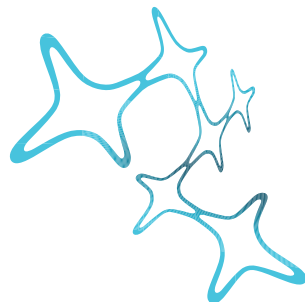

Reverse Engineering the Vestibular System: Intrinsic and Synaptic Contribution to Signal Processing in Frog Central Vestibular Neurons

Christian Andreas Rössert



Graduate School of
Systemic Neurosciences

LMU Munich

München 2010

Reverse Engineering the Vestibular System: Intrinsic and Synaptic Contribution to Signal Processing in Frog Central Vestibular Neurons

Christian Andreas Rössert

Dissertation
an der Graduate School of Systemic Neurosciences
der Ludwig-Maximilians-Universität
München

vorgelegt von
Christian Andreas Rössert
aus München

München, den 15.09.2010

Erstgutachter: PD Dr.-Ing. Stefan Glasauer

Zweitgutachter: Prof. Dr. Hans Straka

Tag der mündlichen Prüfung: 25.11.2010

Summary

Central vestibular neurons in the brainstem are responsible for the major computational step that transforms head acceleration-related sensory signals into appropriate extraocular motor commands for retinal image stabilization. These second-order vestibular neurons (2°VN) receive convergent multimodal information from semicircular canal and otolith organs as well as from the visual (optokinetic) system and neck proprioception. In frog, 2°VN can be separated into two subpopulations (tonic and phasic neurons) that show diverse dynamics in their subthreshold, impedance and spike discharge responses suggesting processing of low-dynamic head motion components in tonic 2°VN and of high-dynamic, nonlinear head motion components in phasic 2°VN. Furthermore, phasic but not tonic 2°VN receive an ipsilateral disynaptic feed-forward inhibition that concurs with their highly dynamic membrane properties.

While information about intrinsic and synaptic properties of 2°VN is available as experimental data, the functional implications of these results on vestibular signal processing was still missing. Furthermore, information on the specific roles of different ion channels in shaping the intracellular response dynamics of 2°VN and their respective interaction with emerging network properties was unknown. This doctoral thesis attempts to answer these questions by combining electrophysiological measurements and quantitative computational modeling.

To reveal the different modes of signal processing in the two 2°VN subtypes, in a first study labyrinthine nerve branches to individual vestibular end organs have been stimulated by trains of single electrical pulses imitating the spike activity of frog vestibular nerve afferents during sinusoidal head rotation *in vivo*. With the help of this stimulation paradigm, pronounced differences in subthreshold dynamics and discharge behavior in tonic and phasic 2°VN have been discovered. Additionally, quantitative subthreshold Hodgkin-Huxley type models of 2°VN have been generated on the basis of available physiological data and were supplemented by respective excitatory and inhibitory synaptic inputs. With the help of this modeling approach it was possible to demonstrate that feed-forward inhibition is the main factor in shaping the subthreshold dynamics of phasic 2°VN and the characteristics of the inhibitory interneurons could be determined.

In the following study the combined subthreshold cellular and network model was extended by an integrate-and-fire threshold to simulate spiking activity. Stimulating the model with an activation pattern as recorded in vestibular nerve afferents during constant angular head acceleration showed how intrinsic and synaptic components can shape the firing behavior of phasic 2°VN. This study thus provided a first insight into the coadaptation of intrinsic membrane properties and synaptic inhibition and generated testable hypotheses for empiric experiments.

To obtain a better characterization of the membrane properties of frog 2°VN, in the third study a frequency-domain analysis of 2°VN was conducted. However, in the course of the experiments it became apparent that the errors induced by the sharp, high-resistant electrodes used for the electrophysiological recordings in 2°VN could not be compensated with the standard amplifier electrode compensation mechanisms. On this account, a novel electrode compensation method called Piece-wise Non-linear Electrode Compensation (PNEC) has been developed that is capable of removing most electrode artifacts in frequency-domain measurements.

In the last study, quantitative spiking Hodgkin-Huxley type models of phasic and tonic 2°VN based on frequency-domain data and interspike frequencies have been constructed. To reproduce the differential subthreshold- and spiking response behavior of phasic and tonic 2°VN the two models differed only by a single additional potassium channel that was low-threshold voltage-dependent in phasic and spike-dependent in tonic 2°VN models. As in the previous simulations, the spiking 2°VN models were extended by conductance-based excitatory synapses and a feed-forward inhibition from tonic 2°VN interneurons onto phasic 2°VN. The resulting quantitative models not only helped elucidating the role of the different membrane parameters in shaping the intracellular response dynamics but also revealed the relative contribution of intrinsic membrane and network properties to synaptic signal processing in phasic 2°VN. Extension of the single cell models to a population model allowed making predictions on intrinsic and synaptic contributions during more natural stimulation including asynchronous afferent fiber input and synaptic noise.

In summary, the results of this thesis will help getting a better understanding of the relative contributions of intrinsic and synaptic factors in generating dynamically appropriate motor commands for retinal image stabilization during locomotion. Furthermore this thesis also has important implications for general electrophysiological measurements using sharp, high-resistant electrodes and provides a promising new alternative electrode compensation method.

Contents

Summary	v
1 Introduction	1
1.1 Semicircular canals, otholith organs and afferent nerve fibers	1
1.2 Second-order vestibular neurons	5
1.2.1 Intrinsic membrane properties of second-order vestibular neurons in amniotes	5
1.2.2 Intrinsic membrane properties of second-order vestibular neurons in frogs	9
1.3 Inhibitory control of second-order vestibular neurons	11
1.4 Methodological aspect: Frequency-domain analysis	13
1.5 Aim of this thesis	15
2 Cumulative Thesis	17
2.1 Differential dynamic processing of afferent signals in frog tonic and phasic second-order vestibular neurons	19
2.2 Modeling of intrinsic and synaptic properties to reveal the cellular and network contribution for vestibular signal processing	21
2.3 Frequency-domain analysis of intrinsic neuronal properties using high-resistant electrodes	23
2.4 Cellular and network contributions to vestibular signal processing: impact of ion conductances, synaptic inhibition and noise	25
3 Discussion	27
3.1 Electrophysiology and quantitative modeling	31
3.2 Intrinsic properties of second-order vestibular neurons of the frog	33
3.3 Signal processing in the vestibular system of the frog	34
Bibliography	37
List of Publications	45
Acknowledgements	47
Enclosure	49
Differential dynamic processing of afferent signals in frog tonic and phasic second- order vestibular neurons	51
Modeling of intrinsic and synaptic properties to reveal the cellular and network contribution for vestibular signal processing	67
Frequency-domain analysis of intrinsic neuronal properties using high-resistant electrodes	73
Cellular and network contributions to vestibular signal processing: impact of ion conductances, synaptic inhibition and noise	87

1 Introduction

Vision, hearing, touch, taste and smell are usually the first to be mentioned when somebody is asked to list biological senses. The vestibular sense, which is the sense of motion and orientation in space, is however often forgotten, yet it plays a vital role in our daily life. The neglect of this sense is not surprising since it provides no distinct tangible sensation and it cannot be shut off. We are thus not aware of this sense unless either sensory conflict with other senses, mismatch or uncertainty in interpreting vestibular signals results in motion sickness or illusions. Other, even more severe incidents that illustrate the importance of the vestibular sense are deficits in the vestibular system (e.g., due to vestibular neuritis, lesions or hair cell loss) that result, amongst others, in disorientation, imbalance and vertigo (Green and Angelaki, 2010).

The set of sensors for the vestibular sense, the vestibular organs, are located in the inner ear on both sides of the head with a mirror-symmetrical spatial arrangement. The signals of the vestibular organs, carried by first-order afferent neurons into the brainstem, contribute to important functions such as gaze stabilization, postural control, balance, spatial perception and spatial navigation (Angelaki and Cullen, 2008). To accomplish these tasks, the vestibular system is highly convergent and multimodal: interactions between different vestibular organs occur at the first synapse in second-order (or central) vestibular neurons (2° VN) which receive the vestibular sensory signals through first-order afferent neurons. Additionally 2° VN receive input from other senses like proprioception and the retinal image-motion-sensitive accessory optic system. Many of the 2° VN are also premotor cells that project directly to extraocular motoneurons and thus already encode a motor command (Straka and Dieringer, 2004). This shows that the important computational step of sensory-motor transformation takes place at 2° VN indicating that the latter neurons play a major role in the control of gaze and posture.

In the following, established knowledge on semicircular canals, otolith organs, afferent nerve fibers and second-order vestibular neurons is reviewed, an introduction into frequency-domain analysis is given and the aim of this doctoral thesis is presented.

1.1 Semicircular canals, otholith organs and afferent nerve fibers

The vestibular organs, also known as the balance organs of the inner ear, consist of three approximately orthogonal oriented semicircular canals, the posterior- (PC), superior- (SC)

(also called anterior- (AC)), and horizontal canal (HC), that detect angular (rotational) accelerations in all three dimensions. Additionally two otolith organs (the utricle and the saccule) in most mammalian species perceive linear accelerations (Cullen and Sadeghi, 2008) (Fig. 1.1). Angular and linear acceleration of the head and head position with respect to gravity are detected via the deflection of hair cells caused by the inertia of either endolymph fluids in semicircular canals or CaCO_3 crystals (the otoconia) in otolith organs (Fig. 1.1).

Whereas the function of the semicircular canals is identical in all vertebrates, most vertebrates (except placental mammals) possess a third otolith organ, the lagena, which along with the sacculus has a dual task in the coding of head movements and detection of substrate vibrations (Ashcroft and Hallpike, 1934; Straka and Dieringer, 2004).

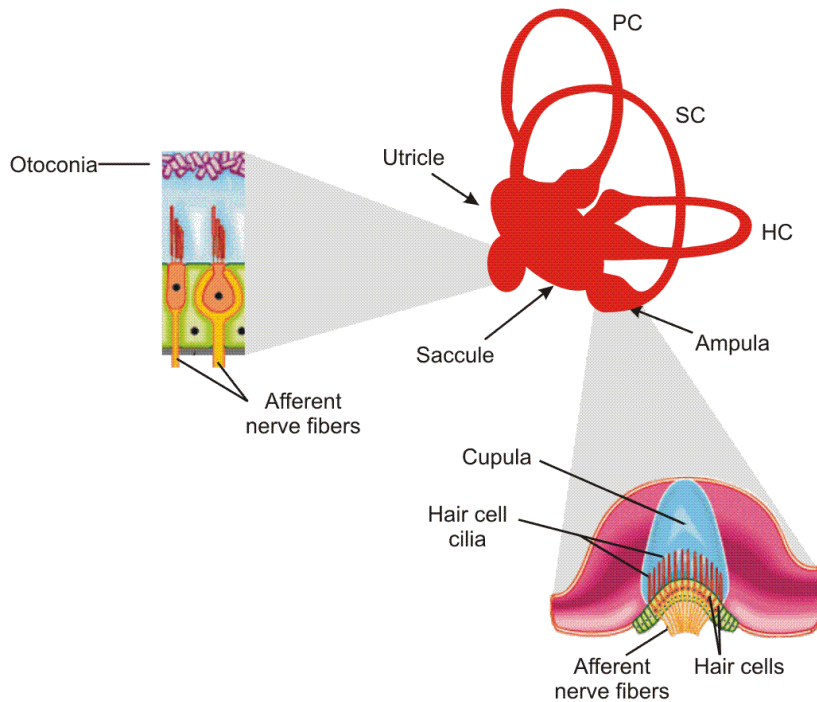


Figure 1.1: Vestibular labyrinth and receptors. Red drawing shows the three semicircular canals that sense rotational movements and the utricle and saccule that are sensitive to linear acceleration. PC, SC, and HC are the posterior, superior, and horizontal canals, respectively. The insets show the semicircular canal hair cells covered by the cupula and the otolith receptors with otoconia. From Cullen and Sadeghi (2008)

Hair cells separate into two main subtypes that have different morphological and physiological properties. Cylindrical shaped Type II hair cells, which are phylogenetically older, are present in both amniotes (i.e., mammals, reptiles, and birds) and anamniotes.

Flask-shaped type I hair cells, which are more sensitive to high frequency stimulation, are however only present in amniotes (Cullen and Sadeghi, 2008). Nevertheless, type II hair cells themselves show diverse morphological and physiological properties which render them sensitive to low- or high-frequency signals (Straka et al., 2009). This frequency selectivity of hair cells allows decomposition of body motion in space into different frequency components.

Hair cells are contacted by ganglion cells whose axons form the afferent fiber bundle (Fig. 1.1) that is part of the eighth cranial nerve and enters the brainstem. Rather than distinct subclasses, afferent fibers form a continuum with respect to several features and show a broad range of axon diameters. Thinner afferent fibers show a regular resting activity (normalized coefficient of variation $CV^* < 0.1$) and tonic discharge to step accelerations, whereas thicker afferent fibers have a highly irregular resting activity ($CV^* > 0.1$) and a phasic discharge in response to step accelerations. These features are thought to render the fibers particularly sensitive to low- and high-frequency signals, respectively (Honrubia et al., 1989; Goldberg, 2000).

Additionally, irregular afferents show higher sensitivities to natural sensory inputs and to externally applied galvanic currents. One possibility, the larger fiber diameter of irregular afferents which should result in greater sensitivity to externally applied currents (BeMent and Ranck, 1969a, 1969b) was shown to only have a small effect (Goldberg et al., 1984). The main effect can be attributed to differences in the action potential after-hyperpolarization (AHP). The different behavior of regular and irregular afferents can be explained with the help of a stochastic AHP model of repetitive discharge (Smith and Goldberg, 1986) fitted to interspike interval statistics. With this modeling approach it was shown that irregular neurons have a faster but weaker AHP current than regular neurons (Fig. 1.2). The differences in the AHPs are thought to be mediated by differential expression of calcium-activated potassium currents I_{KCa} (Goldberg, 2000). The previous two theories are further supported by the finding that smaller (and thus thinner) cultured vestibular-afferent neurons have a 4-times higher density of I_{KCa} channels than larger cells (Limon et al., 2005).

While many of the differences between regular and irregular afferent fibers can be explained by intrinsic membrane properties and thus by the differences in discharge regularity, the frequency response dynamics during sinusoidal head rotations does not depend on the membrane properties. Semicircular canal afferents show at high-frequencies a ~ 10 - fold gain increase and a phase lead which is most prominent in irregular afferents (Goldberg et al., 1982, 1984). However using galvanic stimulation or modeling only a moderate

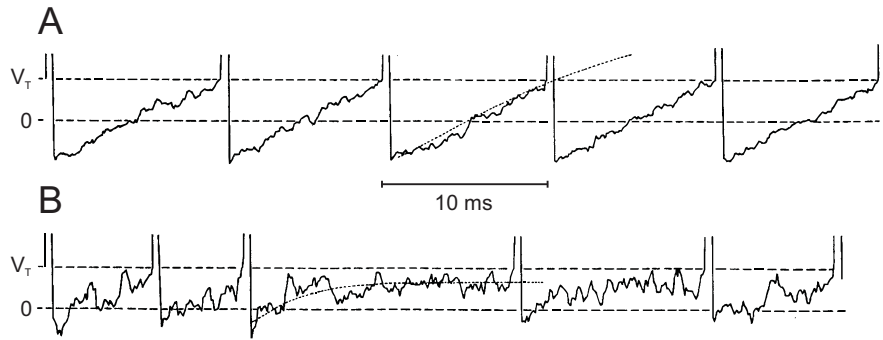


Figure 1.2: Stochastic version of an afterhyperpolarization (AHP) model of repetitive discharge. **A**, Model of afferent fiber with regular discharge because of its deep and slow AHP. **B**, Model of afferent fiber with irregular discharge because of its shallow and fast AHP. Mean interspike trajectories shown as dotted lines, 0 resting potential, V_T spike-threshold potential. From Smith and Goldberg (1986).

~ 1.5 - fold gain increase in both types can be accounted by the membrane properties (Goldberg et al., 1982; Ezure et al., 1983). Differences in frequency response dynamics thus seem to occur at an earlier stage of hair-cell transduction and thus are only correlated but not causally related to discharge regularity. Since irregular fibers transmit information that can not entirely be explained by their intrinsic properties, irregular fibers presumably contact hair cells with an increased gain at higher frequencies. Afferent fibers thus contact hair cells having matched frequency selectivity, which is undermined further by morphological and histochemical observations (Straka et al., 2009) and by the findings that high frequency sensitive type I hair cells mainly provide inputs to irregular vestibular-nerve afferent fibers (Baird et al., 1988). Thus the frequency decomposition as seen in hair cells appears to be retained in vestibular nerve afferent fibers. This frequency-tuned separation in hair cells and afferent fibers is a conserved vertebrate feature (Honrubia et al., 1989; Goldberg, 2000).

In most species, afferent fibers are spontaneously active with a high discharge rate, for example 50-100 Hz in monkeys (Goldberg and Fernandez, 1971; Cullen and Minor, 2002) and mice (Jones et al., 2008). In frogs however, vestibular afferents have a considerably lower discharge of only 1-10 Hz (Blanks and Precht, 1976).

Vestibular nerve afferent fibers innervate central vestibular neurons in the brainstem. At this level the separation of different frequency components is not fully preserved since evoked monosynaptic vestibular afferent excitatory postsynaptic potentials (EPSPs) from a larger spectrum of regular and irregular afferents can be detected in 2° VN. This suggests a certain mixing of different frequency components in most central vestibular neurons (Goldberg, 2000; Straka et al., 2004). Because of this convergence, the information transmission to 2° VN depends on the gain of individual afferents but becomes independent of their discharge regularity (Goldberg, 2000).

1.2 Second-order vestibular neurons

In all vertebrates, second-order vestibular neurons can be subdivided into more or less distinct functional subgroups based on intrinsic cellular properties and discharge dynamics (Straka et al., 2005). In the following, the properties of amniote 2°VN (mainly from recordings in rodents) are presented and compared with the neuronal properties of frog 2°VN.

1.2.1 Intrinsic membrane properties of second-order vestibular neurons in amniotes

In amniotes, most recordings of 2°VN are available from central vestibular neurons in the medial vestibular nucleus (MVN) in rodents (guinea pig, rat and mice) (for a review see Peusner et al. (1998) or Straka et al. (2005)). Intracellularly recorded MVN neurons can be subdivided into two major subtypes called type A and type B neurons. Following each action potential, type A neurons exhibit a single deep after-hyperpolarization (AHP) whereas type B neurons show a biphasic AHP consisting of an initial fast component followed by a delayed second slow AHP (Fig. 1.3, A₁, B₁, C). In addition, type B neurons generally exhibit thinner action potentials, a higher spike rate adaptation in response to depolarizing pulses (Fig. 1.3, A_{2,3}, B_{2,3}) and a more irregular spiking behavior than type A neurons.

The main difference between type A and type B MVN neurons is the implication of different potassium channels in the AHP shape. The deep monophasic AHP in type A neurons is mainly produced by an apamin-insensitive but calcium-dependent (BK type) potassium channel, which is activated by a calcium influx during the action potential. In type B neurons, the initial fast AHP component is produced by 4-aminopyridine (4-AP)-sensitive voltage-dependent potassium channels, whereas the second delayed AHP component is dependent on an apamin-sensitive calcium-dependent (SK type) potassium channel (Serafin et al., 1991; Johnston et al., 1994). In a recent transgenic labeling study it was shown that MVN neurons can be also subdivided into GABAergic neurons labeled in the EGFP (enhanced green fluorescent protein)-expressing inhibitory neuron line (GIN) and glycinergic and glutamatergic neurons labeled in the yellow fluorescent protein-16 (YFP-16) line (Bagnall et al., 2007). Consistent with the previous type A/B classifications, GIN and YFP-16 neurons seem to relate to type A and type B neurons, respectively, due to their corresponding spike shape characteristics. Furthermore, type A/GIN neurons express relatively more calcium-dependent potassium channels (I_{KCa}) and

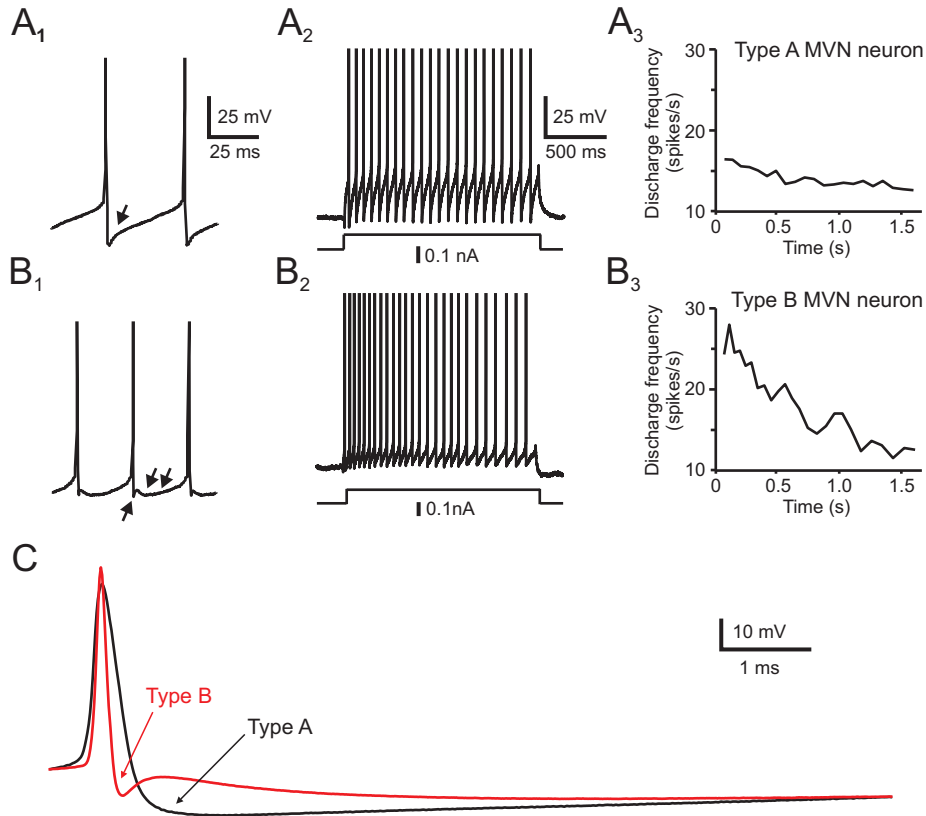


Figure 1.3: Response behavior of type A MVN and type B MVN neurons. **A₁**, **B₁**, During spontaneous spiking, type A MVN neurons exhibit a monophasic after-hyperpolarization (AHP; arrow in **A₁**) whereas type B MVN neurons show a biphasic AHP that consists of an early fast (single arrows in **B₁**) and a delayed, slower component (double arrows in **B₁**). **A_{2,3}**, **B_{2,3}**, In response to depolarizing current pulses type B MVN neurons (**B_{2,3}**) show a stronger spike rate adaptation than type A MVN neurons (**A_{2,3}**). **C**, Overlay of single spikes from a type A (black) and a type B MVN neuron (red) shows the differences in spike width and AHP. Recordings in A and B from guinea pig, modified from Straka et al. (2005). Recordings in C from rat, modified from Johnston et al. (1994).

A-type voltage-dependent potassium channels (I_A) than type B/YFP-16 neurons (Gittis and du Lac, 2007). However both neuronal subtypes express in the same relative amount BK type and SK type I_{KCa} currents. In contrast type B/YFP-16 neurons express relatively more tetraethylammonium (TEA) sensitive voltage-dependent potassium currents (I_{Kv}) mainly composed of the fast and high-voltage activated Kv3 channels (Gittis and du Lac, 2007; Gittis et al., 2010). The large amount of Kv3 channels in type B/YFP-16 neurons is thus responsible for a rather narrow action potential and also accounts for the initial small AHP. Due to the fast Kv3 channel kinetics the initial AHP disappears quickly and the late AHP, generated by slower SK type I_{KCa} currents, progresses. The broad action potential in A/GIN neurons, resulting from a reduced amount of Kv3 channels, consecutively leads to increased calcium influx and thus to a greater activation of BK type I_{KCa} currents. This is consistent with the observation that the BK contribution during narrow action potentials is minimal (Gittis et al., 2010) and the AHP depth is

correlated to spike width (Gittis and du Lac, 2007). The activation of BK currents thus strongly hyperpolarizes the membrane masking the late AHP resulting from activation of slow SK type I_{KCa} currents. The difference between A/GIN and B/YFP-16 neuron spike shape thus seems to be mainly related to the differential expression of voltage-gated Kv3 potassium channels.

A widely accepted conclusion is that type A and B neurons preferentially mediate lower-frequency and higher-frequency signals, respectively (Ris et al., 2001; Straka et al., 2005). This is further supported by the findings that type B/YFP-16 can sustain higher firing rates than type A/GIN neurons (Bagnall et al., 2007) and thus have a wider dynamic range. It was shown that this difference is a direct effect of the higher Kv3 potassium channel expression in type B/YFP-16 neurons (Gittis et al., 2010). Both, type A and B central vestibular neurons in the MVN are spontaneously active in vitro with a rather regular firing rate of approximately 20 Hz (Straka et al., 2005). However, such a regular resting discharge is absent in the intact brain where background firing is very irregular and abolished by sectioning the ipsilateral vestibular nerve (Smith and Curthoys, 1989; Newlands and Perachio, 1990). Most likely type A and B MVN neurons, classified during recordings in brain slices correspond to the classical description in the cat of "tonic" and "kinetic" vestibular neurons of Shimazu and Precht (1965).

To better understand the contribution of the different ion channels to spike shape and frequency response sensitivity of MVN neurons, two models have been constructed on the basis of qualitative spiking behavior. The first model (Quadroni and Knöpfel, 1994), referred to as "Quadroni model", features a complex multi-compartmental dendrite and uses identical processes for the calcium currents, accumulation/removal behavior and a calcium-dependent potassium channel. The different AHP shapes are solely modeled by including different fast voltage-activated potassium currents in type A and type B neurons. The main difference of these currents can be found in the voltage activation kinetics, which have a higher threshold (half activation voltage $V_h = \sim -18 mV$) and a faster activation in type B than in type A neurons (half activation voltage $V_h = \sim -36 mV$). Consistent with recent experimental findings, the Quadroni model thus demonstrates that differences in the I_{Kv} currents can lead to differential spike and AHP shapes in type B and type A neurons. However the deep single AHP in type A model neurons is generated only by I_{Kv} currents whereas all previous experiments suggest a strong involvement of BK type I_{KCa} currents in addition (Johnston et al., 1994; Gittis and du Lac, 2007; Gittis et al., 2010). In contrast, in the second and newer model (Av-Ron and Vidal, 1999), referred to as "Av-Ron model", the AHP shapes are mainly produced by different kinetics of the I_{KCa}

channels and the calcium accumulation/removal process. The resulting I_{KCa} current is slower in type B model cells and thus after an early fast AHP, caused by the standard delayed rectifier potassium current, a second AHP is activated by a calcium-dependent potassium channel (I_{KCa}). In contrast, the resulting I_{KCa} current in type A models is fast and the I_{KCa} channel contributes to and increases the first AHP. With the help of this modeling study the contribution of different intrinsic membrane properties to low-pass, regular spiking and band-pass, irregular spiking behavior in type A and B neurons, respectively, could be demonstrated. However these results are not entirely consistent with electrophysiological recordings. Even though the band-pass firing behavior is higher in type B neurons (Ris et al., 2001), type A neurons do not show purely low-pass characteristics as indicated by the Av-Ron model but also exhibit a gain increase with increasing stimulus frequencies (Beranek et al., 2003; Straka et al., 2005).

Both modeling studies thus necessitate adjustments to recent findings mainly by incorporation of BK and SK type I_{KCa} currents to similar amounts in both type A and B MVN models and of voltage-gated potassium channels in different densities and/or kinetics.

Type A and B MVN neurons also differ in the strength of spike rate adaptation being more prominent in type B neurons (Fig. 1.3, $A_{2,3}$, $B_{2,3}$) (Johnston et al., 1994), which is consistent with YFP-16 and GIN neurons (Bagnall et al., 2007). While calcium-dependent potassium currents are widely known to create spike rate adaptation (Ermentrout, 1998), the effective adaptation time constant (τ_{eff}) (Benda and Herz, 2003) as produced by the type B Av-Ron model ($\tau_{eff} = \sim 50ms$) is one order of magnitude smaller than that seen in MVN neuronal recordings ($\tau_{eff} = \sim 1s$) (Sekirnjak and du Lac, 2002; Straka et al., 2005). This suggests that the late spike rate adaptation in MVN neurons is produced by channels other than the I_{KCa} currents. Smith et al. (2002) support this idea by demonstrating that adaptation in rat MVN neurons is based on spike-dependent but calcium-independent slow potassium currents while confirming that the late AHP is calcium-dependent. Additionally, in Sekirnjak and du Lac (2002) the adaptation behavior was reproduced using a mechanism with a time constant of 1.5 s which, when taking into account that the effective adaptation time constant is always lower, concurs with a τ_{eff} of $\sim 1s$ in the rodent studies. Since spike rate adaptation is directly related to band-pass behavior (Benda and Herz, 2003) this slow non-calcium dependent adaptation process further supports a particular selectivity of type B MVN neurons for higher-frequency signals.

The firing behavior of central vestibular neurons changes with maturation. At the time of birth, most 2°VN in mammals and embryonic principal cells in the tangential vestibular nucleus of chicken show a phasic firing behavior (Peusner et al., 1998; Straka et al., 2005)

which switches to a more tonic firing pattern in adult animals. During depolarizing current injections, these cells either remain silent or generate one or a few spikes immediately after stimulus onset. At least in chicken it has been shown that this accommodation behavior is caused by a low-threshold sustained potassium current (I_{DS}). This channel can be selectively blocked by dendrotoxin (DTX), transforming these neurons into non-accommodating neurons, suggesting an involvement of Kv1.1 and Kv1.2 channel proteins from the Shaker family (Gamkrelidze et al., 1998, 2000). This is further confirmed by a decrease in immunolabeling of Kv1.1 and Kv1.2 in older animals, suggesting a down-regulation in expression of these potassium channel proteins (Popratiloff et al., 2003). In addition, at birth the proportion of type A neurons in mammals is higher while in adult animals more type B MVN neurons can be recorded (Straka et al., 2005). This suggests a shift of proportion from type A cells to type B cells with aging.

1.2.2 Intrinsic membrane properties of second-order vestibular neurons in frogs

Similar to amniotes, second-order vestibular neurons (2° VN) in frog separate into two functional subgroups. Identified 2° VN recorded in the in vitro whole brain preparation can be distinguished into phasic (80%) and tonic neurons (20%) that show distinct intrinsic response dynamics during somatic current injection (Straka et al., 2004). In response to long positive current steps, tonic 2° VN exhibit a permanent discharge (Fig. 1.4, A₁) with a continuous frequency-current (f-I) curve, which corresponds to class 1 excitability (Hodgkin, 1948). In contrast, phasic 2° VN display only one or a few spikes immediately at the beginning of the stimulus current (Fig. 1.4, A₂), corresponding to class 3 excitability. Additionally, tonic neurons show spike rate adaptation in response to depolarizing pulses and a biphasic AHP with a weak second component.

The neuronal filter properties of 2° VN were studied by Beraneck et al. (2007) using intracellular injections of sinusoidal currents with quadratically increasing frequency (ZAP stimuli). This revealed that subthreshold responses as well as spike discharge of tonic 2° VN exhibit low-pass filter-like properties (Fig. 1.4, B₁). In contrast, phasic 2° VN show band-pass filter-like characteristics with a resonance in the subthreshold response at $\sim 10 - 50$ Hz (Fig. 1.4, B₂). With increasing stimulus intensities spikes are triggered around the subthreshold resonance peak. Furthermore the subthreshold responses evoked by ZAP stimuli exhibit an asymmetry in the depolarizing and hyperpolarizing half waves of the sinusoidally modulated membrane potential responses. In tonic 2° VN the depolarizing half waves are larger than the hyperpolarizing half waves, whereas in phasic 2° VN the responses are dominated by the larger hyperpolarizing half waves (compare red subthreshold responses of Fig. 1.4 B₁ and B₂). In phasic 2° VN this effect is attributed

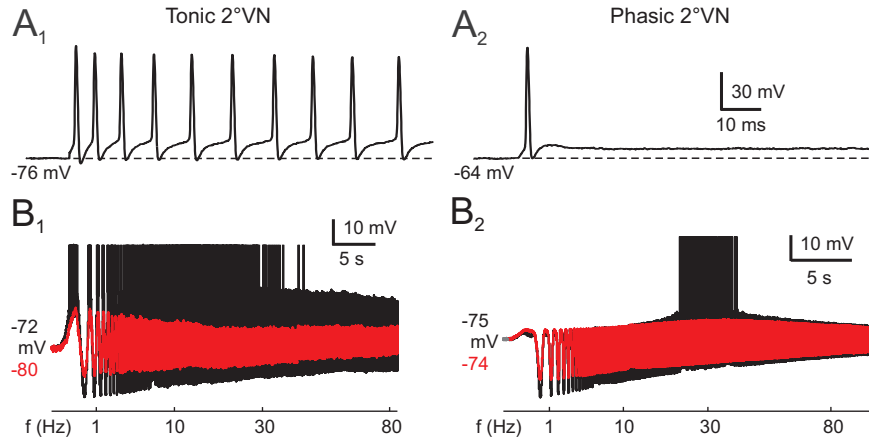


Figure 1.4: Response dynamics of tonic and phasic second-order vestibular neurons. **A**, Continuous discharge (A₁) in tonic and single spike (A₂) in phasic 2°VN evoked by positive current steps. **B**, Subthreshold (red traces) and spiking responses (black traces, spikes truncated) of tonic (B₁) and phasic 2°VN (B₂) evoked by injection of sinusoidally modulated current (ZAP stimuli) with different amplitudes. All subfigures from different neurons. Calibration in A₂ also applies to A₁. Modified from Rössert et al. (in prep.).

to the activation of a low-threshold, voltage-dependent I_D -type Kv1.1 potassium channel. Compatible with this behavior, phasic 2°VN show a decreasing impedance magnitude and increasing resonance with membrane depolarization while tonic 2°VN show an increasing impedance magnitude with membrane depolarization.

In summary, membrane and discharge properties of 2°VN are very similar for guinea pig, mouse, rat and chicken, but are different for frog (Straka et al., 2005). The main difference is the absence of a continuous discharge in the largest neuronal subgroup, the phasic neurons. A comparable phasic behavior can only be found in amniote 2°VN at early developmental stages, as described above. The findings even suggest that in embryonic chicken tangential vestibular neurons and frog phasic 2°VN the same voltage-dependent potassium Kv1.1 channels are responsible for the membrane properties and firing behavior. The only similarity that occurs between mammalian and frog 2°VN is that type B MVN neurons are very similar to tonic 2°VN in the frog due to their similar I-V curves and the biphasic AHP (Straka et al., 2005). However these neurons seem to play different functional roles in frog and mammals, respectively. As described above, type B MVN neurons show a more phasic non-linear response behavior, whereas the complementary type A MVN neurons have more tonic response dynamics. In contrast, tonic 2°VN in frog complement the highly nonlinear phasic 2°VN.

While the properties of 2°VN in frog are different to 2°VN in other species, both subgroups show a surprising similarity to the subgroups of mammalian second-order auditory neurons in the ventral cochlear nucleus (VCN). Like 2°VN also VCN neurons receive in-

put from the eighth cranial nerve from first-order spiral ganglion cells and are like 2°VN sites for convergence of sensory inputs and signal integration. While this is common in all vertebrates, the main similarity is that the two main firing patterns observed during depolarization in VCN neurons are also tonic and phasic. The two subpopulations found in the VCN are tonic stellate cells (also called chopper neurons or type I neurons), showing repetitive firing of action potentials on depolarization and phasic bushy cells (also called type II neurons), generating only one or a few action potentials (Peusner et al., 1998). From current clamp and modeling studies (Rothman and Manis, 2003a, 2003b, 2003c) it has been concluded that both VCN neuron types possess a high-threshold delayed rectifier potassium channel (I_{HT}) (activation threshold $V_{th} > -40$ mV) that is primarily responsible for the repolarization after an action potential. In contrast, the distinct phasic behavior of bushy cells is caused by a low-threshold voltage-activated potassium current (called I_D , I_{DS} or I_{LT}). This channel is sensitive to low concentrations (< 1 mM) of 4-AP and dendrotoxin (DTX), has an activation threshold of $V_{th} < -60$ mV, compatible with an expression of Kv1.1 and Kv1.2 channel subunits in these neurons (Peusner et al., 1998). All these properties show strong similarities to phasic 2°VN suggesting that the differential functional principles of stellate cells and bushy cells also apply to tonic and phasic 2°VN. Besides these similarities a difference is however that 2°VN do not show any sign of a hyperpolarization-activated cation current (I_h) commonly found in VCN neurons (Rothman and Manis, 2003c), which is compatible with the absence of rebound firing in frog 2°VN.

1.3 Inhibitory control of second-order vestibular neurons

Most second-order vestibular neurons do not only receive monosynaptic EPSPs from afferent nerves but also inhibitory inputs through feed-forward and feed-back circuits. One inhibitory input originates from the GABAergic Purkinje cells of the cerebellar cortex, which contributes to adaptation and learning in the vestibulo-ocular reflex (Gittis and du Lac, 2006). Another inhibitory input onto 2°VN is the disynaptic commissural inhibition that, amongst other functions, contributes to the push-pull organization of the angular vestibulo-ocular reflex (Shimazu and Precht, 1966; Kasahara et al., 1968; Mano et al., 1968; Holstein et al., 1999) and causes an increase in sensitivity of the target neurons (Straka and Dieringer, 2004; Malinvaud et al., 2010). A less well-studied input is the ipsilateral disynaptic inhibition that is relayed by local circuits as shown in monkey and frog (Goldberg et al., 1987; Straka and Dieringer, 1996, 2000; Straka et al., 1997).

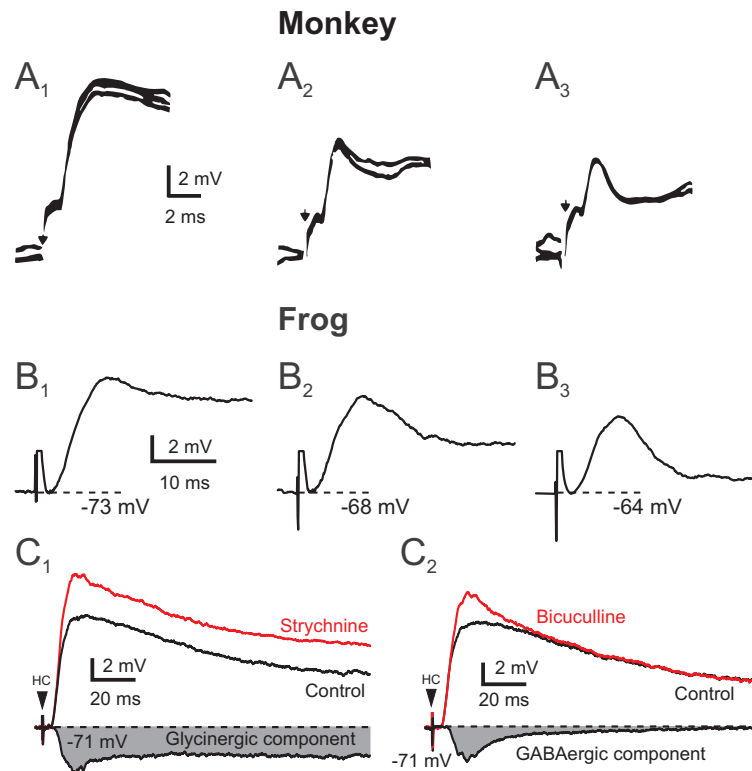


Figure 1.5: Inhibitory responses superimposed on semicircular canal nerve-evoked monosynaptic EPSPs. **A**, Intracellular records from a secondary vestibular neuron following electric shock stimulation of the ipsilateral labyrinths during rest (A_1) and under depolarizing currents of 5 nA (A_2) and 6 nA (A_3) in a squirrel monkey. Due to the depolarization the driving force of the inhibition increases which leads to a reduction of the EPSP. Modified from Goldberg et al. (1987). **B**, Monosynaptic EPSPs evoked by electrical stimulation of the PC nerve recorded at 3 membrane potentials in a phasic 2° VN in frog. Depolarization leads to a decrease of the EPSP decay time due to increased driving force of the inhibition. **C**, Disynaptic glycinergic inhibitory postsynaptic potential (IPSP) superimposed on monosynaptic EPSP evoked by electrical stimulation of the horizontal semicircular canal (HC) nerve in frog. Application of Strychnine or Bicuculline and subtraction from control unmasked the glycinergic (C_1) and GABAergic (C_2) IPSP components, respectively. Modified from Biesdorf et al. (2008).

The superposition of inhibitory responses on semicircular canal nerve-evoked monosynaptic EPSPs has been shown in monkey (Fig. 1.5, A) and frog (Fig. 1.5, B) by a constant intracellular depolarization which increases the driving force of the inhibition. Furthermore, in frog, the inhibition could be separated pharmacologically into a glycinergic and a GABAergic component (Fig. 1.5, C_{1,2}). In frog, the disynaptic inhibition originates from ipsilateral interneurons in the vestibular nuclei (Straka and Dieringer, 1996) thus forming an uncrossed inhibitory feed-forward side-loop.

The function of this inhibition is not entirely understood. An initial model suggested that this inhibition silences the input from irregularly firing afferents to explain the absence of VOR performance loss during ablation of irregular afferents by anodal galvanic stimulation (Minor and Goldberg, 1991). A further physio-pharmacological analysis in frog (Biesdorf et al., 2008) showed that phasic but not tonic 2° VN receive nerve-evoked disynaptic inhi-

bition. Phasic 2°VN are thus embedded into local inhibitory circuits that further reinforce their highly dynamic membrane properties. This embedding of phasic 2°VN in a specific local inhibitory circuit suggests further that intrinsic membrane properties and emerging network properties are coadapted in these neurons to allow differentiation of vestibular afferent inputs.

1.4 Methodological aspect: Frequency-domain analysis

Frequency-domain analysis is an important methodological approach of this doctoral study. In the following, the key concepts will be introduced.

In frequency-domain analysis, systems are analyzed with respect to frequency, rather than time. Whereas time-domain data describes how a signal changes over time, the frequency-domain data describes the amount of different frequency components (sine waves) in the signal. Additionally, frequency-domain representations often also include information on the phase shift which describes how much each sine wave has to be translated in time in order to reconstruct the original time signal. Thus, the two important properties that characterize the transfer function of a system in the frequency-domain are the magnitude- and phase spectrum. One simple way to determine these properties is by using sinusoidal functions of different frequencies as an input, while recording the output. This procedure is exemplarily shown (Fig. 1.6, A) for an electrical circuit of a leaky integrator (Fig. 1.6, A, box). Stimulating the circuit with a sinusoidal current of 20 Hz (Fig. 1.6, A, black line) results in a voltage response (Fig. 1.6, A, red line). The magnitude is defined as the relative amplitude change ($Magnitude = Output\ Amplitude (A_U) / Input\ Amplitude (A_I)$) whereas the phase is defined as the time difference Δt between output and input normalized by the period T and expressed in degree ($Phase = \Delta t / T \cdot 360^\circ$). For 20 Hz this leads to a magnitude of $6.2\ M\Omega$ and a phase of -51.5° . After performing these experiments for all frequencies of interest the resulting magnitude- and phase spectrum are preferentially visualized using Bode plots (Fig. 1.6, B).

Another way to express magnitude and phase is by combining them in a complex quantity $Z(f) = Magnitude \cdot e^{j \cdot Phase \cdot (\pi/180^\circ)}$. In electrical systems this quantity is also called complex impedance, which extends the concept of resistance to dynamic input and has the unit Ω . The inverse of the impedance ($Y(f) = 1/Z(f)$) is called complex admittance with the unit *Siemens*. Impedance and admittance are commonly visualized by plotting

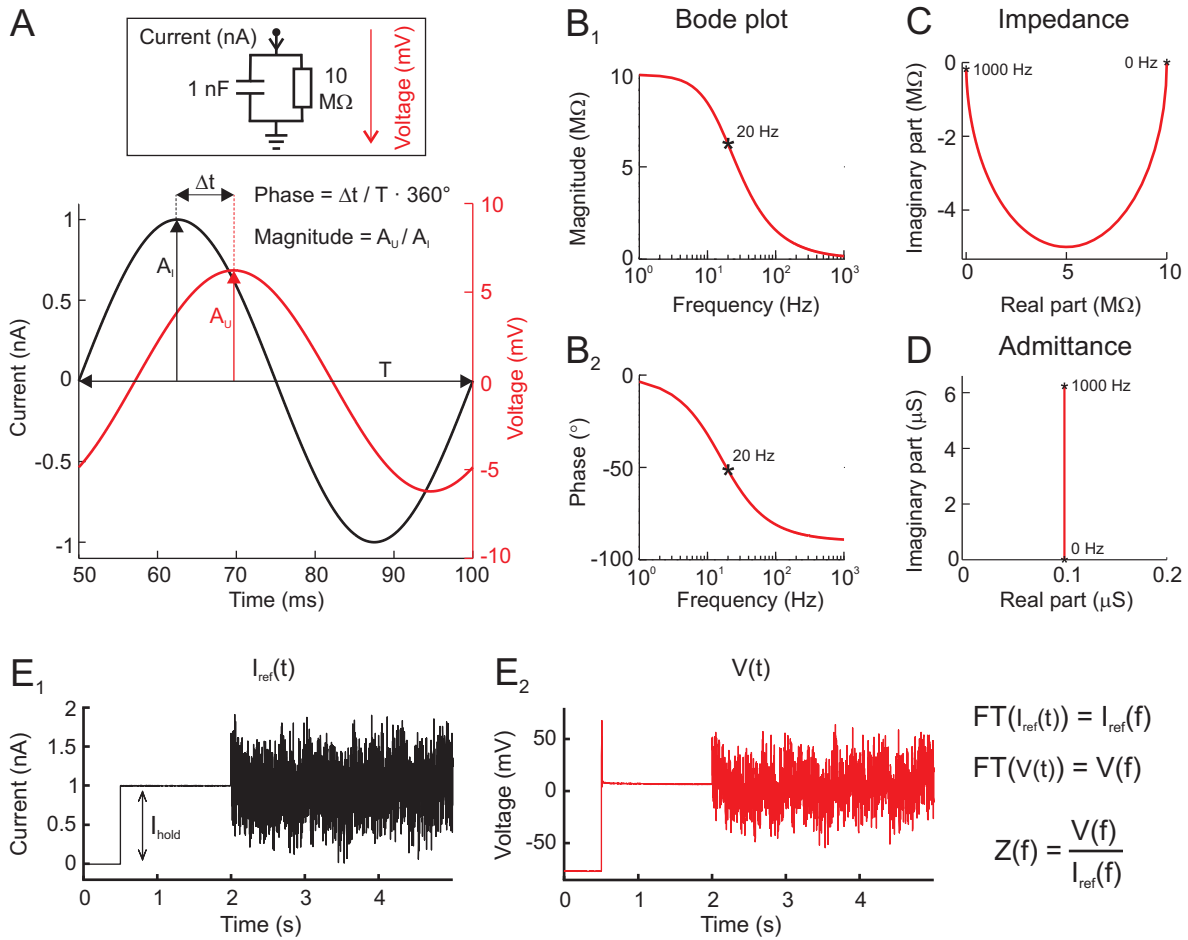


Figure 1.6: Introduction to frequency-domain analysis. **A**, Injection of sinusoidal current of 20 Hz (black line) into a leaky integrator circuit (box) results in a voltage response (red line). **B,C,D**, Transfer function of leaky integrator circuit displayed as a Bode plot (**B_{1,2}**), impedance plot (**C**) or admittance plot (**D**). **E**, Multi-sine current stimulus with discrete frequencies superimposed on a constant holding current, I_{hold} (**E₁**), injected into the neuron leads to a voltage response (without electrode compensation) (**E₂**). Modified from Rössert et al. (2009b).

the real part on the x-axis, whereas the imaginary part is plotted on the y-axis (Fig. 1.6, C, D). In these plots, the frequency is thus expressed as a parameter along the curve, starting with 0 Hz at the point (x,0).

While it is possible to determine magnitude and phase of a system by stimulating with single sinusoids, each frequency one by one, a more effective method for neuronal recordings is to stimulate with all frequencies of interest simultaneously using a multi-sine stimulus I_{MS} . This I_{MS} stimulus is composed of several discrete frequencies with uniform stimulus amplitude and randomized phase spectra. In order to measure the transfer function of neurons at different membrane potentials, the multi-sine stimulus I_{MS} is superimposed on a constant holding current I_{hold} . Stimulating a neuron with $I_{ref}(t) = I_{MS} + I_{hold}$ (Fig. 1.6, **E₁**) leads to an output voltage response $V(t)$ (Fig. 1.6, **E₂**). To calculate the transfer

function, the input and output signal first have to be transformed into the frequency-domain. This is accomplished by the Fourier transform which decomposes a function into its sine wave frequency components leading to the frequency-domain representation of the signal. With the resulting transformed functions $I_{ref}(f)$ and $V(f)$ the transfer function, e.g. the complex impedance, can be easily computed by $Z(f) = V(f)/I_{ref}(f)$. From this the magnitude- and phase spectrum can be calculated using $Magnitude = abs(Z(f))$ and $Phase = arctan(imaginary(Z(f))/real(Z(f))) \cdot 180^\circ/\pi$.

Frequency-domain analysis is not restricted to systems having current input and voltage output but can be deployed using various signal combinations, e.g. current input - firing rate output. The most common form of frequency-domain analysis in this thesis is however current injection and voltage measurement in electrodes and neurons.

Since neurons receive a wide range of rhythmic signals under natural conditions, it is straightforward to investigate their responses to frequencies of biological interest. The simplest neuronal frequency response resembles a low-pass filter, i.e. the impedance magnitude is largest for constant stimuli (0 Hz) (Fig. 1.6, B₁). Such a response can be reproduced by the shown circuit of a leaky integrator which is equal to a passive neuron. However, many cells show a maximal impedance magnitude at non-zero frequencies due to the contribution of sub-threshold ion channels and thus respond best to inputs within a frequency window (band-pass filter). Apart from being useful for analyzing the frequency preference of these latter neurons, frequency-domain analysis also provides a tool for the investigation of intrinsic neuronal properties. The responses of excitable cells to current injection are in general non-linear and difficult to analyze. However conducting a frequency-domain analysis using injection of small amplitude multi-sine currents leads to a piece-wise linearization at different levels of membrane potential. The resulting data can be used to analyze the different contributions of ion channels (Moore et al., 1995; Saint-Mleux and Moore, 2000a, 2000b; Idoux et al., 2008).

1.5 Aim of this thesis

During recent years computational modeling has become a well-established approach for better understanding of intrinsic neuronal signal processing. While for mammalian 2°VN existing neuronal models helped analyzing the intrinsic mechanisms of these cells, this approach has not been yet realized for frog 2°VN. Also, anatomical data about synaptic circuits and their functional implications on the signal processing in mammalian vestibular neurons are scarce. In contrast, specific information about feed-forward inhibitory circuits in the frog vestibular system, the properties of the involved interneurons, the in-

fluence of the inhibition on synaptic signal processing and information about the relative contributions of intrinsic and network properties to the discharge behavior of tonic and phasic 2°VN is available as experimental data, however, a synthesis on the functional implication of these results on a computational level is still missing. This doctoral thesis thus attempts to answer these questions by means of a modeling approach that employs subthreshold and spiking Hodgkin-Huxley type models of 2°VN. The cellular models have been generated on the basis of available physiological data and were supplemented by respective excitatory and inhibitory synaptic inputs. During the frequency-domain analysis of 2°VN, recording errors induced by the glass electrodes have been encountered. Thus a substantial part of this work also focuses on the classification of electrode errors, correction by compensation mechanisms and appropriate selection of the data for quantitative fitting. The resulting models not only will help elucidating the role of the different membrane parameters in shaping the intracellular response dynamics during intracellular and synaptic activation of single neurons but also will allow making further predictions on signal processing characteristics at the population level.

2 Cumulative Thesis

This cumulative thesis consists of three publications and one manuscript currently in preparation for submission. In the following, the abstracts of these publications are presented and the contribution of the author to the respective publications is indicated. The full papers are enclosed in the appendix of this thesis. The full list of publications, including those which are not included in this thesis, is indicated separately (see Contents).

2.1 Differential dynamic processing of afferent signals in frog tonic and phasic second-order vestibular neurons

Pfanzelt S, Rössert C, Rohregger M, Glasauer S, Moore LE, Straka H (2008) Differential dynamic processing of afferent signals in frog tonic and phasic second-order vestibular neurons. *J. Neurosci.* 28:10349-10362

The sensory-motor transformation of the large dynamic spectrum of head-motion-related signals occurs in separate vestibulo-ocular pathways. Synaptic responses of tonic and phasic second-order vestibular neurons were recorded in isolated frog brains after stimulation of individual labyrinthine nerve branches with trains of single electrical pulses. The timing of the single pulses was adapted from spike discharge patterns of frog semicircular canal nerve afferents during sinusoidal head rotation. Because each electrical pulse evoked a single spike in afferent fibers, the resulting sequences with sinusoidally modulated intervals and peak frequencies up to 100 Hz allowed studying the processing of presynaptic afferent inputs with in vivo characteristics in second-order vestibular neurons recorded in vitro in an isolated whole brain. Variation of pulse-train parameters showed that the postsynaptic compound response dynamics differ in the two types of frog vestibular neurons. In tonic neurons, subthreshold compound responses and evoked discharge patterns exhibited relatively linear dynamics and were generally aligned with pulse frequency modulation. In contrast, compound responses of phasic neurons were asymmetric with large leads of subthreshold response peaks and evoked spike discharge relative to stimulus waveform. These nonlinearities were caused by the particular intrinsic properties of phasic vestibular neurons and were facilitated by GABAergic and glycinergic inhibitory inputs from tonic type vestibular interneurons and by cerebellar circuits. Coadapted intrinsic filter and emerging network properties thus form dynamically different neuronal elements that provide the appropriate cellular basis for a parallel processing of linear, tonic, and nonlinear phasic vestibulo-ocular response components in central vestibular neurons.

The author of this doctoral thesis contributed to Pfanzelt et al. (2008) by assisting in the data analysis, by creating and fitting the computational models and by writing the modeling part of the paper.

2.2 Modeling of intrinsic and synaptic properties to reveal the cellular and network contribution for vestibular signal processing

Rössert C, Pfanzelt S, Straka H, Glasauer S (2009a) Modeling of intrinsic and synaptic properties to reveal the cellular and network contribution for vestibular signal processing. *Ann. N. Y. Acad. Sci* 1164:451-454

Computational modeling of cellular and network properties of central vestibular neurons is necessary for understanding the mechanisms of sensory-motor transformation for gaze stabilization. As a first step to mathematically describe vestibular signal processing, the available physiological data of the synaptic and intrinsic properties of frog second-order vestibular neurons (2°VN) were used to create a model that combines cellular and network parameters. With this approach it is now possible to reveal the particular contributions of intrinsic membrane versus emerging network properties in shaping labyrinthine afferent-evoked synaptic responses in 2°VN , to simulate perturbations, and to generate hypotheses that are testable in empiric experiments.

The author of this doctoral thesis contributed to Rössert et al. (2009a) by creating the computational models and by writing major parts of the manuscript.

2.3 Frequency-domain analysis of intrinsic neuronal properties using high-resistant electrodes

Rössert C, Straka H, Glasauer S, Moore LE (2009b) Frequency-domain analysis of intrinsic neuronal properties using high-resistant electrodes. *Front. Neurosci.* 3:64. doi:10.3389/neuro.17.002.2009

Intrinsic cellular properties of neurons in culture or slices are usually studied by the whole cell clamp method using low-resistant patch pipettes. These electrodes allow detailed analyses with standard electrophysiological methods such as current- or voltage-clamp. However, in these preparations large parts of the network and dendritic structures may be removed, thus preventing an adequate study of synaptic signal processing. Therefore, intact *in vivo* preparations or isolated *in vitro* whole brains have been used in which intracellular recordings are usually made with sharp, high-resistant electrodes to optimize the impalement of neurons. The general non-linear resistance properties of these electrodes, however, severely limit accurate quantitative studies of membrane dynamics especially needed for precise modelling. Therefore, we have developed a frequency-domain analysis of membrane properties that uses a Piece-wise Non-linear Electrode Compensation (PNEC) method. The technique was tested in second-order vestibular neurons and abducens motoneurons of isolated frog whole brain preparations using sharp potassium chloride- or potassium acetate-filled electrodes. All recordings were performed without online electrode compensation. The properties of each electrode were determined separately after the neuronal recordings and were used in the frequency-domain analysis of the combined measurement of electrode and cell. This allowed detailed analysis of membrane properties in the frequency-domain with high-resistant electrodes and provided quantitative data that can be further used to model channel kinetics. Thus, sharp electrodes can be used for the characterization of intrinsic properties and synaptic inputs of neurons in intact brains.

The author of this doctoral thesis contributed to Rössert et al. (2009b) by performing all cellular recordings including data analysis, by developing the electrode compensation method and by writing major parts of the manuscript.

2.4 Cellular and network contributions to vestibular signal processing: impact of ion conductances, synaptic inhibition and noise

Rössert C, Straka H, Moore LE, Glasauer S (in prep.) Cellular and network contributions to vestibular signal processing: impact of ion conductances, synaptic inhibition and noise.

Head motion-related sensory signals are transformed by second-order vestibular neurons (2°VN) into appropriate extraocular motor commands for retinal image stabilization during body motion. In frog, these 2°VN form two distinct subpopulations that have either linear (tonic 2°VN) or highly non-linear intrinsic properties (phasic 2°VN), compatible with low-pass and band-pass filter characteristics, respectively. In the present study, available physiological data on cellular properties of 2°VN have been used to construct conductance-based spiking cellular models that were fine-tuned by fitting to spike-frequency data. The obtained results of this approach suggest that the differential response characteristics of the two vestibular subtypes are mainly caused by a single additional potassium channel that is low-threshold and voltage-dependent in phasic and spike-dependent in tonic 2°VN . The insertion of phasic 2°VN into a local feed-forward inhibitory network was used to develop a cellular model with conductance-based synapses that allows simulation of the emerging properties of this network. This approach reveals the relative contributions of intrinsic and synaptic factors on afferent signal processing in phasic 2°VN . Extension of the single cell model to a population model allowed further testing under more natural conditions including asynchronous afferent labyrinthine input and synaptic noise. This latter approach indicated that the feed-forward inhibition from the local inhibitory network acts as a high-pass filter, which reinforces the impact of the intrinsic membrane properties of phasic 2°VN on peak response timing. Moreover, the model suggests that synaptic noise and postsynaptic properties of the target neurons critically influence the dynamics of vestibulo-motor commands.

The author of this doctoral thesis contributed to Rössert et al. (in prep.) by creating and fitting all computational models and by writing major parts of the manuscript.

3 Discussion

While information about intrinsic and synaptic properties of tonic and phasic second-order vestibular neurons (2°VN) is available, up to now, nothing was known about the contribution of these intrinsic and synaptic factors to the overall signal processing. Especially information on the influence of the inhibition on synaptic signal processing and on the properties of the involved interneurons was missing. To this end, in Pfanzelt et al. (2008) individual labyrinthine nerve afferents were stimulated by trains of single electrical pulses, mimicking the spike activity of frog vestibular nerve afferents during sinusoidal head rotation *in vivo*. This stimulation paradigm revealed pronounced differences in subthreshold dynamics and discharge behavior. In tonic 2°VN , the compound responses, consisting of temporal summation of the individual monosynaptic EPSPs evoked by each single pulse, show an overall waveform that is approximately aligned with the stimulus frequency modulation and spikes are triggered as soon as spike threshold is reached.

In phasic 2°VN however the compound responses show an early decay that creates an asymmetry with a response peak skewed to the left of the stimulus frequency peak and spikes are triggered only by the first few pulses of the stimulus train. In addition, available physiological data on intrinsic and synaptic properties of 2°VN were used to create a model that combines subthreshold conductance-based cellular models with network parameters. The results of this modeling approach showed that the feed-forward inhibition is mainly responsible for the highly asymmetric compound response in phasic 2°VN , consistent with pharmacological results. Furthermore the model indicates also that the typical leftward skew in phasic EPSP compound responses can only be reproduced with an inhibition originating from a neuron with a persistent discharge, thus suggesting that the inhibitory interneurons are tonic-type 2°VN . The stimulation paradigm in Pfanzelt et al. (2008) is convenient to identify the basis of a differential processing of vestibular signals in 2°VN , however having the drawback that all afferent fibers respond in synchrony to the given stimulation pattern. Under natural head rotations however, afferent fibers show a broad spectrum of response dynamics that results in an asynchronous synaptic input onto 2°VN (Goldberg, 2000).

In the following modeling study (Rössert et al., 2009a) the combined subthreshold cellular and network model from Pfanzelt et al. (2008) was extended by an integrate-and-fire threshold to simulate spiking activity. In this study, the model was stimulated using

an activation pattern as recorded in vestibular nerve afferents during constant angular head acceleration. During this type of activation the tonic 2°VN model exhibited a spike discharge that is amplified but otherwise similar to that of the afferent input whereas the phasic 2°VN model only responds at the stimulus onset at high stimulus frequencies. Further simulations with reduced inhibition or reduced I_D channels indicated that intrinsic and synaptic components contribute both to the distinct firing behavior of the phasic 2°VN model, yet in different ways. This modeling study thus provides an insight into the coadaptation of intrinsic membrane properties and inhibition and generates testable hypotheses for empiric experiments.

To better characterize the membrane properties of frog 2°VN and to obtain impedance data for the quantitative fitting of Hodgkin Huxley type models, a frequency-domain analysis of 2°VN was conducted (Moore et al., 1995; Saint-Mleux and Moore, 2000a, 2000b; Idoux et al., 2008). However, during this analysis it became apparent that the sharp, high-resistant electrodes used for the electrophysiological recordings in 2°VN show a highly non-linear behavior during current injection. Using a multi-sine analysis it was demonstrated that these electrodes show a conductance that increases with stimulation frequency and exhibit inductive properties which lead to an impedance magnitude resonance at low frequencies (Rössert et al., 2009b). Additionally this behavior was not constant for a given electrode but strongly depended on the depth of the electrode tip in the solution and on the strength of the constant holding currents. The usual electrode compensation circuits implemented in most intracellular amplifiers usually treat the electrode as a simple linear RC circuit which however, especially during frequency-domain measurements, proved to be inefficient in compensating the highly non-linear electrode behavior. Therefore a Piece-wise Non-linear Electrode Compensation (PNEC) method for frequency-domain analysis of membrane properties was developed (Rössert et al., 2009b). In PNEC the electrode properties are determined separately for each injected holding current after the neuronal recordings which are then used in the frequency-domain analysis of the combined measurement of electrode and cell to subtract the electrode components. The technique was tested with model cell recordings, neuronal recordings and simulations and demonstrated to be applicable to compensate for most of the highly non-linear electrode effects in frequency-domain recordings. Furthermore it was shown that the PNEC framework can be used for electrode kernel estimation and offline subtraction of the electrode voltage drop also in the time-domain. This mechanism could also be deployed in voltage-clamp measurements as long the electrode is measured before entering a cell.

The goal of the study by Rössert et al. (in prep.) was to create spiking Hodgkin-Huxley type models for phasic and tonic 2°VN based on quantitative measurements to make further predictions on possible effects of intrinsic and synaptic factors on vestibular signal processing. To accomplish this task, reliable data for quantitative neuron fitting had to be found. Rössert et al. (2009b) showed that during current injection the voltage response is superimposed by electrode artifacts unless PNEC is used. For phasic 2°VN enough frequency-domain data, measured with multi-sine current injections and PNEC, was available to create subthreshold multi-compartment conductance-based models. Using previously reported kinetics of the low-threshold Kv1.1 I_D potassium channel (Rothman and Manis, 2003c) the subthreshold impedance magnitude behavior recorded in phasic 2°VN could be adequately reproduced. However, in the subthreshold recordings no information on the spiking mechanism is present. Yet a substantial amount of data measured with standard bridge RC compensation existed with the only reliable information from these recordings being the firing behavior under constant depolarization and the membrane potential decay after current injections. Therefore spiking tonic and phasic 2°VN multi-compartment models, which differed by a single additional potassium channel that is low-threshold voltage-dependent (I_D channel) in phasic and spike-dependent in tonic 2°VN models, have been fitted to interspike frequencies and to the membrane potential decays after injections of small currents.

The resulting models proved to be faithful representations of phasic and tonic 2°VN since they are capable of reproducing all typical subthreshold, impedance magnitude and firing characteristics. In addition, the analysis of the interspike rate amplitude of tonic 2°VN during ZAP current injections indicated that the latter neuronal type exhibits band-pass filter characteristics with a resonance peak at low frequencies compatible with their low-pass membrane potential behavior. With the help of the modeling approach this effect could be attributed to the spike-dependent potassium current.

As in Pfanzelt et al. (2008), the spiking 2°VN models have been extended by conductance-based excitatory synapses and a feed-forward inhibition from tonic 2°VN interneurons onto phasic 2°VN (Fig. 3.1, B₁). During mimicked sinusoidally modulated excitation of vestibular nerve afferents, tonic 2°VN models exhibit a typical linear and symmetric subthreshold EPSP compound and spiking response as observed in electrophysiological recordings (Fig. 3.1, A_{2,3}).

In phasic 2°VN models however, the prominent early decay of the subthreshold EPSP compound response is only reproduced if a feed-forward inhibition is activated (Fig. 3.1,

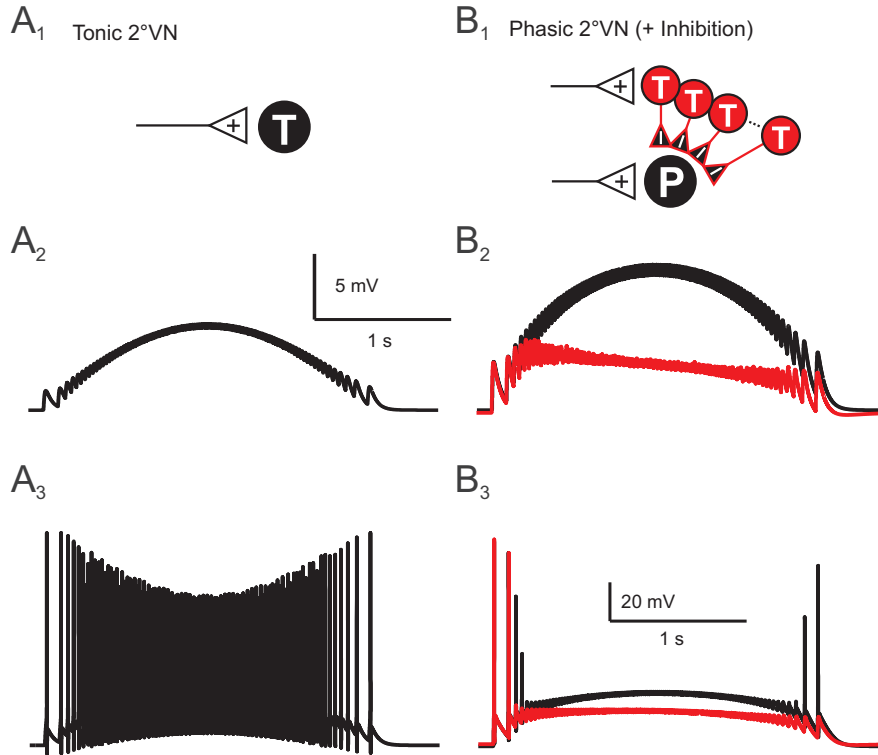


Figure 3.1: Model responses following sinusoidally modulated pulse-train stimulation (peak frequency 70 Hz). Responses shown during subthreshold synaptic excitation (A_2 , B_2) and during synaptic excitation with spiking (A_3 , B_3). Three different cellular and network configurations: A, tonic model with excitation only, B, phasic model with excitation only (black) and phasic model with excitation and inhibition from tonic 2° VN models (red). Network configuration depicted in A_1 and B_1 , respectively. Modified from Rössert et al. (in prep.).

B_2 compare black (without inhibition) with red trace (with inhibition)) confirming the observation that inhibition is the major contributor to the pronounced response peak asymmetry in phasic 2° VN (Pfanzelt et al., 2008). During spike responses, the I_D channel alone was sufficient to resist continuous spike discharge in some phasic 2° VN models. In general however, the inhibition from local tonic inhibitory interneurons is necessary to generate the phasic spiking behavior typically observed in intracellular measurements (Fig. 3.1, B_3).

As mentioned before, one drawback of a pulse stimulation is that all afferent fibers respond more or less in synchrony to the given stimulation pattern. To analyze the effect of uncorrelated responses from single afferent fibers during natural head rotations, two populations of phasic and tonic 2° VN models, created on parameters statistics, have been stimulated by injection of noisy sinusoidal currents. Instead of using a classical spike rate analysis, the postsynaptic conductance (G_S) at a theoretical target neuron produced by each population was computed. The postsynaptic conductances were simulated using alpha functions with either short or long synaptic time constants, thus allowing exami-

nation of the effect of integration and summation at the postsynapse. The simulations revealed that the local inhibitory network acts as a high-pass filter which reinforces the intrinsic membrane properties of phasic 2°VN and controls the peak resonance frequency (Fig. 3.2, B).

Furthermore it could be shown that the frequency response behavior critically depends on the postsynaptic time constant. In the absence of inhibition, long time constants in combination with noisy signals lead to an increased gain in the low-frequency range where most neurons of the phasic 2°VN population are normally silent (Fig. 3.2, B red solid line). In the tonic 2°VN population a resonance as observed in single neuron measurements is only visible with a short postsynaptic time constant. Long postsynaptic time constants however cause the resonance to disappear due to integration over a longer time period (Fig. 3.2, A).

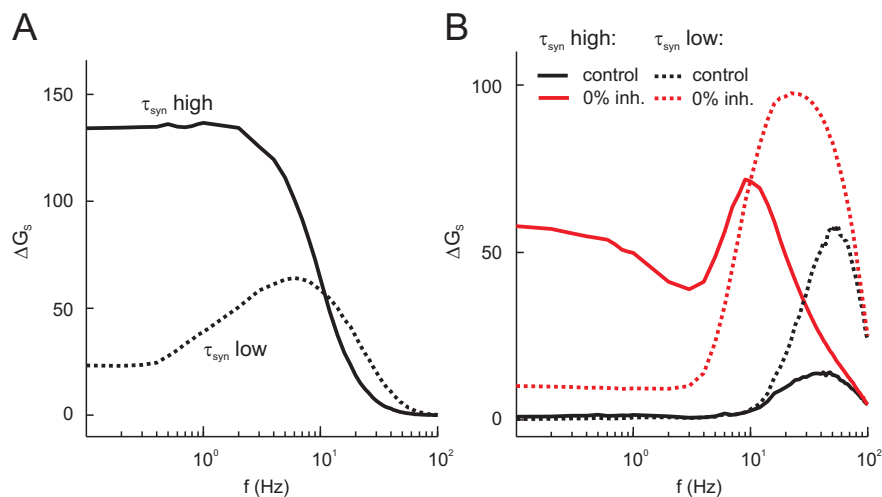


Figure 3.2: Effect of synaptic integration and feed-forward inhibition on the population model response. Abstract post-synaptic conductance amplitude ΔG_S of tonic (A) and phasic 2°VN population (B) with low- (dotted lines) and high post synaptic time constant (solid lines). Also phasic population response without inhibition (B, red lines) is shown. Modified from Rössert et al. (in prep.).

With the results of this thesis, important implications on electrophysiology and quantitative modeling, on intrinsic properties of second-order vestibular neurons and on signal processing in the vestibular system can be made. In the following, these three topics are further discussed in detail.

3.1 Electrophysiology and quantitative modeling

While standard electrode compensation techniques are effectively used with low-resistant patch pipettes, other recent publications showed that these standard methods are not suf-

ficient to compensate the effects of low-pass filtering (Li et al., 2004), artifactual voltage transients and nonlinearities (Brette et al., 2008) caused by sharp, high-resistant electrodes. Thus, as a first step before conducting an electrophysiological study, the possible sources for recording errors should always be judged critically. In particular, the properties of the recording electrodes should be measured independently, preferably with a frequency-domain analysis. With this type of analysis the response behavior also to high frequency currents can be evaluated. A linear electrode response over a broad frequency range is especially important when dynamic currents are injected via the electrode e.g. during voltage clamp or dynamic clamp experiments.

If the sufficiency of standard RC electrode compensation can not be guaranteed, there are only two possible solutions: either information that is free of electrode artifacts must be used, e.g. spiking or membrane potential without simultaneous current injections, or advanced electrode compensation methods should be employed. In this study it was shown that with PNEC neuronal transfer functions of phasic and tonic 2° VN using high-resistant sharp electrodes can be estimated which can be further used to analyze membrane properties and the different contributions of ion channels (Hutcheon and Yarom, 2000). Another alternative electrode compensation technique is the Active Electrode Compensation (AEC) method described by Brette et al. (2008). The difference between PNEC and AEC is however that the latter was specifically designed to compensate for electrode responses in the time-domain and the electrode properties are estimated from a combined electrode and neuron measurement. The AEC method thus does not require a separate electrode measurement as it is the case for PNEC. However the quality of AEC is strongly dependent on electrode- and membrane-time constant ratios and it was shown that the AEC electrode kernel estimation procedure is inaccurate especially when the electrode has an inductive/resonating behavior, which is no problem for the PNEC procedure. Advanced electrode compensation is a challenging task, especially for experiments in *in vivo* or *in vitro* whole brain preparations where very low resistance electrodes cannot be employed. Here, the PNEC method provides a promising new approach to significantly increase the quality of these recordings.

In the past years, besides the classical voltage clamp measurements (Hodgkin and Huxley, 1952; Rothman and Manis, 2003a, 2003b) many different approaches to quantitative neuron modeling have been realized (see Jolivet et al., 2008). A large part of these studies tried to fit neuronal models to membrane potential and spike shapes (Weaver and Wearne, 2006; Geit et al., 2008) but also fits to spike rates (Pospischil et al., 2008) have been performed. In this study a different approach, the fitting to frequency-domain impedance measurements was employed (Moore et al., 1995; Saint-Mleux and Moore, 2000a, 2000b; Idoux et al., 2008). However, the current-clamp multi-sine measurements

on which the fitting is based are restricted to the subthreshold membrane potential and thus the effects of intrinsic mechanisms that are activated at high-voltage potentials can not be measured. In tonic 2°VN, the restriction of subthreshold current-clamp multi-sine measurements becomes particularly apparent. Here the subthreshold impedance response shows no sign of the important adaptation current which only could be characterized using interspike frequencies. One possibility to overcome this subthreshold membrane potential restriction is by deploying voltage-clamp multi-sine measurements which however requires a good control over the membrane potential.

3.2 Intrinsic properties of second-order vestibular neurons of the frog

While for mammalian central vestibular neurons two neuronal models for the two subpopulations exist, the present one is the first model for frog phasic and tonic 2°VN. These cellular models give new insights into the intrinsic computational mechanisms, especially in tonic 2°VN. In the previous study that used ZAP stimuli in 2°VN (Beraneck et al., 2007) the discharge properties have been analyzed using only a spike probability analysis, which resulted in a pure low-pass spiking characteristic of tonic 2°VN. However applying a spike rate analysis to tonic 2°VN ZAP responses revealed a band-pass behavior with a resonance at low frequencies ($\sim 5 Hz$) which was reproduced by the model. With the help of modeling it could be shown that the spike-dependent potassium current, included to account for the adapting interspike frequencies, is responsible for this band-pass behavior. Since no effect of this adaptation current was found in the subthreshold membrane and impedance response it is possible that the adaptation is a combination of high-threshold calcium currents and calcium-dependent potassium currents (Ermentrout, 1998; Benda and Herz, 2003). This duality of low-pass subthreshold and resonant spike responses has also been reported previously in chick MVN neurons, which most likely is also caused by a spike dependent adaptation mechanism. The findings of calcium-dependent potassium currents in these neurons (du Lac, 1996) further support this conclusion. As reported earlier, type B mammalian MVN neurons, that are similar to tonic 2°VN, possess an apamin-sensitive calcium-dependent (SK type) potassium channel that causes a similar spike rate adaptation- and resonance behavior (Bagnall et al., 2008). Furthermore the modeling study suggests that the adaptation process causes the linear current - firing rate relationship in tonic 2°VN as also observed in MVN neurons (du Lac and Lisberger, 1995; Bagnall et al., 2008). Furthermore, the shaping of AHPs by calcium-dependent potassium channels seems to be an important functional feature for vestibular signal processing since it is also present in vestibular afferent fibers, as indicated in the introduction.

In contrast to tonic 2°VN, phasic 2°VN show a resonance in their subthreshold membrane potential. This behavior could be reproduced in frequency- as well as time-domain models by including low-threshold potassium currents (I_{LT}) as found in second-order auditory neurons in the ventral cochlear nucleus (VCN) (Rothman and Manis, 2003c). This illustrates a similarity between bushy VCN cells and phasic 2°VN. In addition, the phasic 2°VN models confirmed that the ZAP response peak frequency of phasic 2°VN increases with depolarization (Beraneck et al., 2007) which might serve as a possible mechanism to control the frequency sensitivity of these neurons, e.g. by long-lasting large-amplitude commissural EPSPs (Dieringer and Precht, 1977; Malinvaud et al., 2010).

While the modeling approach in this thesis offers considerable new insight into the intrinsic signal transmission of second-order vestibular neurons, there are still possibilities for improvements that however have to be based on appropriate experiments. The larger depolarizing than hyperpolarizing half-waves and the impedance magnitude increase with depolarization in tonic 2°VN are reproduced with the intracellular model. However this effect is caused by the window current of the standard fast sodium conductance omitting non-inactivating sodium or calcium conductances as suggested in previous publications (Beraneck et al., 2007; Pfanzelt et al., 2008; Rössert et al., 2009b). The possible contribution of these channels should thus be examined by a detailed voltage-clamp study which however is difficult due to the lack of specific pharmacological blockers for non-inactivating sodium currents. Furthermore, to account for the membrane time constant, multi-compartmental neuron models with a simple passive dendrite had to be used which suggests a large influence of the cell morphology on the signal transmission properties. In future studies this should be taken into account by detailed combined morpho-physiological models.

3.3 Signal processing in the vestibular system of the frog

The results of this thesis strongly suggest co-adaptation of intrinsic membrane and emerging network properties resulting in an optimization of phasic 2°VN characteristics for the processing of high-dynamic, nonlinear head motion components. Hence, with the modeling approach the relative contribution of intrinsic and synaptic factors in phasic 2°VN during sinusoidally modulated pulse train activation could be revealed: while intrinsic properties mainly control the sensitivity and discharge duration at the beginning of the stimulation, the inhibition mainly influences the response at the end of the pulse train

thus leading to a prominent event detection capability in phasic 2°VN (Rössert et al., 2009a; Rössert et al., in prep.). Such a coadaptation of intrinsic membrane and network properties has been shown before in the Mautner cell in fish (Nakayama and Oda, 2004) where recurrent inhibition and membrane properties both contribute to phasic spiking behavior.

The results of the population model including noisy stimulation further demonstrates a functional coadaptation of intrinsic membrane and emerging network properties since the inhibition acts as a high-pass filter which concurs with the intrinsic membrane properties of phasic 2°VN and influences the peak resonance frequency. The inhibition also counteracts the effect of the noise in the phasic 2°VN population and thus allows the band-pass behavior to be maintained during asynchronized responses from individual afferent fibers. The results from the population model are also consistent with the ablation model by Minor and Goldberg (1991) since the inhibition is capable in silencing the responses in the frequency range of 0.1-4 Hz as required by the ablation study.

The low-frequency resonance as found in spike rate responses of tonic 2°VN does not contradict the processing of low-dynamic and tonic head motion components in these cells. The resonance frequency is one magnitude lower than in phasic 2°VN and thus renders tonic 2°VN functionally complementary to the highly nonlinear phasic 2°VN. The shift in signal specificity with higher frequencies in frog 2°VN likely reflects a specific adaptation to its locomotor style that is characterized by long periods of immobility and brief, rapid head/body movements (Schneider, 1954; King and Comer, 1996). In addition to the linearization of the frequency-current (f-I) response (Ermentrout, 1998), the adaptation current I_{KA} also leads to an increased cutoff frequency as seen in the population model responses with a large postsynaptic time constant.

Even if many of the actual synaptic properties in the population model are unknown, the results clearly indicate that the output of the system critically depends on the integrational capabilities of the postsynaptic process. With a short postsynaptic time constant the synaptic integration is limited, thereby ensuring a more or less unaltered transformation of pre- into postsynaptic signals which conserves response resonance phenomena. In contrast, a long synaptic time constant causes signal integration over longer time periods, thereby cancelling or diminishing potential presynaptic response resonances observed in both tonic and phasic 2°VN. Although, only the integrational effect of the postsynapse has been demonstrated in the simulations, the integrational membrane properties (Magee, 2000; Segev and London, 2000) of the postsynaptic neurons, e.g. the extraocular motoneu-

rons, itself very likely lead to the same behavior. As the synaptic current integration increases with distance from the soma (Rall et al., 1967)) the amount of 2°VN resonance antagonization at the next synaptic level thus directly depends on the site of the synaptic contact. Intrinsic membrane properties in combination with synaptic and intrinsic integration at extraocular motoneurons thus provides a mechanism to shape adequate motor signals for compensatory eye motion by dynamically changing synaptic weights at somato-dendritic sites.

In future studies the synaptic and cellular properties of the motoneurons should thus be examined thoroughly to better characterize their influence on signal processing. Furthermore the models of the excitatory synapses were simplified as dual-exponential and alpha synapses and could be refined to account for possible further synaptic effects e.g. synaptic plasticity (Johnston and Wu, 1994) by appropriate measurements of the respective neurons. Ipsilateral excitation and feed-forward inhibition are only two sources for inputs onto 2°VN. As indicated in the introduction, 2°VN receive in numerous different ways body-motion-related signals, e.g. commissural excitation and inhibition from the contralateral side, back-propagation from the cerebellum and proprioceptive and optokinetic signals. To obtain knowledge about possible interactions of these inputs the presented models provide a good basis for guiding appropriate experiments. Thus the tight interaction between experimental approaches and computational modeling allows separating the different contributions of individual parameters (ion channels, synapses, time constants) to the transformation of sensory inputs into motor commands for gaze and posture control.

Bibliography

- Angelaki DE, Cullen KE (2008) Vestibular system: the many facets of a multimodal sense. *Annual Review of Neuroscience* 31:125–150.
- Ashcroft DW, Hallpike CS (1934) On the function of the saccule. *The Journal of Laryngology & Otology* 49:450–460.
- Av-Ron E, Vidal PP (1999) Intrinsic membrane properties and dynamics of medial vestibular neurons: a simulation. *Biological Cybernetics* 80:383–392.
- Bagnall MW, McElvain LE, Faulstich M, du Lac S (2008) Frequency-independent synaptic transmission supports a linear vestibular behavior. *Neuron* 60:343–352.
- Bagnall MW, Stevens RJ, du Lac S (2007) Transgenic mouse lines subdivide medial vestibular nucleus neurons into discrete, neurochemically distinct populations. *The Journal of Neuroscience* 27:2318–2330.
- Baird RA, Desmadryl G, Fernández C, Goldberg JM (1988) The vestibular nerve of the chinchilla. II. relation between afferent response properties and peripheral innervation patterns in the semicircular canals. *Journal of Neurophysiology* 60:182–203.
- BeMent SL, Ranck JB (1969a) A model for electrical stimulation of central myelinated fibers with monopolar electrodes. *Experimental Neurology* 24:171–186.
- BeMent SL, Ranck JB (1969b) A quantitative study of electrical stimulation of central myelinated fibers. *Experimental Neurology* 24:147–170.
- Benda J, Herz AVM (2003) A universal model for spike-frequency adaptation. *Neural Computation* 15:2523–2564.
- Beraneck M, Hachemaoui M, Idoux E, Ris L, Uno A, Godaux E, Vidal P, Moore LE, Vibert N (2003) Long-Term plasticity of ipsilesional medial vestibular nucleus neurons after unilateral labyrinthectomy. *Journal of Neurophysiology* 90:184–203.
- Beraneck M, Pfanzelt S, Vassias I, Rohregger M, Vibert N, Vidal P, Moore LE, Straka H (2007) Differential intrinsic response dynamics determine synaptic signal processing in frog vestibular neurons. *The Journal of Neuroscience* 27:4283–4296.

- Biesdorf S, Malinvaud D, Reichenberger I, Pfanzelt S, Straka H (2008) Differential inhibitory control of semicircular canal nerve afferent-evoked inputs in second-order vestibular neurons by glycinergic and GABAergic circuits. *Journal of Neurophysiology* 99:1758–1769.
- Blanks RHI, Precht W (1976) Functional characterization of primary vestibular afferents in the frog. *Experimental Brain Research* 25:369–390.
- Brette R, Piwkowska Z, Monier C, Rudolph-Lilith M, Fournier J, Levy M, Frégnac Y, Bal T, Destexhe A (2008) High-resolution intracellular recordings using a real-time computational model of the electrode. *Neuron* 59:379–391.
- Cullen K, Sadeghi S (2008) Vestibular system. *Scholarpedia* 3:3013.
- Cullen KE, Minor LB (2002) Semicircular canal afferents similarly encode active and passive head-on-body rotations: implications for the role of vestibular efference. *The Journal of Neuroscience* 22:RC226.
- Dieringer N, Precht W (1977) Modification of synaptic input following unilateral labyrinthectomy. *Nature* 269:431–433.
- du Lac S (1996) Candidate cellular mechanisms of vestibulo-ocular reflex plasticity. *Annals of the New York Academy of Sciences* 781:489–498.
- du Lac S, Lisberger S (1995) Cellular processing of temporal information in medial vestibular nucleus neurons. *The Journal of Neuroscience* 15:8000–8010.
- Ermentrout B (1998) Linearization of F-I curves by adaptation. *Neural Computation* 10:1721–1729.
- Ezure K, Cohen MS, Wilson VJ (1983) Response of cat semicircular canal afferents to sinusoidal polarizing currents: implications for input-output properties of second-order neurons. *Journal of Neurophysiology* 49:639–648.
- Gamkrelidze G, Giaume C, Peusner KD (2000) Firing properties and dendrotoxin-insensitive sustained potassium current in vestibular nuclei neurons of the hatchling chick. *Experimental Brain Research* 134:398–401.
- Gamkrelidze G, Giaume C, Peusner KD (1998) The differential expression of Low-Threshold sustained potassium current contributes to the distinct firing patterns in embryonic central vestibular neurons. *The Journal of Neuroscience* 18:1449–1464.

-
- Geit WV, Schutter ED, Achard P (2008) Automated neuron model optimization techniques: a review. *Biological Cybernetics* 99:241–251.
- Gittis AH, du Lac S (2006) Intrinsic and synaptic plasticity in the vestibular system. *Current Opinion in Neurobiology* 16:385–390.
- Gittis AH, du Lac S (2007) Firing properties of GABAergic versus non-GABAergic vestibular nucleus neurons conferred by a differential balance of potassium currents. *Journal of Neurophysiology* 97:3986–3996.
- Gittis AH, Moghadam SH, du Lac S (2010) Mechanisms of sustained high firing rates in two classes of vestibular nucleus neurons: differential contributions of resurgent na, kv3, and BK currents. *Journal of Neurophysiology* .
- Goldberg JM (2000) Afferent diversity and the organization of central vestibular pathways. *Experimental Brain Research* 130:277–297.
- Goldberg JM, Fernandez C (1971) Physiology of peripheral neurons innervating semicircular canals of the squirrel monkey. i. resting discharge and response to constant angular accelerations. *Journal of Neurophysiology* 34:635–660.
- Goldberg JM, Highstein SM, Moschovakis AK, Fernandez C (1987) Inputs from regularly and irregularly discharging vestibular nerve afferents to secondary neurons in the vestibular nuclei of the squirrel monkey. i. an electrophysiological analysis. *Journal of Neurophysiology* 58:700–718.
- Goldberg JM, Smith CE, Fernandez C (1984) Relation between discharge regularity and responses to externally applied galvanic currents in vestibular nerve afferents of the squirrel monkey. *Journal of Neurophysiology* 51:1236–1256.
- Goldberg J, Fernandez C, Smith C (1982) Responses of vestibular-nerve afferents in the squirrel monkey to externally applied galvanic currents. *Brain Research* 252:156–160.
- Green AM, Angelaki DE (2010) Internal models and neural computation in the vestibular system. *Experimental Brain Research* 200:197–222.
- Hodgkin AL (1948) The local electric changes associated with repetitive action in a non-medullated axon. *The Journal of Physiology* 107:165–181.
- Hodgkin AL, Huxley AF (1952) Currents carried by sodium and potassium ions through the membrane of the giant axon of loligo. *The Journal of Physiology* 116:449–472.

- Holstein GR, Martinelli GP, Cohen B (1999) The ultrastructure of GABA-immunoreactive vestibular commissural neurons related to velocity storage in the monkey. *Neuroscience* 93:171–181.
- Honrubia V, Hoffman LF, Sitko S, Schwartz IR (1989) Anatomic and physiological correlates in bullfrog vestibular nerve. *Journal of Neurophysiology* 61:688–701.
- Hutcheon B, Yarom Y (2000) Resonance, oscillation and the intrinsic frequency preferences of neurons. *Trends in Neurosciences* 23:216–222.
- Idoux E, Eugene D, Chambaz A, Magnani C, White JA, Moore LE (2008) Control of neuronal persistent activity by Voltage-Dependent dendritic properties. *Journal of Neurophysiology* 100:1278–1286.
- Johnston AR, MacLeod NK, Dutia MB (1994) Ionic conductances contributing to spike repolarization and after-potentials in rat medial vestibular nucleus neurones. *The Journal of Physiology* 481:61–77.
- Johnston D, Wu SM (1994) *Foundations of Cellular Neurophysiology* The MIT Press.
- Jolivet R, Roth A, Schürmann F, Gerstner W, Senn W (2008) Special issue on quantitative neuron modeling. *Biological Cybernetics* 99:237–239.
- Jones T, Jones S, Hoffman L (2008) Resting discharge patterns of macular primary afferents in Otoconia-Deficient mice. *Journal of the Association for Research in Otolaryngology* 9:490–505.
- Kasahara M, Mano N, Oshima T, Ozawa S, Shimazu H (1968) Contralateral short latency inhibition of central vestibular neurons in the horizontal canal system. *Brain Research* 8:376–378.
- King JR, Comer CM (1996) Visually elicited turning behavior in rana pipiens: comparative organization and neural control of escape and prey capture. *Journal of Comparative Physiology* 178:293–305.
- Li W, Soffe SR, Roberts A (2004) A direct comparison of whole cell patch and sharp electrodes by simultaneous recording from single spinal neurons in frog tadpoles. *Journal of Neurophysiology* 92:380–386.
- Limon A, Perez C, Vega R, Soto E (2005) Ca^{2+} -Activated K^{+} -Current density is correlated with soma size in rat Vestibular-Afferent neurons in culture. *Journal of Neurophysiology* 94:3751–3761.

-
- Magee JC (2000) Dendritic integration of excitatory synaptic input. *Nature Reviews. Neuroscience* 1:181–190.
- Malinvaud D, Vassias I, Reichenberger I, Rössert C, Straka H (2010) Functional organization of vestibular commissural connections in frog. *The Journal of Neuroscience* 30:3310–3325.
- Mano N, Oshima T, Shimazu H (1968) Inhibitory commissural fibers interconnecting the bilateral vestibular nuclei. *Brain Research* 8:378–382.
- Minor LB, Goldberg JM (1991) Vestibular-nerve inputs to the vestibulo-ocular reflex: a functional-ablation study in the squirrel monkey. *The Journal of Neuroscience* 11:1636–1648.
- Moore L, Buchanan J, Murphey C (1995) Localization and interaction of N-methyl-D-aspartate and non-N-methyl-D-aspartate receptors of lamprey spinal neurons. *Biophysical Journal* 68:96–103.
- Nakayama H, Oda Y (2004) Common sensory inputs and differential excitability of segmentally homologous reticulospinal neurons in the hindbrain. *The Journal of Neuroscience* 24:3199–3209.
- Newlands SD, Perachio AA (1990) Compensation of horizontal canal related activity in the medial vestibular nucleus following unilateral labyrinth ablation in the decerebrate gerbil. *Experimental Brain Research* 82:359–372.
- Peusner K, Gamkrelidze G, Giaume C (1998) Potassium currents and excitability in second-order auditory and vestibular neurons. *Journal of Neuroscience Research* 53:511–520.
- Pfanzelt S, Rössert C, Rohregger M, Glasauer S, Moore LE, Straka H (2008) Differential dynamic processing of afferent signals in frog tonic and phasic Second-Order vestibular neurons. *The Journal of Neuroscience* 28:10349–10362.
- Popratiloff A, Giaume C, Peusner KD (2003) Developmental change in expression and subcellular localization of two shaker-related potassium channel proteins (Kv1.1 and kv1.2) in the chick tangential vestibular nucleus. *The Journal of Comparative Neurology* 461:466–482.
- Pospischil M, Toledo-Rodriguez M, Monier C, Piwkowska Z, Bal T, Frégnac Y, Markram H, Destexhe A (2008) Minimal Hodgkin-Huxley type models for different classes of cortical and thalamic neurons. *Biological Cybernetics* 99:427–441.

- Quadroni R, Knöpfel T (1994) Compartmental models of type a and type b guinea pig medial vestibular neurons. *Journal of Neurophysiology* 72:1911–1924.
- Rall W, Burke RE, Smith TG, Nelson PG, Frank K (1967) Dendritic location of synapses and possible mechanisms for the monosynaptic EPSP in motoneurons. *Journal of Neurophysiology* 30:1169–1193.
- Ris L, Hachemaoui M, Vibert N, Godaux E, Vidal PP, Moore LE (2001) Resonance of spike discharge modulation in neurons of the guinea pig medial vestibular nucleus. *Journal of Neurophysiology* 86:703–716.
- Rothman JS, Manis PB (2003a) Differential expression of three distinct potassium currents in the ventral cochlear nucleus. *Journal of Neurophysiology* 89:3070–3082.
- Rothman JS, Manis PB (2003b) Kinetic analyses of three distinct potassium conductances in ventral cochlear nucleus neurons. *Journal of Neurophysiology* 89:3083–3096.
- Rothman JS, Manis PB (2003c) The roles potassium currents play in regulating the electrical activity of ventral cochlear nucleus neurons. *Journal of Neurophysiology* 89:3097–3113.
- Rössert C, Pfanzelt S, Straka H, Glasauer S (2009a) Modeling of intrinsic and synaptic properties to reveal the cellular and network contribution for vestibular signal processing. *Annals of the New York Academy of Sciences* 1164:451–454.
- Rössert C, Straka H, Glasauer S, Moore LE (2009b) Frequency-domain analysis of intrinsic neuronal properties using high-resistant electrodes. *Frontiers in Neuroscience* 3:64. doi:10.3389/neuro.17.002.2009.
- Rössert C, Straka H, Moore LE, Glasauer S (in prep.) Cellular and network contributions to vestibular signal processing: impact of ion conductances, synaptic inhibition and noise. *Manuscript in preparation* .
- Saint-Mleux B, Moore LE (2000a) Active dendritic membrane properties of xenopus larval spinal neurons analyzed with a whole cell soma voltage clamp. *Journal of Neurophysiology* 83:1381–1393.
- Saint-Mleux B, Moore LE (2000b) Firing properties and electrotonic structure of xenopus larval spinal neurons. *Journal of Neurophysiology* 83:1366–1380.
- Schneider D (1954) Das Gesichtsfeld und der Fixiervorgang bei einheimischen Anuren. *Zeitschrift für vergleichende Physiologie* 36:147–164.

-
- Segev I, London M (2000) Untangling dendrites with quantitative models. *Science* 290:744–750.
- Sekirnjak C, du Lac S (2002) Intrinsic firing dynamics of vestibular nucleus neurons. *The Journal of Neuroscience* 22:2083–2095.
- Serafin M, de Waele C, Khateb A, Vidal PP, Mühlethaler M (1991) Medial vestibular nucleus in the guinea-pig. II. ionic basis of the intrinsic membrane properties in brainstem slices. *Experimental Brain Research* 84:426–433.
- Shimazu H, Precht W (1965) Tonic and kinetic responses of cat's vestibular neurons to horizontal angular acceleration. *Journal of Neurophysiology* 28:991–1013.
- Shimazu H, Precht W (1966) Inhibition of central vestibular neurons from the contralateral labyrinth and its mediating pathway. *Journal of Neurophysiology* 29:467–492.
- Smith CE, Goldberg JM (1986) A stochastic afterhyperpolarization model of repetitive activity in vestibular afferents. *Biological Cybernetics* 54:41–51.
- Smith MR, Nelson AB, du Lac S (2002) Regulation of firing response gain by Calcium-Dependent mechanisms in vestibular nucleus neurons. *Journal of Neurophysiology* 87:2031–2042.
- Smith PF, Curthoys IS (1989) Mechanisms of recovery following unilateral labyrinthectomy: a review. *Brain Research Reviews* 14:155–180.
- Straka H, Beraneck M, Rohregger M, Moore LE, Vidal P, Vibert N (2004) Second-order vestibular neurons form separate populations with different membrane and discharge properties. *Journal of Neurophysiology* 92:845–861.
- Straka H, Biesdorf S, Dieringer N (1997) Canal-Specific excitation and inhibition of frog Second-Order vestibular neurons. *Journal of Neurophysiology* 78:1363–1372.
- Straka H, Dieringer N (1996) Uncrossed disynaptic inhibition of second-order vestibular neurons and its interaction with monosynaptic excitation from vestibular nerve afferent fibers in the frog. *Journal of Neurophysiology* 76:3087–3101.
- Straka H, Dieringer N (2000) Convergence pattern of uncrossed excitatory and inhibitory semicircular canal-specific inputs onto second-order vestibular neurons of frogs. *Experimental Brain Research* 135:462–473.
- Straka H, Dieringer N (2004) Basic organization principles of the VOR: lessons from frogs. *Progress in Neurobiology* 73:259–309.

Straka H, Vibert N, Vidal PP, Moore LE, Dutia MB (2005) Intrinsic membrane properties of vertebrate vestibular neurons: function, development and plasticity. *Progress in Neurobiology* 76:349–392.

Straka H, Lambert FM, Pfanzelt S, Beraneck M (2009) Vestibulo-ocular signal transformation in frequency-tuned channels. *Annals of the New York Academy of Sciences* 1164:37–44.

Weaver CM, Wearne SL (2006) The role of action potential shape and parameter constraints in optimization of compartment models. *Neurocomputing* 69:1053–1057.

List of Publications

- Glasauer S, Rössert C (2008) Modelling drug modulation of nystagmus. *Progress in Brain Research* 171:527-534.
- Pfanzelt S, Rössert C, Rohregger M, Glasauer S, Moore LE, Straka H (2008) Differential dynamic processing of afferent signals in frog tonic and phasic second-order vestibular neurons. *The Journal of Neuroscience* 28:10349-10362.
- Rössert C, Pfanzelt S, Straka H, Glasauer S (2009) Modeling of intrinsic and synaptic properties to reveal the cellular and network contribution for vestibular signal processing. *Annals of the New York Academy of Sciences* 1164:451-454.
- Rössert C, Straka H, Glasauer S, Moore LE (2009) Frequency-domain analysis of intrinsic neuronal properties using high-resistant electrodes. *Frontiers in Neuroscience* 3:64. doi:10.3389/neuro.17.002.2009.
- Malinvaud D, Vassias I, Reichenberger I, Rössert C, Straka H (2010) Functional organization of vestibular commissural connections in frog. *The Journal of Neuroscience* 30:3310-3325

Acknowledgements

I would like to express my sincere gratitude to the people that helped me during the time of my thesis.

I am extremely grateful to my supervisor PD Dr.-Ing. Stefan Glasauer for giving me the opportunity to conduct my doctoral study in his group. I have been most fortunate to have a second supervisor, Prof. Dr. Hans Straka. I am very thankful to him for introducing me into the field of electrophysiology and giving me the possibility to do experiments in his lab. I would like to thank both of my supervisors for their constant belief in my abilities and for giving me the freedom to develop my own ideas and concepts. Their enthusiasm for research and their optimism encouraged me during various phases of my study.

I would like to thank Prof. Dr. Christian Leibold for being part of my thesis advisory committee and for giving valuable suggestions during my committee meetings.

Further, I want to thank Dr. Sandra Pfanzelt and Dr. Lee E. Moore for their contribution and help especially at the beginning of my doctoral study. I am also very thankful to all my colleagues in the "Forschungshaus". Although we had very different research areas I enjoyed the good working atmosphere.

Last but not least, I would also thank my parents who always supported me. Without their help and big trust I would never have made it that far.

Enclosure

Differential dynamic processing of afferent signals in frog tonic and phasic second-order vestibular neurons

Differential Dynamic Processing of Afferent Signals in Frog Tonic and Phasic Second-Order Vestibular Neurons

Sandra Pfanzelt,^{1,2} Christian Rössert,² Martin Rohregger,³ Stefan Glasauer,² Lee E. Moore,¹ and Hans Straka¹

¹Laboratoire de Neurobiologie des Réseaux Sensorimoteurs, Centre National de la Recherche Scientifique, UMR 7060, Université Paris Descartes, 75270 Paris Cedex 06, France, ²Department of Neurology, Bernstein Center for Computational Neuroscience, Ludwig-Maximilians-Universität München, 81377 Munich, Germany, and ³Department of Physiology, Ludwig-Maximilians-Universität München, 80336 Munich, Germany

The sensory–motor transformation of the large dynamic spectrum of head-motion-related signals occurs in separate vestibulo-ocular pathways. Synaptic responses of tonic and phasic second-order vestibular neurons were recorded in isolated frog brains after stimulation of individual labyrinthine nerve branches with trains of single electrical pulses. The timing of the single pulses was adapted from spike discharge patterns of frog semicircular canal nerve afferents during sinusoidal head rotation. Because each electrical pulse evoked a single spike in afferent fibers, the resulting sequences with sinusoidally modulated intervals and peak frequencies up to 100 Hz allowed studying the processing of presynaptic afferent inputs with *in vivo* characteristics in second-order vestibular neurons recorded *in vitro* in an isolated whole brain. Variation of pulse-train parameters showed that the postsynaptic compound response dynamics differ in the two types of frog vestibular neurons. In tonic neurons, subthreshold compound responses and evoked discharge patterns exhibited relatively linear dynamics and were generally aligned with pulse frequency modulation. In contrast, compound responses of phasic neurons were asymmetric with large leads of subthreshold response peaks and evoked spike discharge relative to stimulus waveform. These nonlinearities were caused by the particular intrinsic properties of phasic vestibular neurons and were facilitated by GABAergic and glycinergic inhibitory inputs from tonic type vestibular interneurons and by cerebellar circuits. Coadapted intrinsic filter and emerging network properties thus form dynamically different neuronal elements that provide the appropriate cellular basis for a parallel processing of linear, tonic, and nonlinear phasic vestibulo-ocular response components in central vestibular neurons.

Key words: semicircular canal; phasic; tonic; afferent fibers; vestibular; macula

Introduction

Processing of head movement-related signals in vestibulomotor networks occurs in parallel pathways that are organized as frequency-tuned channels from the sensory periphery to the motor plant (Lisberger et al., 1983; Minor et al., 1999; Goldberg, 2000; Straka and Dieringer, 2004). This parallel organization is necessary to transform sensory signals as diverse as static head deviation or high acceleration profiles that occur during rapid locomotion into dynamically adequate motor commands for gaze and posture control. Hair cells in vestibular end organs and vestibular afferent fibers appear to be organized as subpopulations of dynamically different neuronal elements with interrelated morphophysiological properties for the detection and cod-

ing of head motion (Baird, 1994a,b; Eatock et al., 1998; Goldberg, 2000; Straka and Dieringer, 2004).

At the level of central vestibular neurons distinct subpopulations of second-order vestibular neurons (2°VNs) with different intrinsic membrane properties have been observed in various vertebrate species (Serafin et al., 1991; Johnston et al., 1994; du Lac and Lisberger, 1995; Peusner and Giaume, 1997; Straka et al., 2005). Although cellular properties of 2°VNs may vary between vertebrate species, the different neuronal subgroups form specific filter elements, respectively (Straka et al., 2005). If appropriately adapted to the dynamics of the sensory afferent inputs, these central vestibular populations could separately mediate linear (tonic) and nonlinear (phasic) vestibulomotor components (Minor et al., 1999; Clendaniel et al., 2002).

Based on specific differences in intrinsic membrane properties, frog 2°VNs subdivide into two distinct neuronal subtypes (Straka et al., 2004; Beraneck et al., 2007). Tonic 2°VNs behave like low-pass filters, whereas phasic 2°VNs show a pronounced resonance behavior for subthreshold membrane polarization and spike discharge, thereby generating potential-dependent band-pass filters (Beraneck et al., 2007). The different impedance behavior during membrane polarization makes the two subtypes most suitable for amplification (tonic 2°VNs) and differentiation (phasic 2°VNs) of vestibular inputs (Beraneck et al., 2007). A different insertion of the two neuronal subtypes into local inhib-

Received July 8, 2008; revised Aug. 22, 2008; accepted Aug. 28, 2008.

This work was supported by the French Centre National de la Recherche Scientifique and Centre National d'Etudes Spatiales. S.P. received funding from a Marie-Curie Training Sites contract HPMT-CT-2000-00008 (France), the Deutscher Akademischer Austauschdienst D/05/40377 (Germany), and the Graduiertenkolleg 1091 (Orientation and Motion in Space); C.R. received a PhD grant from the Bayerische Forschungstiftung. We thank Dr. Mathieu Beraneck for critically reading this manuscript and Dr. Isabelle Vassias for excellent processing and photographing of the histological material shown in Figure 2A.

Correspondence should be addressed to Dr. Hans Straka, Laboratoire de Neurobiologie des Réseaux Sensorimoteurs, Centre National de la Recherche Scientifique, UMR 7060, Université Paris Descartes, 45 rue des Saints-Pères, 75270 Paris Cedex 06, France. E-mail: hans.straka@univ-paris5.fr.

DOI:10.1523/JNEUROSCI.3368-08.2008

Copyright © 2008 Society for Neuroscience 0270-6474/08/2810349-14\$15.00/0

itory networks as indicated by the presence of ipsilateral disynaptic feedforward IPSPs in phasic but not tonic 2° VNs (Biesdorf et al., 2008) concurs with the highly transient intrinsic properties of the former neurons. The distinctly different filter properties and their differential effect on single monosynaptic afferent EPSPs in phasic and tonic 2° VNs suggests that more complex synaptic inputs similar to those that occur during natural head movements would be the appropriate test to reveal the different modes of signal processing of the two subtypes.

The present study uses the isolated brain of adult frogs to investigate the synaptic responses of tonic and phasic 2° VNs after activation of labyrinthine nerve afferents by trains of single electrical pulses with a timing that was obtained from the spike discharge of afferent fibers during head movements. For this purpose, the spike activity of frog vestibular nerve afferents during sinusoidal head rotation *in vivo* (Blanks and Precht, 1976) was transformed into a sequence of single electrical pulses for the activation of individual labyrinthine nerve branches *in vitro*.

Preliminary results have been published previously in abstract form (Pfanzelt et al., 2004).

Materials and Methods

In vitro experiments were performed on the isolated brains of 47 grass frogs (*Rana temporaria*) and complied with the *Principles of Animal Care* (publication No. 86-23, revised in 1985 by the National Institutes of Health). Permission for these experiments was granted by the government of Oberbayern (211-2531-31/95). As described in previous studies (Straka and Dieringer, 1993), the animals were deeply anesthetized with 0.1% MS-222 (3-aminobenzoic acid ethyl ester), and perfused transcardially with iced Ringer's solution [(in mM) 75 NaCl, 25 NaHCO₃, 2 CaCl₂, 2 KCl, 0.5 MgCl₂, 11 glucose, pH 7.4]. Thereafter, the skull and bony labyrinth were opened by a ventral approach. After dissecting the three semicircular canals on each side, the brain was removed with all labyrinthine end organs attached to the eighth nerve. Subsequently, the brain was submerged in iced Ringer's and the dura, the labyrinthine end organs, and the choroid plexus covering the fourth ventricle were removed. In all experiments, the forebrain was removed. Brains were used up to 4 d after their isolation and were stored overnight at 6°C in continuously oxygenated Ringer's solution (carbogen, 95% O₂, 5% CO₂) with a pH of 7.5 ± 0.1. For the experiments, the brainstem was glued with cyanoacrylate to a plastic mesh, which was fixed with insect pins to the Sylgard floor of a chamber (volume, 2.4 ml). The chamber was continuously perfused with oxygenated Ringer's solution at a rate of 1.3–2.1 ml/min. The temperature was electronically controlled and maintained at 14 ± 0.1°C.

Intracellular recordings were obtained from vestibular nerve afferent fibers ($n = 27$) and central vestibular neurons ($n = 110$). Vestibular nerve afferents were recorded in the eighth nerve between Scarpa's ganglion and the entry of the nerve into the brainstem. The peripheral origin of individual afferent fibers was determined by the presence of short-latency all-or-nothing antidromic responses (<0.8 ms) after separate electrical stimulation of the three semicircular canal nerves or the lagenar nerve branch. Central neurons in the vestibular nuclei were identified as 2° VNs by their monosynaptic responses to separate stimulation of the nerve branches. For electrical activation of the nerve branches, single constant current pulses (duration, 0.2 ms; threshold, 1.5–3.1 μ A) were applied across individually adjusted suction electrodes (diameter, 120–150 μ m). The use of this electrode type facilitated the isolation of the individual nerve branches without current spread to other labyrinthine nerve branches. Pulses were produced by a stimulus isolation unit (World Precision Instruments A 360).

Glass microelectrodes used for extracellular and intracellular recordings were made with a horizontal puller (P-87 Brown/Flaming). Electrodes for extracellular field potential recordings were beveled (30°, ~20 μ m tip diameter) and filled with a 2 M solution of sodium chloride (~1 M Ω final resistance). Electrodes for intracellular recordings were filled with a mixture of 2 M potassium acetate and 3 M potassium chloride

(10:1), which gave a final resistance of ~90–110 M Ω . Neuronal recordings were made in bridge mode (SEC-05L; NPI Electronic).

At the beginning of each experiment, presynaptic and postsynaptic field potentials evoked by separate stimulation of the labyrinthine nerve branches were recorded at a standard reference site in the vestibular nuclei to optimize the position of the stimulus electrodes and to determine the stimulus threshold (T) for each nerve branch (Straka et al., 1997, 2002). Stimulus intensities were indicated as multiples of the threshold values for the postsynaptic field potentials. Vestibular neurons were recorded in all vestibular subnuclei (lateral, superior, descending, and medial), except the most medial parts of the medial vestibular nucleus. Based on the differential discharge patterns during long positive current steps, frog 2° VNs were distinctly distinguished into phasic or tonic vestibular neurons (Straka et al., 2004; Beranek et al., 2007). As reported previously, most of the vestibular neurons in the isolated frog brain had no spontaneous discharge at resting membrane potential (Straka and Dieringer, 2004; Straka et al., 2005). Only neurons with a membrane potential more negative than -55 mV were included in this study.

A differential processing of synaptic signals in phasic and tonic type 2° VNs was studied by applying stimulus trains of single current pulses to the labyrinthine nerve branch, which were as close as possible to naturally occurring vestibular afferent input patterns. The trains consisted of individual pulses with interstimulus frequencies that were sinusoidally modulated up to a variable maximal frequency. The timing of the single pulses in the train and the maximal peak frequency was obtained from the discharge pattern of frog horizontal canal afferent fibers during sinusoidal vertical axis rotation (see Fig. 1A) (Blanks and Precht, 1976). The imitation of a natural vestibular afferent discharge by an electrical stimulus train applied to labyrinthine nerve branches in the isolated whole brain *in vitro* is an approximation and restricted by differences in the synchronicity of the evoked discharge in the population of recruited afferent fibers and the activated fiber spectrum compared with the *in vivo* situation. However, this particular stimulus paradigm provides an excellent way to bridge the gap between *in vivo* studies of vestibulo-ocular functionality and *in vitro* single-cell studies of intrinsic membrane properties of 2° VNs.

For the transformation of the afferent activity *in vivo* into a stimulus train, the discharge of an afferent fiber to sinusoidal head acceleration at 0.2 Hz ($\pm 20^{\circ}$) was fitted with a sine wave function (see Fig. 1A₁). Because the resting discharge of this as of most other vestibular nerve afferent fibers in frog is very low (<2–10 spikes/s) (Blanks and Precht, 1976; Dieringer and Precht, 1977), the sine wave was only fitted for the activation half cycle. This sine wave function was transformed into a sequence of single events with sinusoidally modulated intervals and peak frequencies of 40, 70, 100, 150, or 200 Hz for different sets of experiments (see Fig. 1A₂). This sequence was applied during the first half cycle of a sine wave and was followed by a second half cycle without stimuli (see Fig. 1A₃). These electrical pulse trains were applied multiple times (8–20 cycles) to those semicircular canal or the lagenar nerve branches that were monosynaptically connected to the recorded 2° VNs. In the following, this stimulation will be denoted as "sinusoidal pulse train."

Each single pulse generated one spike in afferent fibers and evoked monosynaptic EPSPs in 2° VNs. Synaptic compound responses in phasic and tonic 2° VNs were formed by the temporal summation of the evoked individual monosynaptic EPSPs. These compound responses were characterized by several stimulus parameters, such as stimulus peak frequency (40, 70, or 100 Hz), half-cycle length (0.25, 0.5, 1, or 2.5 s), and single-pulse intensity (1.2 to 5 $\times T$). Amplitude and timing of the evoked responses were quantified in smoothed fits of the compound responses (see Fig. 2D, E, red lines). A compound response peak advance (+) or lag (-) relative to stimulus peak frequency was determined as the time between compound response peak and stimulus peak frequency and converted into degrees. The conversion allowed comparing the results obtained at different half-cycle lengths.

A contribution of glycinergic and GABAergic inhibitory circuits to the processing of synaptic signals in 2° VNs was studied by bath application of strychnine (Sigma; 1 μ M) and bicuculline (Sigma; 1–5 μ M). Surgical removal of the cerebellum or pressure injection of 100–150 nl of lidocaine (Sigma; 2–5% in Ringer's solution) through a beveled injection

electrode (30°, 10–15 μm tip diameter) into the ipsilateral cerebellar peduncle was used to reveal a contribution of the cerebellum to the processing of afferent signals in 2°VNs.

Single sweeps of the responses were digitized (CED 1401; Cambridge Electronic Design), stored on computer, and analyzed off-line (Signal, Cambridge Electronic Design; and Matlab, MathWorks). Synaptic potentials were analyzed from averages of 8–20 single sweeps after electronic subtraction of the extracellular field potential recorded in the vicinity. Statistical differences in parameters were calculated according to the Mann–Whitney *U* test (unpaired parameters) and the Wilcoxon signed rank test (paired parameters; Prism, Graphpad Software). All averaged results are expressed as mean \pm SE. Graphical presentations were made with the aid of commercially available computer software (Origin, Microcal Software; Corel Draw, Corel).

Retrograde labeling of vestibular projection neurons and anterograde tracing of vestibular nerve afferent fibers (see Fig. 2A) helped to determine the location of neurons within the vestibular nuclear boundary in the isolated frog brain based on external landmarks. To outline the location of central vestibular neurons and the termination of vestibular nerve afferent fibers, crystals of Alexa Fluor 488 (green) or 546 dextran (red) were inserted unilaterally into the oculomotor nucleus or the upper spinal cord, or were placed on particular vestibular nerve branches in the periphery in isolated frog brains *in vitro*. After 48 h of survival at 9°C, brains were fixed in 4% paraformaldehyde in 0.1 M phosphate buffer (PB) for 24 h and stored overnight in 15 and 30% sucrose in 0.1 M PB. All brains were cut transversally in 60 μm sections on a cryostat. Sections were mounted on slides, coverslipped with Vectashield (Vector Laboratories; Biovalley), and analyzed by laser scanning confocal microscopy (Zeiss LSM 510) at a wavelength of 488 or 543 nm. Stacks of 10–20 confocal images were generated with a 20 \times /0.5 objective and a plan Apochromat 40 \times /1.3 oil-immersion objective. Images for Figure 2A were produced by horizontal projection of the entire stack.

Modeling of the synaptic processing in tonic and phasic 2°VNs was performed by extending previously described intrinsic neuronal models (Borg-Graham, 1991; Moore et al., 1995) with conductance-based synapses. Parameter estimation was based on frequency responses of representative phasic and tonic 2°VNs (Beranek et al., 2007). The estimation was done by a compartmental admittance formulation, which consisted of an active soma and one active dendrite with three compartments. All passive and active parameters were assumed to be uniformly distributed (Moore et al., 1995; Murphey et al., 1995). Parameters were estimated using a compartmental admittance formulation in Matlab (MathWorks). Real-time compartmental models were simulated in NEURON (Carnevale and Hines, 2006) (for a detailed description, see the supplemental material, available at www.jneurosci.org).

Dual-exponential conductance-based synapses were added to the intrinsic single-cell compartmental models using the following equation: $I_{\text{sb}} = g_{\text{sb}} F [\exp(-t/\tau_2) - \exp(-t/\tau_1)](V_i - V_{\text{sb}})$ with τ_1 as rise and τ_2 as fall time constant (Johnston and Wu, 1994). The peak conductance for a single synaptic event was defined by g_{sb} ; V_{sb} indicates the reversal potential and V_i the current compartmental membrane potential. The scaling factor F is defined such that the peak of the dual exponential is 1. These synapses were implemented by the function “exp2syn” in the NEURON simulation environment, extended by an absolute synaptic refractory period (Hjelmstad et al., 1997). The values of the reversal potentials for excitatory ($V_{\text{se}} = 0$ mV) and inhibitory synapses ($V_{\text{si}} = -75$ mV) were obtained from Hille (2001). Two different parameter sets for synaptic innervation were used: the “E compartmental model” consisted of one excitatory synapse at the last dendritic compartment with the following parameters: $\tau_1 = 5$ ms, $\tau_2 = 97$ ms, $g_{\text{se}} = 16.8$ nS. To mimic the monosynaptic excitation, a delay of 3.4 ms (Biesdorf et al., 2008) from the stimulus to the onset of the excitation was used. For the “E/I compartmental model” the E compartmental model was extended by two inhibitory synapses at the soma: glycine ($\tau_1 = 2$ ms, $\tau_2 = 200$ ms, $g_{\text{si}} = 22.5$ nS) and GABA_A ($\tau_1 = 2$ ms, $\tau_2 = 91$ ms, $g_{\text{si}} = 16.8$ nS). All synaptic time constants and conductances were obtained by fitting published experimental data (Biesdorf et al., 2008). The inhibition for the stimulation paradigms 70 Hz/2.5 s (peak frequency/half-cycle length) in the model was activated by detected spike events of phasic or tonic neurons, using a

synaptic delay of 1.8 ms (Straka et al. 1997). For all other computations, the spike discharge of tonic 2°VNs has been generated from the 70 Hz/2.5 s stimulation paradigm.

Results

Discharge of vestibular nerve afferent fibers

Vestibular nerve afferent fibers ($n = 27$) during sinusoidal pulse-train stimulation of individual labyrinthine nerve branches (Fig. 1A₃) were recorded intracellularly to determine the maximal peak frequency at which each single pulse in the train was still able to evoke spikes. Recorded afferent fibers originated from the horizontal canal (HC; $n = 4$), the anterior vertical canal (AC; $n = 4$), the posterior vertical canal (PC; $n = 12$), or the lagena (LA; $n = 7$). Spikes were elicited by electrical pulse intensities between ~ 1.2 and $3 \times T$ of the afferent nerve-evoked field potential recorded in the vestibular nuclei (threshold, 1.5–3.1 μA). All pulses of the stimulus train evoked single spikes up to a peak frequency of ~ 100 Hz (Fig. 1B₁, B₂, C, inset for 40 and 100 Hz). Because each individual pulse evoked only one spike, the discharge in the afferent fibers had the same frequency modulation as the stimulus train. At a higher peak frequency, increasingly more single pulses of the train failed to evoke spikes (Fig. 1B₃, C, inset for 200 Hz). Although some fibers responded with an action potential to each single pulse up to peak frequencies of 150 Hz, the discharge reliability of the population of recorded afferent neurons decreased progressively for stimulus trains with peak frequencies > 100 Hz (Fig. 1C).

Because intracellular recordings of axons were likely biased toward larger fibers, the upper frequency for reliable firing during pulse trains are likely dominated by the results from the thickest vestibular nerve afferents. However, the amplitude of labyrinthine nerve-evoked presynaptic field potentials in the vestibular nuclei remained unchanged for stimulus frequencies up to 100 Hz *in vitro* (Biesdorf and Straka, 2004), indicating that most afferents can sustain a discharge up to this frequency, compatible with *in vivo* data (Blanks and Precht, 1976). Therefore, the maximal stimulus peak frequency was limited to 100 Hz in the present study to assure the faithful activation of spikes in all afferent fibers by each electrical pulse of the stimulus train. Because afferent fibers in our *in vitro* study were silent at rest, this electrical stimulus generated a defined presynaptic activity pattern in all afferents that terminate on a particular vestibular neuron. Thus, this electrical stimulus paradigm, which is based on the timing of the spike discharge of a vestibular nerve afferent fiber during a head movement *in vivo*, is well suited to reveal the dynamic processing of vestibular sensory signals in the different neuronal subtypes. Because frog phasic and tonic vestibular neurons receive monosynaptic inputs from a similar afferent fiber spectrum (Straka et al., 2004) any differences in the dynamics of the synaptic processing are unlikely to result from different afferent termination patterns on the two neuronal subtypes, but rather are caused by differences in intrinsic membrane and/or emerging network properties.

Identification and classification of frog vestibular neurons

Central vestibular neurons ($n = 110$) were recorded in the isolated frog brain throughout the rostrocaudal extent of the vestibular nuclei. Retrogradely labeled vestibulo-ocular (Fig. 2A₁, A₂) and vestibulospinal neurons after application of Alexa Fluor 546 dextran in the oculomotor nucleus, or the upper spinal cord and the labeled terminal field of vestibular nerve afferent fibers (Fig. 2A₃) outlined the location of the vestibular neurons in the dorsal hindbrain. Data on afferent and efferent vestibular connections

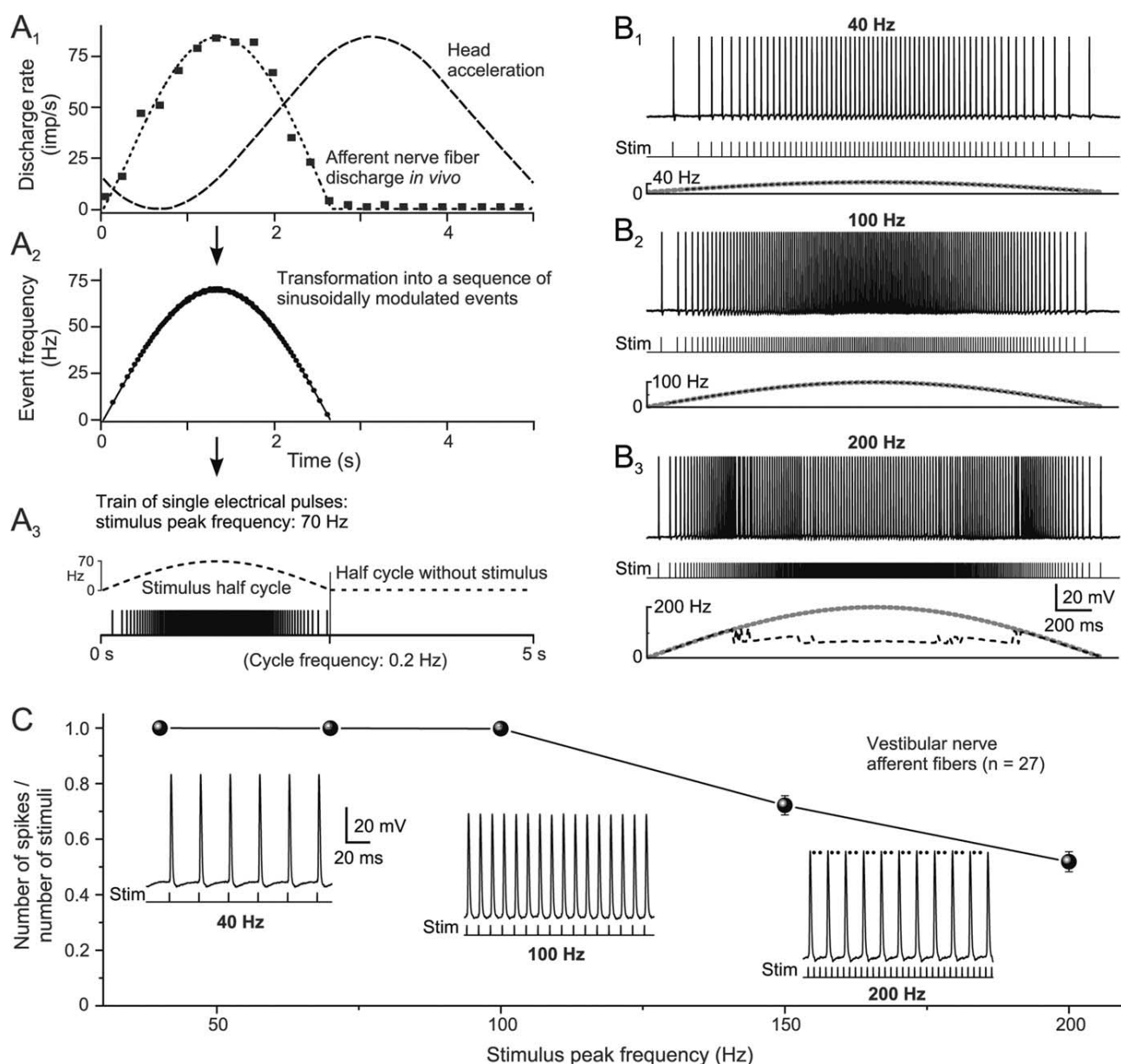


Figure 1. Discharge of vestibular nerve afferent fibers evoked by trains of single electrical pulses (sinusoidal pulse train). **A₁–A₃**, The discharge of a horizontal semicircular canal afferent fiber (■) recorded during a 0.2 Hz ($\pm 20^\circ$) sinusoidal rotation in frog *in vivo* (Blanks and Precht, 1976) was fitted with a sine wave function (dashed line in **A₁**), transformed into sinusoidally modulated sequences of events with modifiable peak frequencies (**A₂**, ●), and used as a template for pulse trains to electrically stimulate individual labyrinthine nerve branches (**A₃**). Because of the low resting discharge, only one half cycle was used for stimulation. **B₁–B₃**, Intracellular recorded spike discharge of a posterior vertical canal afferent fiber evoked by a sinusoidal pulse train (Stim) with peak frequencies of 40 (**B₁**), 100 (**B₂**), and 200 Hz (**B₃**); bottom traces in **B₁–B₃** indicate pulse trains, stimulus frequency (dotted gray line), and discharge rate (dashed black line). The calibration in **B₃** also applies to **B₁** and **B₂**. **C**, Ratio between the number of spikes and stimulus pulses (mean \pm SE) as a function of peak frequency (1 indicates that each single pulse of a train evokes one single spike). Insets, Spike discharge of the afferent fiber shown in **B₁–B₃** at peak frequencies of 40, 100, and 200 Hz at an extended time scale; at a peak frequency of 200 Hz, two of three stimuli failed to evoke spikes (black dots). The calibration for the trace at 40 Hz applies to all insets.

(Straka and Dieringer, 1991; Birinyi et al., 2001), as well as the location of vestibular projection neurons and the termination of vestibular nerve afferent fibers relative to external landmarks (e.g., entry of the eighth nerve into the brainstem; dorsal apex), served as clues for localizing the recording area for 2°VNs in the isolated frog brain.

Based on intrinsic membrane properties and discharge behavior in response to intracellular current injection, central VNs were classified as phasic or tonic neurons (Straka et al., 2004). As described previously, during injection of long positive current

steps, tonic VNs ($n = 15$; 13.6%) exhibited a continuous discharge throughout the current step (Fig. 2B) (Straka et al., 2004; Beraneck et al., 2007). In contrast, the larger population of phasic VNs ($n = 95$; 86.4%) responded with a short, high-frequency burst of one to three spikes within the first 50 ms (Fig. 2C), which unequivocally separated these neurons from tonic VNs. The difference in the evoked discharge pattern was paralleled by a significant difference ($p \leq 0.0001$; Mann–Whitney U test) in the input resistance between phasic ($11.8 \pm 3.1 \text{ M}\Omega$; $n = 42$) and tonic neurons ($21.5 \pm 3.9 \text{ M}\Omega$; $n = 11$). In contrast, the resting mem-

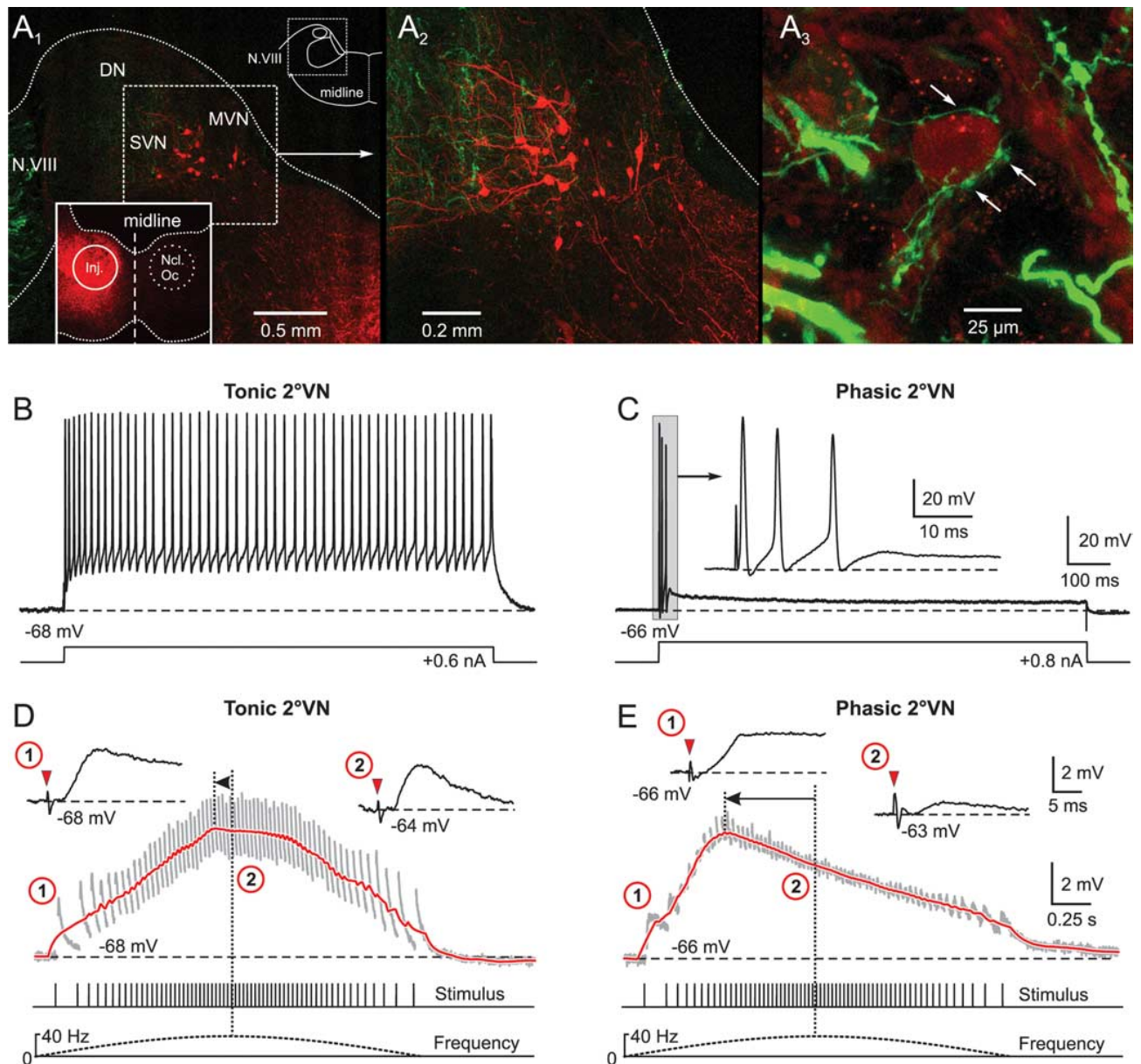


Figure 2. Synaptic compound responses evoked by pulse-train stimulation of semicircular canal nerves in identified central vestibular neurons. **A₁**, The location of retrogradely labeled vestibulo-ocular neurons in the superior vestibular nucleus (SVN) and MVN after injection of Alexa Fluor 546 dextran (red) into the ipsilateral oculomotor nucleus (Ncl. Oc.; inset) help determine the area for the recordings in the isolated frog brain. **A₂**, Higher magnification of labeled SVN and MVN vestibulo-ocular neurons located in the outlined area in **A₁**. **A₃**, AC afferent fibers, labeled in green from the periphery with Alexa Fluor 488 dextran, contact the soma (arrows) of a neuron in the SVN. **B, C**, A continuous discharge (**B**) and a short burst of three spikes (**C**) evoked by intracellular injection of long positive current steps (bottom traces) characterized tonic (**B**) and phasic 2°VNs (**C**), respectively. The inset in **C** shows the short initial burst (gray area) of the phasic 2°VN at an extended time scale. **D, E**, Compound responses formed by temporal summation of individual EPSPs (gray traces) after pulse-train stimulation of the AC nerve with a peak frequency of 40 Hz in the same tonic (**D**) and phasic 2°VN (**E**) as shown in **B** and **C**, respectively. The bottom traces indicate pulse train and stimulus frequency. Insets in **D** and **E** show EPSPs evoked by the first single pulse of the train (1) and by the single pulse at peak frequency (2) at an extended time scale; horizontal dashed lines in **B–E** indicate the membrane potential (−68 mV in **B, D**; −66 mV in **C, E**). Red arrowheads in insets in **D** and **E** indicate the single pulses. Red traces in **D** and **E** are smoothed fits of the compound responses; horizontal arrows indicate the advance of the compound response peak with respect to stimulus peak frequency (vertical dotted lines). Records in **B** and **C** are single sweeps, and in **D** and **E** are the average of 12 responses. Calibrations in **C** and **E** apply to **B** and **D**, respectively. DN, Dorsal auditory nucleus.

brane potential of the two subtypes were similar (phasic, -68.4 ± 12.3 mV, $n = 95$; tonic, -69.2 ± 9.2 mV, $n = 15$).

Recorded neurons in the vestibular nuclei were identified as second-order by an EPSP with a monosynaptic onset after electrical stimulation of a particular ipsilateral semicircular canal or the lagenar nerve (Fig. 2*D, E*, inset 1). This monosynaptic EPSP is the physiological correlate of the morphologically visualized synaptic connection between vestibular nerve afferent fibers and

central vestibular neurons (Fig. 2*A₃*, arrows). The criteria for the timing of monosynaptic responses have been described previously in detail (Straka and Dieringer, 1997). Accordingly, semicircular canal or lagenar nerve-evoked EPSPs with onset latencies between 2.7 and 4.5 ms were considered as monosynaptic. Based on this definition, the recorded 2°VNs could be distinguished as 2°HC ($n = 28$), 2°AC ($n = 32$), 2°PC ($n = 33$) and 2°LA ($n = 17$) neurons. Although many of these neurons received, in addition,

inputs with disynaptic or oligosynaptic latencies from one or more ipsilateral labyrinthine nerve branches, only the monosynaptic inputs were considered for further investigation.

Activation of second-order vestibular neurons with sinusoidal pulse trains

The responses of tonic and phasic 2° VNs to electrical stimulation of a particular vestibular nerve branch with a sinusoidal pulse train consisted of a temporal summation of the individual monosynaptic EPSPs evoked by each single pulse (Fig. 2*D,E*, gray traces). In tonic 2° VNs ($n = 14$), compound responses were rather symmetric with a slow rise and decay and an overall waveform that was approximately aligned with the stimulus frequency modulation (Fig. 2*D*, compare red solid and dashed lines below stimulus). Thus, the compound response peak in this neuronal type (Fig. 2*D*, vertical dotted lines, horizontal arrow) approximately matched the stimulus peak frequency or was slightly advanced (Fig. 2*D*, vertical dotted lines, arrowhead). In contrast, phasic 2° VNs ($n = 67$) showed a relatively rapid rise and an early decay of the compound response that created a considerable peak advance (Fig. 2*E*, vertical dotted lines, horizontal arrow) relative to the stimulus peak frequency (Fig. 2*E*, compare red solid and dashed lines below stimulus). This pronounced difference in compound response dynamics and response peak timing relative to stimulus waveform of tonic and phasic 2° VNs was characteristic and suggested a different postsynaptic signal processing in the two neuronal subtypes.

The different dynamics of compound responses in tonic and phasic 2° VNs were paralleled by differences in the behavior of the individual monosynaptic EPSPs during the pulse train (Fig. 2*D,E*, insets 1, 2). Compared with the first EPSP, the amplitudes of those evoked by the subsequent single pulses in tonic 2° VNs were moderately reduced during the stimulus train (Fig. 2*D*, compare insets 1, 2). In contrast, in phasic 2° VNs, the amplitudes of the individual EPSPs decreased considerably during the pulse train compared with the first EPSP (Fig. 2*E*, compare insets 1, 2) and reached a minimum at stimulus peak frequency. This difference is compatible with the differential impedance behavior of the two vestibular subtypes during membrane polarization (Berañeck et al., 2007). In particular, the marked reduction of the EPSP amplitude in phasic 2° VNs at stimulus peak frequency (Fig. 2*E*, inset 2) complies with the marked impedance decrease of these neurons during depolarization.

In the following, several parameters of the stimulus pulse train, such as peak frequency, cycle length, or single-pulse intensity were varied to reveal the postsynaptic response dynamics in 2° VNs during different labyrinthine afferent activity patterns. Although the activity in vestibular nerve afferents, evoked by the different stimulus pulse trains, is an approximation with respect to the synchronicity of the afferent activity pattern during natural head motion *in vivo* (Ramachandran and Lisberger, 2006; Hospedales et al., 2008), by its defined timing it facilitates the characterization of the neuronal mechanisms underlying a parallel processing of afferent signals in separate populations of central vestibular neurons.

Effect of stimulus train peak frequency

Compound responses in both tonic and phasic 2° VNs evoked by stimulus trains with successively larger peak frequencies (40, 70, and 100 Hz) had similar peak amplitudes but exhibited progressively larger peak advances when the peak frequency was augmented from 40 Hz to 70 and 100 Hz (Fig. 3*A₁–A₃, B₁–B₃*; Table 1). The mean advance of the response peak relative to stimulus

peak frequency increased to a similar extent in both types of 2° VNs (Fig. 3*E*; Table 1). However, independent of stimulus peak frequency, the advance was always significantly larger in phasic compared with tonic 2° VNs (Fig. 3*E*; Table 1). In most phasic 2° VNs, the compound response had a more pronounced truncation during pulse trains with higher peak frequencies (Fig. 3*B₂, B₃*, open triangles). This further accentuated the asymmetry of the compound responses and indicates that these neurons have a highly nonlinear synaptic processing of repetitive afferent vestibular inputs. Construction of the population mean responses (Fig. 3*C*) and smoothed fits (*D*) from the recordings of phasic ($n = 67$) and tonic 2° VNs ($n = 14$), respectively, confirmed the clear differences in postsynaptic signal processing of the two neuronal subpopulations.

Increasing the stimulus peak frequency from 40 Hz to 70 and 100 Hz did not only change the time course of the compound responses but also caused an increasingly larger reduction of the individual EPSP size in both tonic and phasic 2° VNs (Fig. 3*A₁–A₃, B₁–B₃, F*, gray traces; Table 1). This reduction was particularly prominent in phasic 2° VNs (Fig. 3*F₁, F₂*, compare plots) because EPSPs evoked by the single pulses at peak frequency of 100 Hz were on average <10% of the amplitude of the first EPSP (Fig. 3*F₂*; Table 1). This suggests the presence of powerful shunting mechanisms for afferent synaptic inputs, preferentially at high stimulus peak frequencies. This shunting likely contributes to the observed truncation of the compound response (Fig. 3*B₂, B₃*, open triangles) and the increased peak advance at higher peak frequencies. Although some shunting of single EPSPs was also observed in tonic 2° VNs, the maximal reduction (at 100 Hz peak frequency) was significantly less than in phasic 2° VNs (Fig. 3*F₁, F₂*; Table 1). Except for stimulus peak frequencies of 40 Hz the shunting effect on single EPSP size was always more pronounced in phasic compared with tonic 2° VNs (Table 1).

Effect of stimulus train length

Using stimulus train length as a variable but keeping peak frequency constant revealed a different dependency of both amplitude and timing of the compound response from this parameter in tonic and phasic 2° VNs (Fig. 4*A,B*). Compatible with the relatively linear transformation of presynaptic afferent activity into postsynaptic compound responses in tonic 2° VNs, the response peak almost doubled in amplitude when the stimulus train length (half cycle) was increased from 0.25 s to 2.5 s (Fig. 4*A₁–A₄, C₁*, open circles). This finding indicates that the temporal summation of individual EPSPs in tonic 2° VNs gradually increases with continuously larger numbers of single pulses in the train and confirms the notion of a mostly linear input–output relationship in this vestibular neuronal subtype. The substantial increase in compound response peak amplitude with increasing train length is accompanied by a considerable change in the timing of the response peak. Notably, the large peak lag of approximately -45° at a half-cycle length of 0.25 s changes into a peak advance of $\sim 20^{\circ}$ at a half-cycle length of 2.5 s (Fig. 4*C₂*, open circles). Accordingly, the compound response peak in tonic 2° VNs would be aligned with peak frequency at a half-cycle length of ~ 1.5 s (Fig. 4*C₂*, dotted arrow to bottom axis).

In phasic 2° VNs, the amplitude of the compound response evoked during a stimulus half cycle of 2.5 s increased only by $\sim 25\%$ compared with the response evoked with a stimulus half cycle of 0.25 s (Fig. 4*B, C₁*). This small increment in amplitude during a 10-fold extension in stimulus half-cycle length contrasts with the almost twofold increase in tonic 2° VNs (Fig. 4*C₁*). This is because of the relatively larger responses in phasic 2° VNs (75%)

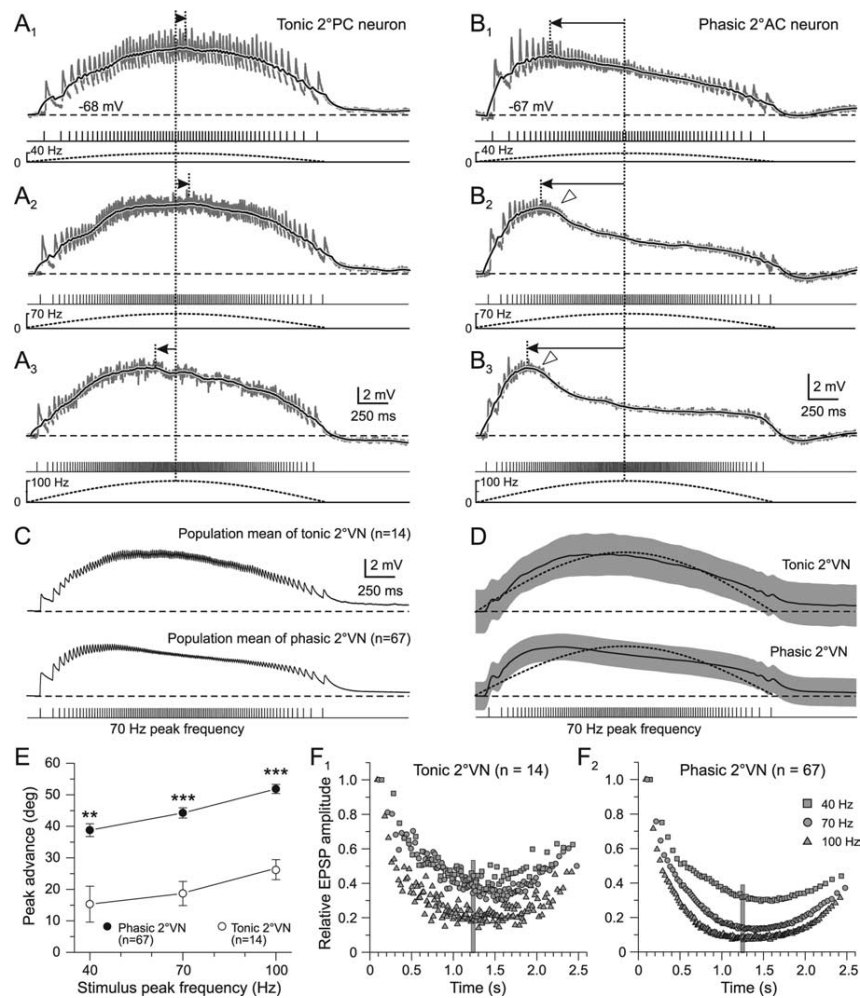


Figure 3. Compound synaptic responses as a function of stimulus train peak frequency in phasic and tonic 2° VNs. **A₁–B₃**, Compound responses formed by summation of single EPSPs (gray traces) in a tonic 2° PC (**A₁–A₃**) and a phasic 2° AC (**B₁–B₃**) neuron after pulse-train stimulation with a peak frequency of 40 (**A₁, B₁**), 70 (**A₂, B₂**), and 100 Hz (**A₃, B₃**). The black traces are smoothed fits of the compound responses; bottom traces show pulse trains (half-cycle duration, 2.5 s) and stimulus frequency modulation (dashed lines), respectively; horizontal dashed lines indicate the resting membrane potential (–68 mV in **A**; –67 mV in **B**) and horizontal arrows the lag/advance of the compound response peak with respect to stimulus peak frequency (vertical dotted lines). Synaptic responses in **A₁–B₃** are the averages of 12 single sweeps. Calibrations in **A₃** and **B₃** apply to **A₁, A₂** and **B₁, B₂**, respectively; open arrowheads in **B₂** and **B₃** mark the truncation of the compound response. **C, D**, Population mean of compound responses (**C**) and smoothed fits (**D**) evoked by pulse trains with 70 Hz peak frequency and 2.5 s half-cycle length in tonic ($n = 14$) and phasic 2° VNs ($n = 67$). The gray bands in **D** indicate \pm SE of the mean, the dotted curves indicate the stimulus modulation and the horizontal dashed lines the mean resting membrane potential of –69 mV in tonic and –68 mV in phasic 2° VNs. **E**, Advance (in degrees) of the compound response peak relative to stimulus peak frequency (mean \pm SE) in phasic (●) and tonic 2° VNs (○) as a function of stimulus peak frequency. $^{**}p \leq 0.001$, $^{***}p \leq 0.0001$, significant difference between tonic and phasic 2° VNs (Mann–Whitney U test). **F₁, F₂**, Average amplitude of individual EPSPs evoked by the single pulses of the train with peak frequencies of 40 (□), 70 (○), and 100 Hz (△) in tonic (**F₁**) and phasic 2° VNs (**F₂**). Amplitudes were normalized to the size of the first EPSP. Plots of \pm SE were omitted for clarity; vertical gray bars mark the timing of the stimulus peak frequency.

at a half-cycle length of 0.25 s compared with tonic 2° VNs (55%) (Fig. 4C₁). The larger amplitudes in phasic 2° VNs during short stimulus trains (0.25 s) and the rather small increment with increasing train length can be explained by the relatively rapid rise of the compound response generating the considerable peak advance (Figs. 2E, 3B). This small increase in peak amplitudes for half-cycle lengths between 0.25 and 2.5 s, however, is contrasted by a large simultaneous change of peak timing, which exceeded that of tonic 2° VNs (Fig. 4C₂). The considerable response peak lag of approximately -35° at a half-cycle length of 0.25 s changed into a peak advance of $\sim 45^{\circ}$ at a half-cycle length of 2.5 s (Fig.

4C₂, filled circles). Calculation of the stimulus half-cycle length at which compound responses in phasic 2° VNs were aligned with stimulus peak frequency yielded a value of ~ 0.7 s (Fig. 4C₂, dotted arrow to the bottom axis). This time is considerably shorter than that in tonic 2° VNs (~ 1.5 s) and again attributable to the faster slope of the compound response during the first few stimuli of the train (Figs. 2E, 3B). Moreover, it complies with the notion that phasic 2° VNs are particularly suitable for the detection of short, high-frequency components, whereas tonic 2° VNs are better suited to the processing of low-frequency components.

Effect of single stimulus pulse intensity

Higher-intensity single current pulses applied to the vestibular nerve branches recruit increasingly more afferent fibers. This recruitment causes larger amplitudes of all individual monosynaptic EPSPs (Fig. 5A–F, inset 1) and consequently compound responses with larger peak amplitudes in both tonic (Fig. 5A–C) and phasic 2° VNs (Fig. 5D–F). With larger intensities of all single pulses of a train [$1.3 \times T$ (Fig. 5A), $1.8 \times T$ (B), and $3.1 \times T$ (C)], the compound responses evoked by stimulus trains with low-intensity single pulses increased and action potentials were triggered in tonic 2° VNs as soon as the spike threshold was reached. The number of evoked spikes during the train stimulation depended on the subthreshold compound response amplitude but consistently was largest around peak stimulus frequency (Fig. 5B, C, insets 2). This indicates that in tonic 2° VNs ($n = 10$) the evoked discharge is rather linearly related to the underlying synaptic membrane depolarization as for intracellular injected currents (Straka et al., 2004). This effect became more evident when the relative spike discharge rate during the stimulus train (peak frequency, 70 Hz; train half-cycle length, 2.5 s; single-pulse intensity, $>2.5 \times T$) was plotted as a function of time (Fig. 5G₁). The maximal spike discharge rate occurs slightly before stimulus train peak frequency (Fig. 5G₁, arrow) and corresponds with the peak advance of the subthreshold compound response (Fig. 3C). Thus, the spike discharge in these neurons that more or less mirrors the stimulus frequency modulation has a rather tight correlation with the synaptic depolarization.

In phasic 2° VNs, stimulus-train-evoked compound responses changed from a symmetric waveform at low-intensity single pulses [e.g., $1.4 \times T$ (Fig. 5D)] to a skewed response at high-intensity single pulses [$2.0 \times T$ (Fig. 5E) and $3.2 \times T$ (F)]. Most importantly however, in all phasic 2° VNs ($n = 31$), only a small number of action potentials (approximately one to six) were evoked during the first 10–15 single pulses of the stimulus train

Table 1. Timing of the compound response peak and reduction of amplitudes of single EPSPs during pulse-train stimulation in phasic and tonic 2°VN

Stimulus peak frequency	Tonic 2°VNs		Phasic 2°VNs	
	Peak advance relative to stimulus peak frequency	Relative size of single EPSPs at stimulus peak frequency	Peak advance relative to stimulus peak frequency	Relative size of single EPSPs at stimulus peak frequency
40 Hz	15 ± 5° (9)*	46 ± 10%, n.s. (9)	38 ± 2° (36)	35 ± 2% (36)
70 Hz	19 ± 3° (14)*	38 ± 9% (14)*	44 ± 2° (67)	14 ± 1% (67)
100 Hz	26 ± 3° (9)*	23 ± 3% (9)**	53 ± 1° (40)	8 ± 1% (40)

Single EPSP amplitudes at stimulus peak frequencies (40, 70, and 100 Hz) are indicated as a percentage (mean ± SE) of the EPSP evoked by the first pulse in the stimulus train. The timing of the compound response peak is indicated relative to the peak frequency. n.s., Not significant. The number of neurons (*n*) is shown in parentheses.

* $p \leq 0.01$; ** $p \leq 0.001$, significant difference (Mann–Whitney *U* test) between parameters of phasic and tonic 2°VN.

(Fig. 5*E,F*, insets 2). Even with larger single-pulse intensity ($>5 \times T$) no further increase in spike number or spiking after the first 15 pulses was observed. This is illustrated by plotting the relative spike discharge rate during the stimulus train (Fig. 5*G*₂). The likelihood for spike triggering is maximal at the third single pulse of the train (Fig. 5*G*₂, arrow). This temporal limitation of evoked spikes is compatible with the pronounced peak advance of the subthreshold compound response (Fig. 3*E*) and is likely related to the substantial shunting of single EPSPs after the response peak is reached (Fig. 3*F*₂).

The differential temporal pattern of synaptically evoked spikes in phasic and tonic 2°VNs (Fig. 5*G*₃) was quantified by calculating the stimulus cycle frequency at which the maximal discharge rate (Fig. 5*G*₁, *G*₂, arrows) coincides with the stimulus peak. The maximal discharge rate matches the stimulus peak frequency at a cycle frequency of ~1 Hz in phasic and ~0.25 Hz in tonic 2°VNs (Fig. 5*G*₁, *G*₂). Accordingly, the differential synaptic spike discharge behavior in phasic and tonic 2°VNs (Fig. 5*G*₃) is compatible with the different intrinsic filter properties and suggests a preferential processing of high- and low-dynamics vestibular afferent signals in the two neuronal subtypes, respectively (Beraneck et al., 2007).

Inhibitory neuronal circuits control afferent synaptic signal processing in phasic 2°VNs

The early truncation of the compound responses and the marked reduction of single EPSP amplitudes that likely contributes to the peak advance in phasic 2°VNs might not only be caused by prominent voltage-dependent potassium conductances (Beraneck et al., 2007), but also by inhibitory synaptic inputs superimposed on the afferent-evoked monosynaptic excitation (Biesdorf et al., 2008). A potential contribution of glycinergic and GABAergic IPSPs to the nonlinear characteristics of compound responses in phasic 2°VNs was studied by bath application of the respective transmitter antagonists (Fig. 6*A,C*). Appli-

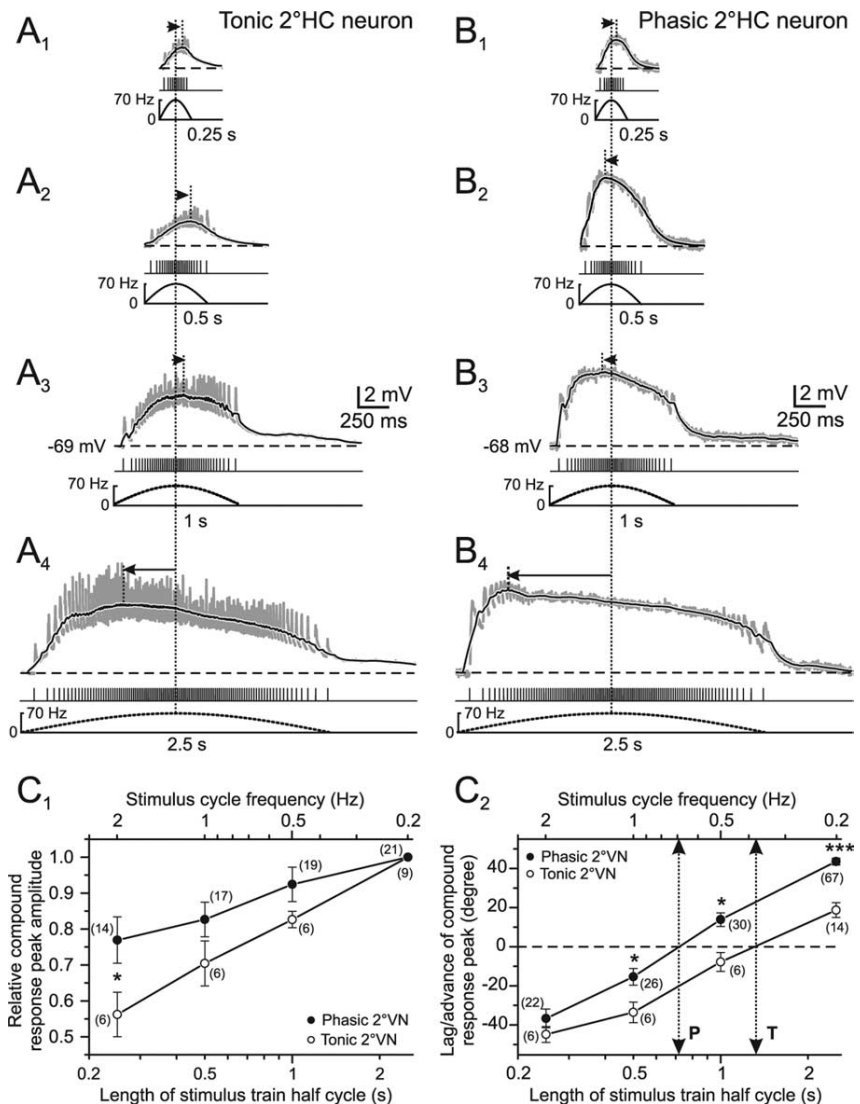


Figure 4. Compound synaptic responses as a function of stimulus pulse train length in phasic and tonic 2°VNs. *A*₁–*B*₄, Compound responses of single EPSPs (gray traces) in a tonic (*A*₁–*A*₄) and a phasic (*B*₁–*B*₄) 2°HC neuron after pulse-train stimulation with 0.25 (*A*₁, *B*₁), 0.5 (*A*₂, *B*₂), 1 (*A*₃, *B*₃), and 2.5 s (*A*₄, *B*₄) half-cycle length. The peak frequency was 70 Hz and pulse intensity was $1.8 \times T$ in *A* and $1.7 \times T$ in *B*. Black traces are smoothed fits of the compound responses; bottom traces show pulse trains and stimulus frequency (dashed lines), respectively; horizontal dashed lines indicate the membrane potential (−69 mV in *A*; −68 mV in *B*) and horizontal arrows indicate the lag/advance in degree of the compound response peak with respect to stimulus peak frequency (vertical dotted lines). All records are the average of 12 responses. Calibrations in *A*₃ and *B*₃ apply to all other traces. *C*₁, *C*₂, Mean (±SE) of compound response peak amplitude (*C*₁) and peak lag/advance relative to stimulus peak frequency (*C*₂) of tonic (○) and phasic 2°VNs (●) as a function of stimulus half-cycle length (bottom axis) and corresponding full stimulus cycle frequency (top axis). Amplitudes in *C*₁ were normalized to those obtained at a stimulus half-cycle length of 2.5 s; dotted two-sided arrows indicate half-cycle length and corresponding full-cycle frequency where response peak and stimulus peak frequency are aligned (0°; dashed horizontal line) in tonic (T) and phasic (P) 2°VNs. The number of neurons is indicated in parentheses. * $p \leq 0.05$, *** $p \leq 0.0001$, significance of difference between tonic and phasic neurons (Mann–Whitney *U* test).

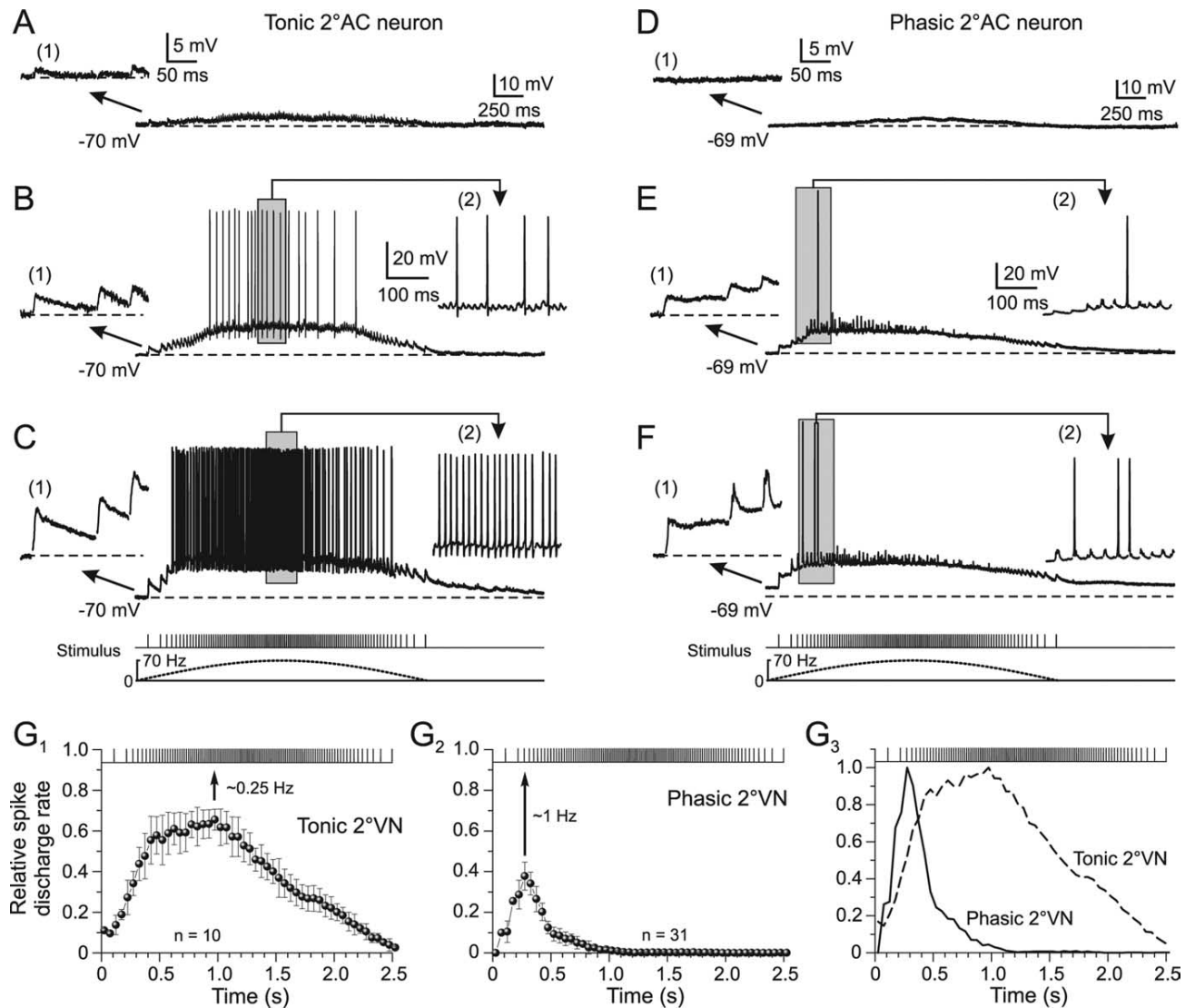


Figure 5. Synaptic discharge dynamics as a function of stimulus pulse intensity in phasic and tonic 2°VNs. *A–F*, Compound responses and superimposed spikes in a tonic (*A–C*) and a phasic (*D–F*) 2°AC neuron after stimulation with sinusoidal pulse trains at a peak frequency of 70 Hz. The intensities for the single pulses were in the tonic 2°AC (*A*, $1.3 \times T$; *B*, $1.8 \times T$; *C*, $3.1 \times T$) and in the phasic 2°AC neuron (*D*, $1.4 \times T$; *E*, $2.0 \times T$; *F*, $3.2 \times T$); the first three single EPSPs of the train (1) and during the indicated period (gray area) of spike discharge (2) in *A–F* are shown at an extended time and amplitude scale; bottom traces in *C* and *F* show pulse trains (half-cycle duration, 2.5 s) and stimulus frequency (dashed lines) that also apply to *A*, *B* and *D*, *E*, respectively. Horizontal dashed lines indicate the membrane potential (-70 mV in *A–C*; -69 mV in *D–F*); records in *B*, *C* and *E*, *F* are single sweeps and in *A* and *D*, the average of 12 responses, respectively. Calibrations in *A* and *D* and insets (1) therein apply also to *B*, *C* and *E*, *F*, respectively; calibration in insets (2) in *B* and *E* apply also to insets (2) in *C* and *F*, respectively. *G*₁–*G*₃, Relative rate of evoked spike discharge (mean \pm SE) during pulse trains with peak frequencies of 70 Hz in tonic (*G*₁) and phasic 2°VNs (*G*₂) at single-pulse intensity $>2.5 \times T$. The relative rate was calculated from the number of spikes in each cell during the stimulus train in 50 ms bins and divided by the number of stimuli within the respective bin. The discharge in phasic 2°VNs is confined to the first 10–15 single pulses of the train (*G*₂, solid line), whereas in tonic 2°VNs it is more aligned with the frequency modulation of the single pulses (*G*₂, dashed line). Curves in *G*₃ were obtained by normalization to the peaks in *G*₁ and *G*₂, respectively. Peak discharge rate in tonic and phasic 2°VNs (*G*₁, *G*₂, arrows) corresponds to a full stimulus cycle of ~ 0.25 and ~ 1 Hz, respectively.

cation of the glycine receptor antagonist strychnine ($1 \mu\text{M}$; $n = 7$) or the GABA_A receptor antagonist bicuculline ($1\text{--}5 \mu\text{M}$; $n = 8$) caused a significant reversible increase of the compound response amplitude by ~ 2 mV and a decrease of the mean peak advance by $>20^\circ$ compared with controls (Fig. 6*A, C, H, I*). Moreover, the observed reduction of single EPSP amplitudes during the stimulus train in controls became smaller after application of both transmitter antagonists (Fig. 6*B, D*). Although, this effect was significant only after blocking the GABAergic transmission (Fig. 6*D*, asterisk), it suggests that at least part of the observed shunting during the stimulus train was caused by inhibitory inputs. Probable neuronal candidates for mediating the glycinergic and GABAergic inhibition are ipsilateral vestibular inhibitory inter-

neurons (Straka and Dieringer, 1996) that have been shown to activate disynaptic IPSPs in phasic, but not in tonic 2°VNs after electrical stimulation of vestibular nerve afferent fibers (Biesdorf et al., 2008). An ipsilateral origin was confirmed by the recordings of several phasic 2°VNs ($n = 6$) in isolated frog brains in which the midline was completely transected from the optic tectum to the obex. The peak advance of the compound responses of these neurons was identical to those of controls, thereby excluding commissural connections as the source of the inhibition.

The larger effect of bicuculline with respect to strychnine on the shunting of single EPSP amplitude during the pulse-train stimulus suggests that GABAergic inputs might be either more effective or more numerous. However, GABAergic IPSPs from

inhibitory vestibular interneurons have shorter time constants than glycinergic IPSPs (Biesdorf et al., 2008), suggesting that additional GABAergic circuits might be recruited by the pulse-train stimulation in the present study. Because all experiments were performed in the isolated frog brain in which the cerebellum was attached (Fig. 6G), it is possible that the activation of vestibular nerve afferent fibers recruits the cerebellar circuitry and thereby evokes Purkinje-cell-mediated GABAergic IPSPs (Magherini et al., 1975) in phasic 2° VNs. Pressure injection of 100–150 nl of 2% lidocaine ($n = 16$) into the ipsilateral cerebellar peduncle (Fig. 6G) that blocks the activation of the cerebellar circuitry provoked, in some of the phasic 2° VNs ($n = 7$ of 16), a reversible increase of the compound response amplitude by ~ 1 mV as well as a reduction of the peak advance by $\sim 25^{\circ}$ compared with controls (Fig. 6E, H, I), but had no effect in others ($n = 9$ of 16). The accompanying reduction of the shunt of single EPSP amplitudes during the stimulus pulse train, however, was not significant (Fig. 6F). A spread of pressure-injected lidocaine from the cerebellum into the vestibular nuclei as a potential explanation of the effect was ruled out because the amplitude of the monosynaptic EPSPs in the 2° VNs ($n = 16$), as well as of presynaptic and postsynaptic vestibular afferent field potential components (verified in control experiments) after single electrical pulse stimulation did not decrease. This amplitude constancy served as an indication that no block of action potentials in vestibular afferent fibers occurred within the vestibular nuclei. The effects on the compound response after injection of lidocaine into the cerebellum were confirmed in experiments where phasic 2° VNs ($n = 18$) were recorded in isolated whole brains ($n = 4$) in which the cerebellum was removed. In fact, the peak advance of compound responses in phasic 2° VNs recorded in these preparations was significantly reduced by $\sim 20^{\circ}$ in 12 of the 18 neurons compared with controls (Fig. 6I).

Modeling approach to reveal cellular and network contributions for signal processing in 2° VNs

To differentiate between contributions of intrinsic membrane properties and the properties of network circuitry in shaping postsynaptic signals in 2° VNs, a modeling approach was used. Minimal models consisting of a soma and a three compartmental dendrite with uniformly distributed conductances were generated from frequency domain data of tonic and phasic 2° VNs (Fig. 7) (for details, see the supplemental ma-

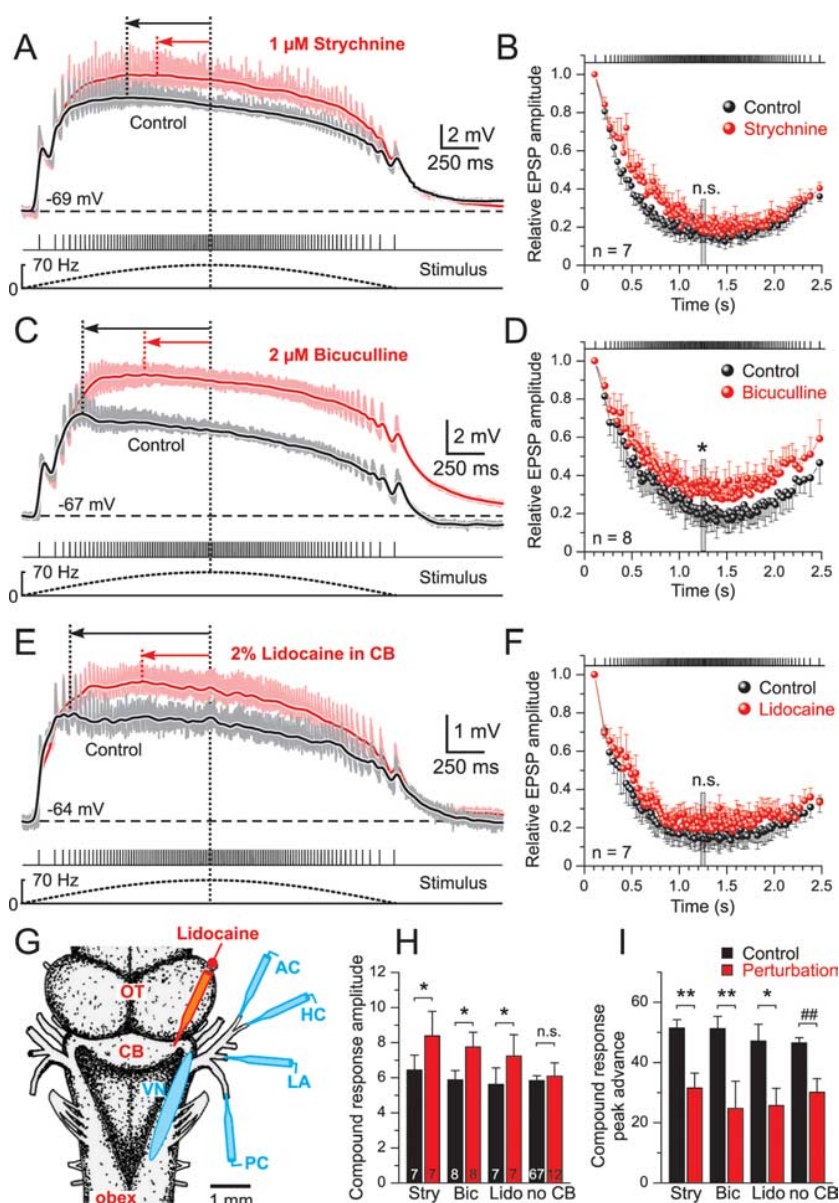


Figure 6. Inhibitory control of compound synaptic responses in phasic 2° VNs. **A, C, E**, Effect of blocking the glycinergic (strychnine, **A**) and GABAergic transmission (bicuculline, **C**) and the cerebellar output (100–150 nl of lidocaine in CB, **E**) on amplitude and timing of the compound responses in three different phasic 2° VNs. Responses were evoked by stimulation of the anterior vertical (**A, E**) or horizontal semicircular canal nerves (**C**) with sinusoidal pulse trains of 70 Hz peak frequency. The black and red traces are smoothed fits of the compound responses (gray and pink traces); bottom traces show pulse trains (half-cycle duration, 2.5 s) and stimulus frequency (dashed lines), respectively; horizontal dashed lines indicate membrane potentials (-69 mV in **A**; -67 mV in **C**; -64 mV in **E**), and black and red horizontal arrows the peak advance relative to stimulus peak frequency (vertical dotted lines). All records are the average of 12 responses. **B, D, F**, Amplitudes (mean \pm SE) of individual EPSPs evoked by single pulses of the train before (black) and after (red) drug application; amplitudes were normalized to the first EPSP, respectively. Vertical gray bars mark the timing of stimulus peak frequency. **G**, Schematic drawing illustrating the stimulation of individual vestibular nerve branches, the vestibular nuclei, and the site for injection of lidocaine into the ipsilateral cerebellar peduncle. **H, I**, Amplitude (**H**) and timing (**I**) of the compound response peak (mean \pm SE) before and after application of strychnine (Stry), bicuculline (Bic), pressure injection of lidocaine (Lido) into the ipsilateral cerebellar peduncle, or after surgical removal of the cerebellum (no CB). * $p \leq 0.05$, ** $p \leq 0.01$, significance of difference before and after drug application (Wilcoxon signed-rank test); ## $p \leq 0.01$ (Mann–Whitney U test), significance between controls and 2° VNs recorded after the removal of the cerebellum. n.s., Not significant; CB, cerebellum; OT, optic tectum.

terial, available at www.jneurosci.org). Compatible with previous results (Beraneck et al., 2007), a noninactivating sodium conductance was required to obtain the observed increase in impedance with depolarization in tonic 2° VNs (Fig. 7A). In contrast, for

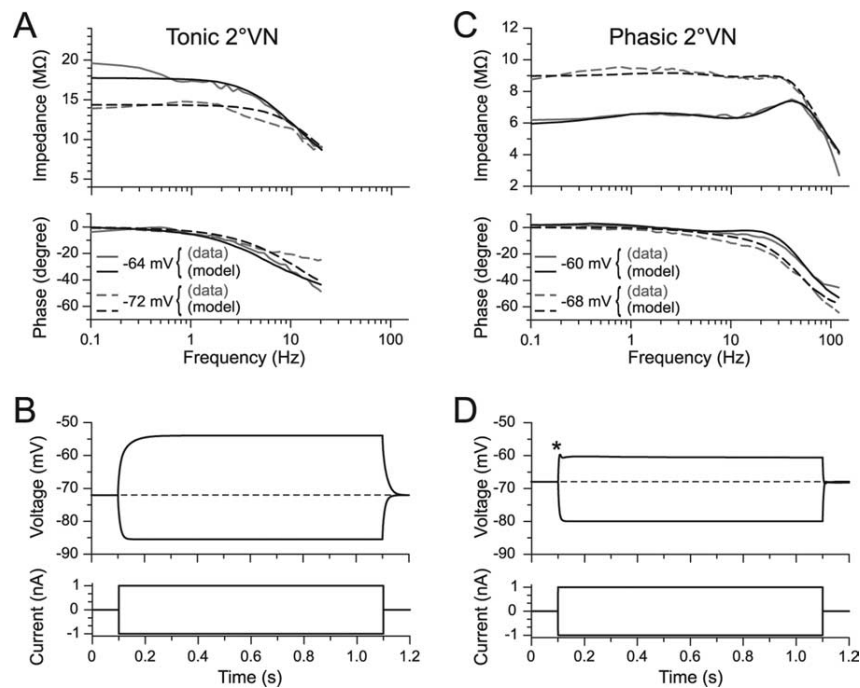


Figure 7. Frequency responses of tonic and phasic compartmental models of 2° VNs superimposed on magnitude and phase data used for parameter estimation. **A, C**, Impedance and phase functions of tonic (**A**) and phasic 2° VNs (**C**) at two different membrane potentials, computed from published data (Beraneck et al., 2007). Gray curves indicate data and black curves are tonic and phasic neuronal model fits using parameter estimation methods described previously (Saint-Mieux and Moore, 2000). For cell parameter values, see the supplemental material (available at www.jneurosci.org as supplemental material). **B, D**, Reconstruction of real-time current step responses of the tonic (**B**) and the phasic model neuron (**D**) using the compartmental models with respective parameters; the asymmetry between depolarizing and hyperpolarizing responses of the phasic neuron model (**D**) as well as the characteristic initial transient in response to positive current steps (**D**, asterisk) matches the real data (Straka et al., 2004).

phasic 2° VNs, an inactivating potassium conductance (Bekkers and Delaney, 2001) as well as a delayed rectifier was required to quantitatively describe the particular potential dependence of the resonance behavior (Fig. 7C). Using parameters derived from the impedance data, simulations with the three compartment cable model (Fig. 7B, D) adequately predicted membrane potential responses to current steps, including a depolarization-induced damped oscillation in phasic 2° VNs (Fig. 7D, asterisk). The similar responses of model and frog phasic 2° VNs supports the particular role of the potassium conductances in generating the distinct resonance and the dynamic response pattern of this neuronal vestibular subtype (Straka et al., 2004; Beraneck et al., 2007).

The role of intrinsic cellular properties in causing the observed dynamics of synaptic compound responses was tested by extending the “single-neuron models” of tonic and phasic 2° VNs by excitatory conductance-based synapses (*E* compartmental model) (for parameters, see Material and Methods). This allowed mimicking the repetitive synaptic excitation of 2° VNs by vestibular nerve afferent fibers as performed in the present study. Calculation of the synaptic compound response characteristics as a function of different stimulus parameters shows that these extended single-neuron models yield results (Fig. 8A₁, A₂, filled circles, open circles) that were at least qualitatively similar to the obtained data, illustrating the functional consequences of the different dynamic properties of phasic and tonic 2° VNs. Therefore, the characteristic intrinsic cellular properties contribute to some extent to the observed differences in compound response peak timing of the two vestibular neuronal subtypes (Fig. 8A₁, A₂, filled

circles, open circles). However, the assumed cellular properties in the model were not sufficient to account for the precise response characteristics as e.g., the large peak advance seen in phasic 2° VNs (Figs. 3C, 4C₂).

Based on the experimental results concerning inhibitory inputs from ipsilateral vestibular networks in phasic but not tonic 2° VNs after electrical nerve stimulation (Biesdorf et al., 2008), a combination of excitatory and superimposed inhibitory synapses was added to the single-neuron model (*E/I* compartmental model). All parameters related to amplitude and time course of monosynaptic afferent excitation and disynaptic GABAergic and glycinergic IPSPs (for details, see Material and Methods and supplemental material, available at www.jneurosci.org) have been adapted to values obtained from empiric experiments (Biesdorf et al., 2008). This procedure allowed the generation of model fits of single-pulse-activated afferent monosynaptic EPSPs and superimposed disynaptic GABAergic and glycinergic IPSPs (Fig. 8B). The estimated EPSP and IPSP parameters were used to reconstruct compound responses after pulse-train stimulation at a stimulus peak frequency of 70 Hz and half-cycle length of 2.5 s (Fig. 8C₁). The assumption of conductance-based inhibitory synapses yielded model response values similar to

those of real frog phasic 2° VNs (compare Fig. 8A₁, A₂, filled squares, with 3E, 4C₂). After turning off the glycinergic and GABAergic inhibition, the reconstructed model compound responses show that these components are particularly important for the timing of the response in phasic 2° VNs and considerably enhance the peak advance caused by the intrinsic cellular properties (Fig. 8C₁). This indicates that the particular response dynamics of this neuronal subtype originate from both the intrinsic membrane properties as well as the emerging properties of the inhibitory synaptic circuitry in which these neurons are embedded.

Previous studies have shown that the disynaptic GABAergic and glycinergic IPSPs in phasic 2° VNs are mediated by inhibitory neurons in the ipsilateral vestibular nucleus (Straka and Dieringer 1996, 2000; Biesdorf et al., 2008). To obtain realistic reconstructions of control model responses of phasic 2° VNs after pulse-train stimulation (compare Fig. 8C₁, control, with 3C), it was necessary to assume that both GABAergic and glycinergic inhibitory neurons fire spikes during pulse-train stimulation with a pattern typical for tonic 2° VNs (Fig. 8D₁). Using the alternative assumption, i.e., that the disynaptic inhibition is exclusively mediated by neurons with discharge patterns typical for phasic 2° VNs (Fig. 8D₂), the resulting model compound response exhibited a dynamics (Fig. 8C₂, black trace) that is incompatible with the experimental data (compare Fig. 8C₁, control). The delayed rapid increase in the response amplitude (Fig. 8C₂, arrowhead) was caused by the restricted effect of the inhibition in the model response attributable to the temporally limited discharge of the hypothetical phasic inhibitory neurons (Fig. 8D₂).

The testable prediction from this modeling approach in future studies thus is that tonic ipsilateral vestibular neurons mediate the observed disynaptic inhibition onto phasic 2°VNs.

Discussion

Frequency-modulated electrical pulse-train stimulation of individual vestibular nerve branches activated synaptic responses in frog tonic and phasic 2°VNs with distinctly different profiles. The mostly linear transformation of the presynaptic afferent activity into postsynaptic responses in tonic 2°VNs complies with the linear intrinsic properties and low-pass filter characteristics of these neurons and suggests an implication in the processing of low-dynamic, tonic components of head motion. In contrast, responses of phasic 2°VNs exhibited highly asymmetric profiles because of distinct bandpass filter properties and the impact of inhibitory inputs from vestibular and cerebellar circuits. Accordingly, phasic 2°VNs form adequate central vestibular elements optimized for processing of high-dynamic, nonlinear head motion components.

Limitations of the stimulus paradigm

Vestibular afferent fibers cover a broad spectrum of response dynamics during head rotation (Goldberg, 2000). The heterogeneity in afferent spiking during natural activation causes an asynchronous postsynaptic input in 2°VNs that is important for the high-fidelity linear response behavior of the vestibulo-ocular reflex (VOR) (Ramachandran and Lisberger, 2006; Hospedales et al., 2008). The sinusoidally modulated electrical pulse trains in the present study cause mainly synchronized vestibular afferent activity. Thus, imitation of head motion-related afferent discharge *in vitro* is an approximation with respect to presynaptic discharge timing and recruited fiber spectrum. However, it facilitates investigating the transformation of well-defined presynaptic vestibular afferent activity into postsynaptic responses of tonic and phasic 2°VNs. Thus, the use of *in vivo* discharge patterns as a template for electrical stimulation *in vitro* is well suited to understand the cellular basis for a differential processing of vestibular sensory signals in 2°VNs.

Coadaptation of intrinsic membrane and emerging network properties of 2°VNs

The different, oppositely oriented response properties of frog tonic and phasic 2°VNs (Beraneck et al., 2007) and the differential insertion into inhibitory synaptic circuits (Biesdorf et al., 2008) suggest that intrinsic membrane and emerging network properties are functionally coadapted. Together with the different dynamics of pulse train-evoked compound responses, this supports the idea that each of the two subtypes is optimally adapted for a particular role in vestibular sensory–motor transformation. Accordingly, tonic 2°VNs as low-pass filters are well

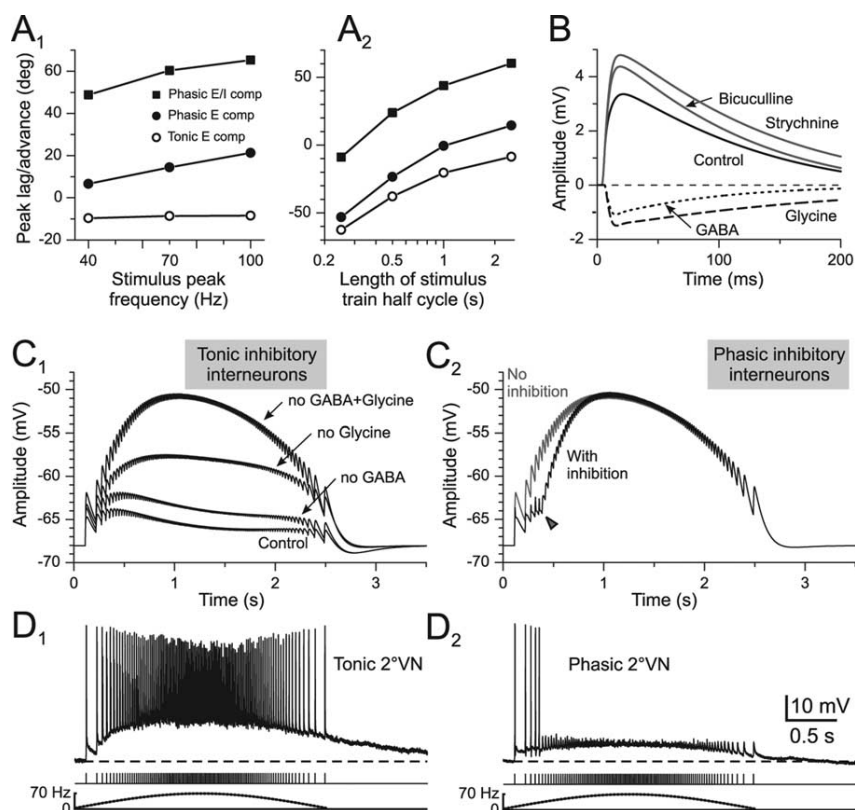


Figure 8. Compound responses generated from intrinsic compartmental models extended by excitatory (*E* compartmental model) or excitatory and inhibitory synaptic conductances (*E/I* compartmental model). **A₁**, **A₂**, Peak lag/advance as a function of stimulus peak frequency (**A₁**) or half-cycle length (**A₂**) of model compound responses reconstructed from tonic (○) and phasic (●) *E* compartmental models; appropriate conductances that mimic the disynaptic inhibition (*E/I* compartmental model) cause the peak advance (■) observed in phasic 2°VNs. **B**, Fitted average responses of the *E/I* compartmental model mimicking labyrinthine nerve-evoked monosynaptic EPSPs before (control) and after application of bicuculline or strychnine in phasic 2°VNs; subtraction from control responses reveals the differential time courses of disynaptic GABAergic (dotted line) and glycinergic (dashed line) IPSPs [fit based on data from the study by Biesdorf et al. (2008)]. **C₁**–**D₂**, Model compound responses of a phasic 2°VN (peak frequency, 70 Hz) based on the *E/I* compartmental model assuming that inhibitory interneurons exhibit either a discharge like a real tonic (**D₁**) or a real phasic 2°VN (**D₂**); model compound responses before (control) and after blocking disynaptic GABAergic, glycinergic, or both components are shown in **C₁**; the arrowhead in **C₂** indicates the increase of the model response amplitude attributable to the termination of the limited discharge (**D₂**) if the inhibitory interneurons were phasic type 2°VNs; recordings in **D₁** and **D₂** are single sweeps; dashed lines indicate the resting membrane potential (−66 mV in **D₁**; −62 mV in **D₂**). The calibration in **D₂** applies to **D₁**; bottom traces in **D₁** and **D₂** show pulse trains and stimulus frequency (dotted lines).

sued for the processing of low-frequency head motion components with a relatively linear transformation of presynaptic afferent activity patterns into postsynaptic responses. In contrast, phasic 2°VNs are most suitable for processing transient, high-frequency components with an input–output function that is rather nonlinear as evidenced by the timing of peak discharge rate (Fig. 5G₂). The large nonlinearity of the latter neuronal subtype is caused by a fast and efficient EPSP summation and a subsequent shunting of the input, particularly during high-frequency presynaptic afferent activity (Fig. 3B). The shunting is mostly attributable to the combined effect of voltage-dependent potassium conductances (Beraneck et al., 2007) and a potent disynaptic inhibition after the monosynaptic EPSP (Biesdorf et al., 2008). Although the experimental data do not allow a distinction between relative contributions of intrinsic and network properties in shaping the synaptic responses, our modeling approach suggests that the feedforward inhibition contributes considerably to the generation of the highly asymmetric response profile in phasic 2°VNs, thus facilitating the effects of the intrinsic cellular characteristics.

The distinct differences of pulse-train evoked synaptic re-

sponses in frog tonic and phasic 2°VNs is suitable to form the cellular basis for a processing of VOR signals in parallel, frequency-tuned channels that mediate linear (tonic) and nonlinear (phasic) components, respectively (Minor et al., 1999). Separate information channels occur at the sensory periphery (Goldberg, 2000) as well as at the extraocular motor level as evidenced by the presence of functional elements with different morphophysiological properties (Büttner-Ennever, 2005; Spencer and Porter, 2005). In frog, this is evidenced by the presence of abducens motoneurons with different response profiles (Dieringer and Precht, 1986). The large advance and nonlinear pattern of the discharge in phasic 2°VNs during sinusoidal pulse-train stimulation of semicircular canal nerves (Fig. 5E, F, G₂) concurs with the particular contribution of eye movements to gaze stabilization in frogs (Dieringer, 1987). During sinusoidal head rotation, compensatory eye motion consists of a rapid, transient eye velocity peak followed by a rather stable eye position. Although the eye velocity shows a transient profile during sinusoidal table rotation, combined eye/head movements generate perfect compensatory gaze movements. The observed different dynamic eye motion components are coherent with an activation of extraocular motoneurons by a combination of signals from phasic and tonic 2°VNs (Fig. 5G₁–G₃) stimulated with the same cycle length of table rotation as *in vivo* (Blanks and Precht, 1976; Dieringer, 1987). Given that both tonic and phasic 2°VNs project directly to extraocular targets (Straka et al., 2004), the discharge patterns of the two vestibular cell types are well suited to generate the necessary premotor commands for the different dynamic eye motion components during gaze stabilization in frog.

Common principles of vertebrate central vestibular information processing

The independent adaptive control of different dynamic aspects of angular VOR suggests that the mediation of linear and nonlinear components in separate sensory–motor channels (Lisberger et al., 1983; Minor et al., 1999; Lasker et al., 2000; Clendaniel et al., 2002; Ramachandran and Lisberger, 2006) is a general feature of vertebrate vestibular information processing. Such a parallel processing requires that different dynamic aspects of head motion-related vestibular signals are not only coded in separate vestibular sensory (Goldberg, 2000) and extraocular motor channels (Büttner-Ennever, 2005; Spencer and Porter, 2005) but are also processed centrally within separate populations of 2°VNs. In frog, tonic and phasic 2°VNs are ideally suited for a separate central processing of linear and nonlinear components. Appropriate homologues for a respective parallel processing in mammals might be tonic and “kinetic” vestibular neurons described in cat (Shimazu and Precht, 1965) or rodent type A and B medial vestibular nucleus (MVN) neurons (Babalian et al., 1997). The latter types exhibit adequate cellular properties necessary for differential signal processing (Straka et al., 2005) mostly based on differences in potassium conductances (Gittis and du Lac, 2007).

In frog, the differential tuning of synaptic response dynamics in 2°VNs depends on intrinsic membrane properties as well as on inhibitory side loops. The connectivity of these circuits is likely not a particularity of frogs but rather a common vertebrate feature. The similarities of vestibular network organization in different vertebrates (Straka and Dieringer, 2004) suggest that the sensory–motor transformation of head motion-related signals in mammals is also controlled by similarly organized side loops (Minor and Goldberg, 1991). Thus, a differential insertion of, for example, rodent type A and B MVN neurons into inhibitory and excitatory circuits is likely and might allow an independent ad-

aptation and modification of particular dynamic aspects. Given a fundamental functional equivalence of central vestibular neurons in different vertebrates (Straka et al., 2005), intrinsic membrane and emerging network properties of mammalian vestibular subgroups might be coadapted as in frogs.

Inhibitory control of vestibular responses

An ipsilateral disynaptic GABAergic and glycinergic inhibition that facilitates nonlinear response components in frog phasic 2°VNs (Biesdorf et al., 2008) is likely also present in a subgroup of mammalian central vestibular neurons. Mouse type B MVN neurons, functional homologues of frog phasic 2°VNs, receive considerably more spontaneous glycinergic and GABAergic inputs from ipsilateral vestibular interneurons than type A MVN neurons (Camp et al., 2006). A feedforward side loop that mediates an inhibition on type B MVN neurons could originate from a subset of type-A-like GABAergic neurons in the parvocellular part of the MVN (Bagnall et al., 2007; Gittis and du Lac, 2007, 2008). This putative organization in mouse matches with our modeling predictions (Fig. 8B, C) and suggests that vestibular inhibitory interneurons are tonic 2°VNs, which are equivalent to mammalian type A MVN neurons (Straka et al., 2005). Thus, a conserved intrinsic vestibular circuitry exists that allows a continuous fine tuning of the response dynamics in a particular type of 2°VNs (Minor and Goldberg, 1991; Straka and Dieringer, 1996).

In all vertebrates, a subpopulation of central vestibular neurons receives a Purkinje cell-mediated GABAergic inhibition (Straka and Dieringer, 2004). Although this inhibition seems to be weak in frog (Magherini et al., 1975; Dieringer and Precht, 1979), a cerebellar lesion increased the gain of the abducens motoneuronal discharge during sinusoidal head rotation by ~50% (Straka and Dieringer, 2004). This complies with the increase of semicircular canal nerve-evoked compound response amplitudes in phasic 2°VNs after a block of the cerebellar circuit (Fig. 6E). The presence of a cerebellar inhibition in some phasic 2°VNs makes these neurons equivalent to mammalian floccular target neurons (FTN) in the MVN (De Zeeuw et al., 1994; Lisberger, 1998). In rodents, these neurons were shown to form a specific subpopulation of type B MVN neurons (Babalian and Vidal, 2000; Sekirnjak et al., 2003). Thus, a differentially organized Purkinje cell-mediated inhibition in equivalent subpopulations of vestibular neurons seems to be another conserved feature of vertebrate vestibular signal processing. The particular role of mammalian FTN in VOR plasticity and the flexibly controlled synaptic signal processing in frog phasic 2°VNs suggests that these neurons are part of a modifiable pathway that enables plastic adaptations of vestibulomotor responses (Lisberger, 1998; Minor et al., 1999; Boyden et al., 2004; Gittis and du Lac, 2006; Ramachandran and Lisberger, 2006, 2008).

References

- Babalian A, Vibert N, Assie G, Serafin M, Mühlethaler M, Vidal PP (1997) Central vestibular networks in the guinea-pig: functional characterization in the isolated whole brain *in vitro*. *Neuroscience* 81:405–426.
- Babalian AL, Vidal PP (2000) Floccular modulation of vestibuloocular pathways and cerebellum-related plasticity: an *in vitro* whole brain study. *J Neurophysiol* 84:2514–2528.
- Bagnall MW, Stevens RJ, du Lac S (2007) Transgenic mouse lines subdivide medial vestibular nucleus neurons into discrete, neurochemically distinct populations. *J Neurosci* 28:2318–2330.
- Baird RA (1994a) Comparative transduction mechanisms of hair cells in the bullfrog utricle. I. Responses to intracellular current. *J Neurophysiol* 71:666–684.
- Baird RA (1994b) Comparative transduction mechanisms of hair cells in the

- bullfrog utricle. II. Sensitivity and response dynamics to hair bundle displacement. *J Neurophysiol* 71:685–705.
- Bekkers JM, Delaney AJ (2001) Modulation of excitability by alpha-dendrotoxin-sensitive potassium channels in neocortical pyramidal neurons. *J Neurosci* 21:6553–6560.
- Beraneck M, Pfanzelt S, Vassias I, Rohregger M, Vibert N, Vidal PP, Moore LE, Straka H (2007) Differential intrinsic response dynamics determine synaptic signal processing in frog vestibular neurons. *J Neurosci* 27:4283–4296.
- Biesdorf S, Straka H (2004) Control of responses in frog second-order semicircular canal neurons by inhibitory and excitatory inputs. *Soc Neurosci Abstr* 30:652.1.
- Biesdorf S, Malinvaud D, Reichenberger I, Pfanzelt S, Straka H (2008) Differential inhibitory control of semicircular canal nerve afferent-evoked inputs in second-order vestibular neurons by glycinergic and GABAergic circuits. *J Neurophysiol* 99:1758–1769.
- Birinyi A, Straka H, Matesz C, Dieringer N (2001) Location of dye-coupled second order and of efferent vestibular neurons labeled from individual semicircular canal or otolith organs in the frog. *Brain Res* 921:44–59.
- Blanks RH, Precht W (1976) Functional characterization of primary vestibular afferents in the frog. *Exp Brain Res* 25:369–390.
- Borg-Graham L (1991) Modelling the non-linear conductances of excitable membranes. In: *Cellular neurobiology: a practical approach* (Chad J, Wheal H, eds). Oxford: IRL at Oxford UP.
- Boyden ES, Katoh A, Raymond JL (2004) Cerebellum-dependent learning: the role of multiple plasticity mechanisms. *Annu Rev Neurosci* 27:581–609.
- Büttner-Ennever JA (2005) The extraocular motor nuclei: organization and functional neuroanatomy. *Prog Brain Res* 151:95–125.
- Camp AJ, Callister RJ, Brichta AM (2006) Inhibitory synaptic transmission differs in mouse type A and B medial vestibular nucleus neurons in vitro. *J Neurophysiol* 95:3208–3218.
- Carnevale NT, Hines ML (2006) *The NEURON book*. Cambridge, UK: Cambridge UP.
- Clendaniel RA, Lasker DM, Minor LB (2002) Differential adaptation of the linear and nonlinear components of the horizontal vestibuloocular reflex in squirrel monkeys. *J Neurophysiol* 88:3534–3540.
- De Zeeuw CI, Wylie DR, DiGiorgi PL, Simpson JI (1994) Projections of individual Purkinje cells of identified zones in the flocculus to the vestibular and cerebellar nuclei in the rabbit. *J Comp Neurol* 349:428–447.
- Dieringer N (1987) The role of compensatory eye and head movements for gaze stabilization in the unrestrained frog. *Brain Res* 404:33–38.
- Dieringer N, Precht W (1977) Modification of synaptic input following unilateral labyrinthectomy. *Nature* 269:431–433.
- Dieringer N, Precht W (1979) Mechanisms of compensation for vestibular deficits in the frog. II. Modification of the inhibitory pathways. *Exp Brain Res* 36:329–357.
- Dieringer N, Precht W (1986) Functional organization of eye velocity and eye position signals in abducens motoneurons of the frog. *J Comp Physiol* 158:179–194.
- du Lac S, Lisberger SG (1995) Cellular processing of temporal information in medial vestibular nucleus neurons. *J Neurosci* 15:8000–8010.
- Eatock RA, Rüscher A, Lysakowski A, Saeki M (1998) Hair cells in mammalian utricles. *Otolaryngol Head Neck Surg* 119:172–181.
- Gittis AH, du Lac S (2006) Intrinsic and synaptic plasticity in the vestibular system. *Curr Opin Neurobiol* 16:385–390.
- Gittis AH, du Lac S (2007) Firing properties of GABAergic versus non-GABAergic vestibular nucleus neurons conferred by a differential balance of potassium currents. *J Neurophysiol* 97:3986–3996.
- Gittis AH, du Lac S (2008) Similar properties of transient, persistent, and resurgent Na currents in GABAergic and non-GABAergic vestibular nucleus neurons. *J Neurophysiol* 99:2060–2065.
- Goldberg JM (2000) Afferent diversity and the organization of central vestibular pathways. *Exp Brain Res* 130:277–297.
- Hille B (2001) *Ion channels of excitable membranes*, Ed 3. Sunderland, MA: Sinauer.
- Hjelmstad GO, Nicoll RA, Malenka RC (1997) Synaptic refractory period provides a measure of probability of release in the hippocampus. *Neuron* 19:1309–1318.
- Hospedales TM, van Rossum MC, Graham BP, Dutia MB (2008) Implications of noise and neural heterogeneity for vestibulo-ocular reflex fidelity. *Neural Comput* 20:756–778.
- Johnston D, Wu SM (1994) *Foundations of cellular neurophysiology* (Bradford Books). Cambridge, MA: MIT.
- Johnston AR, MacLeod NK, Dutia MB (1994) Ionic conductances contributing to spike repolarization and after-potentials in rat medial vestibular nucleus neurons. *J Physiol* 481:61–77.
- Lasker DM, Hullar TE, Minor LB (2000) Horizontal vestibuloocular reflex evoked by high-acceleration rotations in the squirrel monkey. III. Responses after labyrinthectomy. *J Neurophysiol* 83:2482–2496.
- Lisberger SG (1998) Physiologic basis for motor learning in the vestibuloocular reflex. *Otolaryngol Head Neck Surg* 119:43–48.
- Lisberger SG, Miles FA, Optican LM (1983) Frequency-selective adaptation: evidence for channels in the vestibulo-ocular reflex? *J Neurosci* 3:1234–1244.
- Magherini PC, Giretti ML, Precht W (1975) Cerebellar control of vestibular neurons of the frog. *Pflügers Arch* 356:99–109.
- Minor LB, Goldberg JM (1991) Vestibular nerve inputs to the vestibuloocular reflex: a functional ablation study in the squirrel monkey. *J Neurosci* 11:1636–1648.
- Minor LB, Lasker DM, Backous DD, Hullar TE (1999) Horizontal vestibuloocular reflex evoked by high-acceleration rotations in the squirrel monkey. I. Normal responses. *J Neurophysiol* 82:1254–1270.
- Moore LE, Buchanan JT, Murphey CR (1995) Localization and interaction of N-methyl-D-aspartate and non-N-methyl-D-aspartate receptors of lamprey spinal neurons. *Biophys J* 68:96–103.
- Murphey CR, Moore LE, Buchanan JT (1995) Quantitative analysis of electrotonic structure and membrane properties of NMDA-activated lamprey spinal neurons. *Neural Comp* 7:486–506.
- Peusner KD, Giaume C (1997) Ontogeny of electrophysiological properties and dendritic pattern in second-order chick vestibular neurons. *J Comp Neurol* 384:621–633.
- Pfanzelt S, Rohregger M, Moore LE, Straka H (2004) Differential dynamics of labyrinthine nerve afferent-evoked responses in tonic and phasic frog second-order vestibular neurons. *Soc Neurosci Abstr* 30:652.2.
- Ramachandran R, Lisberger SG (2006) Transformation of vestibular signals into motor commands in the vestibuloocular reflex pathways of monkeys. *J Neurophysiol* 96:1061–1074.
- Ramachandran R, Lisberger SG (2008) Neural substrate of modified and unmodified pathways for learning in monkey vestibulo-ocular reflex. *J Neurophysiol*, in press.
- Saint Mleux B, Moore LE (2000) Active dendritic membrane properties of *Xenopus* larval spinal neurons analyzed with a whole cell soma voltage clamp. *J Neurophysiol* 83:1381–1393.
- Sekirnjak C, Vissel B, Bollinger J, Faulstich M, du Lac S (2003) Purkinje cell synapses target physiologically unique brainstem neurons. *J Neurosci* 23:6392–6398.
- Serafin M, de Waele C, Khateb A, Vidal PP, Mühlenthaler M (1991) Medial vestibular nucleus in the guinea-pig. I. Intrinsic membrane properties in brainstem slices. *Exp Brain Res* 84:417–425.
- Shimazu H, Precht W (1965) Tonic and kinetic responses of cat's vestibular neurons to horizontal angular acceleration. *J Neurophysiol* 28:991–1013.
- Spencer RF, Porter JD (2005) Biological organization of the extraocular muscles. *Prog Brain Res* 151:43–80.
- Straka H, Dieringer N (1991) Internuclear neurons in the ocular motor system of frogs. *J Comp Neurol* 312:537–548.
- Straka H, Dieringer N (1993) Electrophysiological and pharmacological characterization of vestibular inputs to identified frog abducens motoneurons and internuclear neurons in vitro. *Eur J Neurosci* 5:251–260.
- Straka H, Dieringer N (1996) Uncrossed disynaptic inhibition of second-order vestibular neurons and its interaction with monosynaptic excitation from vestibular nerve afferent fibers in the frog. *J Neurophysiol* 76:3087–3101.
- Straka H, Dieringer N (2000) Convergence pattern of uncrossed excitatory and inhibitory semicircular canal-specific inputs onto second-order vestibular neurons of frogs. *Exp Brain Res* 135:462–473.
- Straka H, Dieringer N (2004) Basic organization principles of the VOR: lessons from frogs. *Prog Neurobiol* 73:259–309.
- Straka H, Biesdorf S, Dieringer N (1997) Canal-specific excitation and inhibition of frog second order vestibular neurons. *J Neurophysiol* 78:1363–1372.
- Straka H, Holler S, Goto F (2002) Patterns of canal and otolith afferent input convergence in frog second order vestibular neurons. *J Neurophysiol* 88:2287–2301.
- Straka H, Beraneck M, Rohregger M, Moore LE, Vidal PP, Vibert N (2004) Second-order vestibular neurons form separate populations with different membrane and discharge properties. *J Neurophysiol* 92:845–861.
- Straka H, Vibert N, Vidal PP, Moore LE, Dutia MB (2005) Intrinsic membrane properties of vertebrate vestibular neurons: function, development and plasticity. *Prog Neurobiol* 76:349–392.

Modeling of intrinsic and synaptic properties to reveal the cellular and network contribution for vestibular signal processing

Modeling of Intrinsic and Synaptic Properties to Reveal the Cellular and Network Contribution for Vestibular Signal Processing

Christian Rössert,^a Sandra Pfanzelt,^{a,b} Hans Straka,^b
and Stefan Glasauer^a

^a*Department of Neurology, BCCN, Ludwig-Maximilians-Universität München, München, Germany*

^b*Laboratoire de Neurobiologie des Réseaux Sensorimoteurs, CNRS UMR 7060, Université Paris Descartes, Paris, France*

Computational modeling of cellular and network properties of central vestibular neurons is necessary for understanding the mechanisms of sensory–motor transformation for gaze stabilization. As a first step to mathematically describe vestibular signal processing, the available physiological data of the synaptic and intrinsic properties of frog second-order vestibular neurons (2°VN) were used to create a model that combines cellular and network parameters. With this approach it is now possible to reveal the particular contributions of intrinsic membrane versus emerging network properties in shaping labyrinthine afferent-evoked synaptic responses in 2°VN, to simulate perturbations, and to generate hypotheses that are testable in empiric experiments.

Key words: afferent fibers; second-order vestibular neuron; intrinsic membrane properties; synaptic inhibition

Introduction

The processing of head movement–related signals occurs in parallel vestibulomotor networks. Central vestibular neurons in frog form two functional subgroups (tonic and phasic second-order vestibular neurons [2°VN]) based on distinct differences in intrinsic membrane properties.^{1,2} Correlated with these cellular properties, phasic but not tonic 2°VN, receive a disynaptic GABAergic and glycinergic feedforward inhibition³ through tonic vestibular interneurons.⁶ Based on these results a model of the membrane and synaptic properties of 2°VN has been created that can be synaptically activated by a presynaptic discharge that mimics the known firing

pattern of labyrinthine nerve afferents during a horizontal head rotation with constant acceleration.⁴

Methods

Modeling of synaptic processing in tonic and phasic 2°VN was performed by extending previously described intrinsic neuronal models⁵ with an integrate-and-fire threshold and conductance-based synapses. Parameter estimation was based on frequency-domain responses of typical phasic and tonic 2°VN,² and was done by means of a compartmental admittance formulation⁵ in Matlab (MathWorks, Natick, Massachusetts, USA). Real-time compartmental models were simulated with the NEURON software package. Dual-exponential conductance-based synapses were added to the intrinsic single-cell compartmental models. Synaptic excitation in tonic

Address for correspondence: Christian Rössert, Klinikum der Universität München, Zentrum für Sensomotorik, Marchioninistr. 23, 81377 München, Germany. Roessert@lrz.uni-muenchen.de

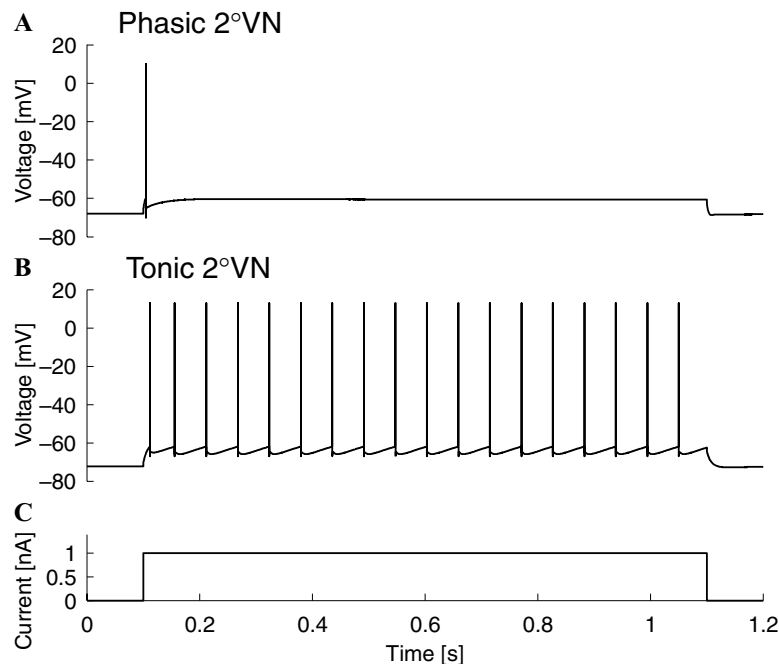


Figure 1. Discharge of (A) phasic and (B) tonic second-order vestibular neurons (2° VN) models evoked by (C) a constant depolarizing current pulse.

and phasic 2° VN was triggered by discharge sequences of labyrinthine nerve afferents; an inhibition in phasic 2° VN was activated by interneurons that exhibit a discharge pattern typical for tonic 2° VN. All synaptic time constants, conductances, and delays were obtained by fitting published experimental data.³ Based on mean rise-time constants (3 ms) of horizontal-canal nerve afferent discharge during constant angular head acceleration,⁴ a series of discharge sequences (duration 5 s; peak frequencies up to 150 Hz) has been constructed and used to activate the model.

Results and Discussion

For the tonic 2° VN intrinsic model, a non-inactivating Na^+ -conductance was necessary, whereas the phasic 2° VN model required an inactivating K^+ -conductance (I_D) and a delayed rectifier.² After adding integrate-and-fire thresholds to the compartmental models, the discharge evoked by the constant depolarizing current pulses into the soma (Fig. 1) matches

well with real data.¹ Based on the intrinsic models, the dynamics of synaptic signal processing was revealed by an extension with a synaptic excitation that was activated by a spike activity pattern (Fig. 2A) obtained from afferent fiber discharge during head rotation⁴ (see Methods). Under these conditions, tonic 2° VN show a spike discharge pattern (Fig. 2B) that is amplified but otherwise similar to the presynaptic afferent activity (Fig. 2A). In contrast, phasic 2° VN fire a few spikes only at stimulus onset and only if the afferent input peak frequency F_{max} is >50 Hz (Fig. 2C). Thus, these latter 2° VN serve as event detectors for head motion, if the acceleration exceeds a minimum value, compatible with conclusions drawn from in vitro experiments.² The respective contribution of intrinsic K^+ -conductances and the feedforward inhibition for generating the particular behavior in phasic 2° VN was tested by a 50% reduction of either the inhibitory inputs (Fig. 2D) or the intrinsic I_D conductance (Fig. 2E). As a result, both properties differentially contribute to the firing of phasic 2° VN

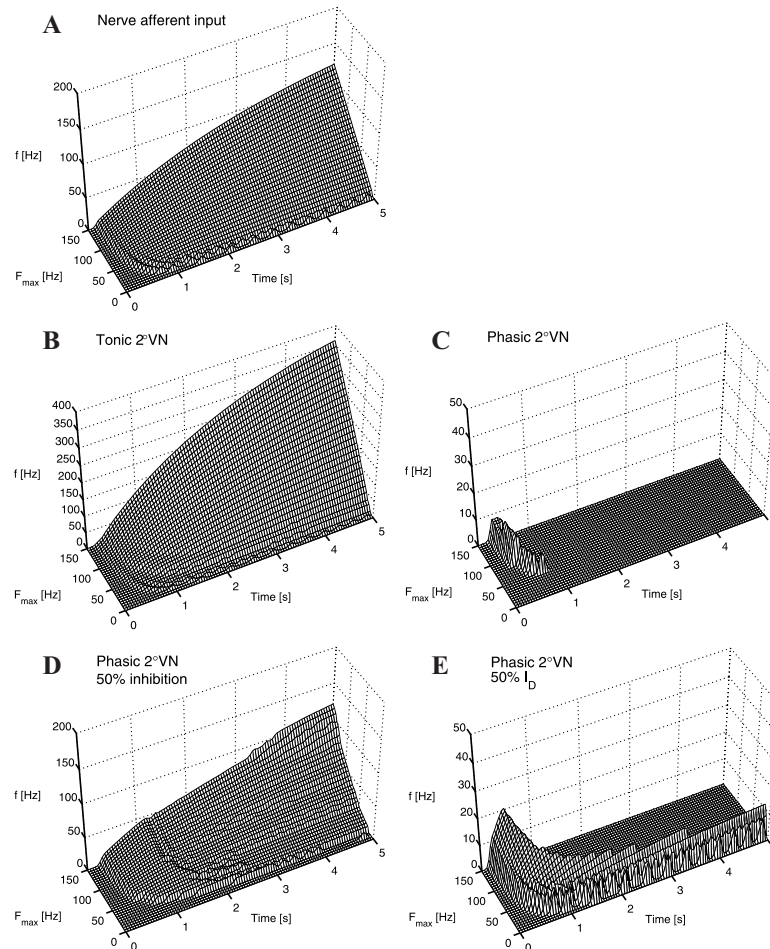


Figure 2. Firing rate $f(t)$ (computed with Gaussian window function, $\sigma = 50$ ms) of vestibular nerve afferent input as well as of tonic and phasic second-order vestibular neurons (2° VN) model discharge behavior during synaptic activation with different input peak frequencies F_{\max} . **(A)** The discharge of afferent fibers during head rotation⁴ was used as a presynaptic input pattern for 2° VN. **(B, C)** Control discharge of tonic (B) and phasic 2° VN (C). **(D)** Discharge of phasic 2° VN with a reduced vestibular interneuronal inhibition or **(E)** a reduced I_D conductance.

(Fig. 2B). With reduced inhibition, the firing becomes continuous throughout the stimulus (Fig. 2D), but at a much lower level than in tonic 2° VN. In contrast, a reduced I_D conductance (Fig. 2E) conserves the event detection for head motion at higher accelerations; at low presynaptic afferent discharge rates the inhibition through tonic interneurons is not strong enough to drive the membrane potential below spike threshold, thus causing these neurons to fire continuously. These results show that both, intrinsic membrane properties as well as

feedforward inhibition contribute to the highly dynamic signal processing of phasic 2° VN, although differentially. Nevertheless, future studies will have to take into account the non-linear K^+-Na^+ interaction on spike generation using a full spiking Hodgkin–Huxley-type model.

Acknowledgments

This work was supported by the CNRS, CNES, and BCCN. One of the authors (S.P.)

received funding from a Marie-Curie Training Sites contract HPMT-CT-2000-00008 (France), the DAAD D/05/40377 (Germany), and the DFG GRK 1091 (Germany); another of the authors (C.R.) received a Ph.D. grant from the Bayerische Forschungsstiftung.

Conflicts of Interest

The authors declare no conflicts of interest.

References

1. Straka, H., M. Beraneck, M. Rohregger, *et al.* 2004. Second-order vestibular neurons form separate populations with different membrane and discharge properties. *J. Neurophysiol.* **92**: 845–861.
2. Beraneck, M., S. Pfanzelt, I. Vassias, *et al.* 2007. Differential intrinsic response dynamics determine synaptic signal processing in frog vestibular neurons. *J. Neurosci.* **27**: 4283–4296.
3. Biesdorf, S., D. Malinvaud, I. Reichenberger, *et al.* 2008. Differential inhibitory control of semicircular canal nerve afferent-evoked inputs in second-order vestibular neurons by glycinergic and GABAergic circuits. *J. Neurophysiol.* **99**: 1758–1769.
4. Precht, W., R. Llinás & M. Clarke. 1971. Physiological responses of frog vestibular fibers to horizontal angular rotation. *Exp. Brain Res.* **13**: 378–407.
5. Moore, L.E., J.T. Buchanan & C.R. Murphey. 1995. Localization and interaction of N-methyl-D-aspartate and non-N-methyl-D-aspartate receptors of lamprey spinal neurons. *Biophys. J.* **68**: 96–103.
6. Pfanzelt, S., C. Rössert, M. Rohregger, *et al.* 2008. Differential dynamic processing of afferent signals in frog tonic and phasic second-order vestibular neurons. *J. Neurosci.* **28**: 10349–10362.

Frequency-domain analysis of intrinsic neuronal properties using high-resistant electrodes



Frequency-domain analysis of intrinsic neuronal properties using high-resistant electrodes

Christian Rössert^{1,2*}, Hans Straka³, Stefan Glasauer^{1,4} and Lee E. Moore³

¹ Institute for Clinical Neurosciences, Ludwig-Maximilians-Universität München, Munich, Germany

² Graduate School of Systemic Neurosciences, Ludwig-Maximilians-Universität München, Munich, Germany

³ Laboratoire de Neurobiologie des Réseaux Sensorimoteurs, Centre National de la Recherche Scientifique, UMR 7060, Université Paris Descartes, Paris, France

⁴ Bernstein Center for Computational Neuroscience Munich, Munich, Germany

Edited by:

Laszlo Acsady, Institute of Experimental Medicine, Hungary

Reviewed by:

Victor Varga, Institute of Experimental Medicine of the Hungarian Academy of Sciences, Hungary

Marco Diana, Ecole Normale Supérieure, France

Robert Renden, Heidelberg University, Germany

*Correspondence:

Christian Rössert, Klinikum der Universität München, Zentrum für Sensomotorik, Marchioninistr. 23, 81377 München, Germany.
e-mail: roessert@lrz.uni-muenchen.de

Intrinsic cellular properties of neurons in culture or slices are usually studied by the whole cell clamp method using low-resistant patch pipettes. These electrodes allow detailed analyses with standard electrophysiological methods such as current- or voltage-clamp. However, in these preparations large parts of the network and dendritic structures may be removed, thus preventing an adequate study of synaptic signal processing. Therefore, intact *in vivo* preparations or isolated *in vitro* whole brains have been used in which intracellular recordings are usually made with sharp, high-resistant electrodes to optimize the impalement of neurons. The general non-linear resistance properties of these electrodes, however, severely limit accurate quantitative studies of membrane dynamics especially needed for precise modelling. Therefore, we have developed a frequency-domain analysis of membrane properties that uses a Piece-wise Non-linear Electrode Compensation (PNEC) method. The technique was tested in second-order vestibular neurons and abducens motoneurons of isolated frog whole brain preparations using sharp potassium chloride- or potassium acetate-filled electrodes. All recordings were performed without online electrode compensation. The properties of each electrode were determined separately after the neuronal recordings and were used in the frequency-domain analysis of the combined measurement of electrode and cell. This allowed detailed analysis of membrane properties in the frequency-domain with high-resistant electrodes and provided quantitative data that can be further used to model channel kinetics. Thus, sharp electrodes can be used for the characterization of intrinsic properties and synaptic inputs of neurons in intact brains.

Keywords: vestibular, abducens, model, intracellular, capacitance, resistance, ion-channel, electrode compensation

INTRODUCTION

The standard method for characterizing properties of single neurons is the intracellular recording with glass micropipettes. Quantitative data on intrinsic and synaptic properties have been mainly obtained from recordings of neurons in culture or in slice preparations with low-resistant patch pipettes. The use of these low-resistant electrodes is required for the voltage clamp control of the membrane potential, which has been used for detailed analyses of ion channel kinetics (Neher and Sakmann, 1976). However, a major drawback of these reduced preparations is that the surrounding neuronal network and the dendritic structures of individual neurons are partially removed, thus making this experimental approach less appropriate for an investigation of synaptic signal processing in complex circuits with feed-forward and feed-back loops, in particular where multiple and longer-range circuits contribute to this processing. Therefore, spatial and temporal aspects of synaptic signal processing in single neurons have been frequently studied *in vivo* or in isolated *in vitro* vertebrate whole brain preparations (e.g. Llinás and Yarom, 1981; Hounsgaard et al., 1988; Babalian et al., 1997). In these preparations, intracellular recordings of neurons are most efficiently made with high-resistant (~50–120 M Ω) sharp glass electrodes to maximize the success rate of impaling neurons.

The disadvantage of these high-resistant sharp electrodes, however, is that it is necessary to compensate the non-linear voltage drop across the electrode during intracellular current injections. The electrode compensation circuits that are implemented in most intracellular amplifiers usually treat the electrode as a simple linear RC circuit (resistor and capacitor). This procedure, however, is generally inadequate since sharp electrodes are often not simple RC elements and show current-dependent non-linear resistance changes (Brette et al., 2008) that are difficult to describe quantitatively and thus impair a reliable use of bridge compensation (BC) or discontinuous current clamp (DCC) compensation (Moore et al., 1993).

The present study describes a novel frequency-domain analysis of single neurons using offline electrode compensation that employs a Piece-wise Non-linear Electrode Compensation (PNEC) procedure to remove the separately measured electrode from the combination of both electrode and cell impedance. With this method it is possible to compensate for arbitrarily complex electrodes in frequency-domain data, which is an improvement to BC and DCC. Moreover it is also an improvement to the novel Active Electrode Compensation (AEC) method (Brette et al., 2008) since the PNEC does not rely on the resistance linearity of the electrode and is independent of the ratio of electrode and membrane time constants,

which do not need to be estimated mathematically from combined measurements of electrode and neuron.

The frequency-domain data provide current-dependent transfer functions, which can be used for the characterization of intrinsic membrane properties or to directly fit compartmental models with a comparable precision and reliability as those obtained from patch-clamp measurements (Booth et al., 1997; Tennigkeit et al., 1998; Roth and Häusser, 2001; Erchova et al., 2004; Taylor and Enoka, 2004; Idoux et al., 2008). Preliminary results have been published in abstract form (Rössert et al., 2008).

MATERIALS AND METHODS

WHOLE BRAIN PREPARATION

In vitro experiments were performed on isolated brains of six adult grass frogs (*Rana temporaria*) and complied with the “Principles of animal care”, publication No. 86–23, revised 1985 by the National Institute of Health. As described in previous studies (Straka and Dieringer, 1993), animals were deeply anesthetized with 0.1% 3-aminobenzoic acid ethyl ester (MS-222), and perfused transcardially with iced Ringer solution (75 mM NaCl; 25 mM NaHCO₃; 2 mM CaCl₂; 2 mM KCl; 0.5 mM MgCl₂; 11 mM glucose; pH 7.4). Thereafter, the skull and bony labyrinth were opened ventrally. After dissecting the three semicircular canals on each side, the brain was removed with all labyrinthine end organs attached to the VIIIth nerve. Subsequently, the brain was submerged in iced Ringer and the dura, the labyrinthine end organs and the choroid plexus covering the IVth ventricle were removed. In all experiments the fore-brain was disconnected. Brains were used as long as 4 days after their isolation and were stored overnight at 6°C in continuously oxygenated Ringer solution (Carbogen: 95% O₂, 5% CO₂) with a pH of 7.4 ± 0.1. The brains were directly fixed with insect pins to the sylgard floor of a chamber (volume 2.4 ml) or glued with cyanoacrylate to a plastic mesh that was fixed to the floor of the recording chamber. The chamber was continuously perfused with oxygenated Ringer solution at a rate of 1.3–2.1 ml/min. The temperature was electronically controlled and maintained at 14 ± 0.1°C.

CLASSIFICATION OF NEURONAL CELL TYPES

External landmarks of the isolated frog whole brain served to identify the target sites for the intracellular recordings in the vestibular (Pfanzelt et al., 2008) and the abducens nuclei (Straka and Dieringer, 1993). Intracellularly recorded second-order vestibular neurons (2°VN) were identified by the activation of monosynaptic EPSPs following electrical stimulation of individual ipsilateral semicircular canal nerves (Straka et al., 1997) with single constant current pulses (duration: 0.2 ms; threshold: ~1–3 μA). These pulses were produced by a stimulus isolation unit (WPI A 360) and applied across suction electrodes whose opening diameters (120–150 μm) were individually adjusted. All 2°VN were classified as phasic or tonic neurons based on their responses to the injection of long, positive current steps (Straka et al., 2004; Beranek et al., 2007; Pfanzelt et al., 2008). Abducens motoneurons (AbMot) were identified by short-latency antidromic action potentials following electrical stimulation of the ipsilateral VIth cranial nerve with suction electrodes (diameter 100–150 μm). These neurons typically received a disynaptic crossed EPSP and an uncrossed IPSP following electrical stimulation of the bilateral horizontal canal

nerve, compatible with previous results obtained after electrical stimulation of the entire VIIIth nerve (Straka and Dieringer, 1993). Only 2°VN and AbMot with resting membrane potentials that were more negative than –55 mV were included in this study.

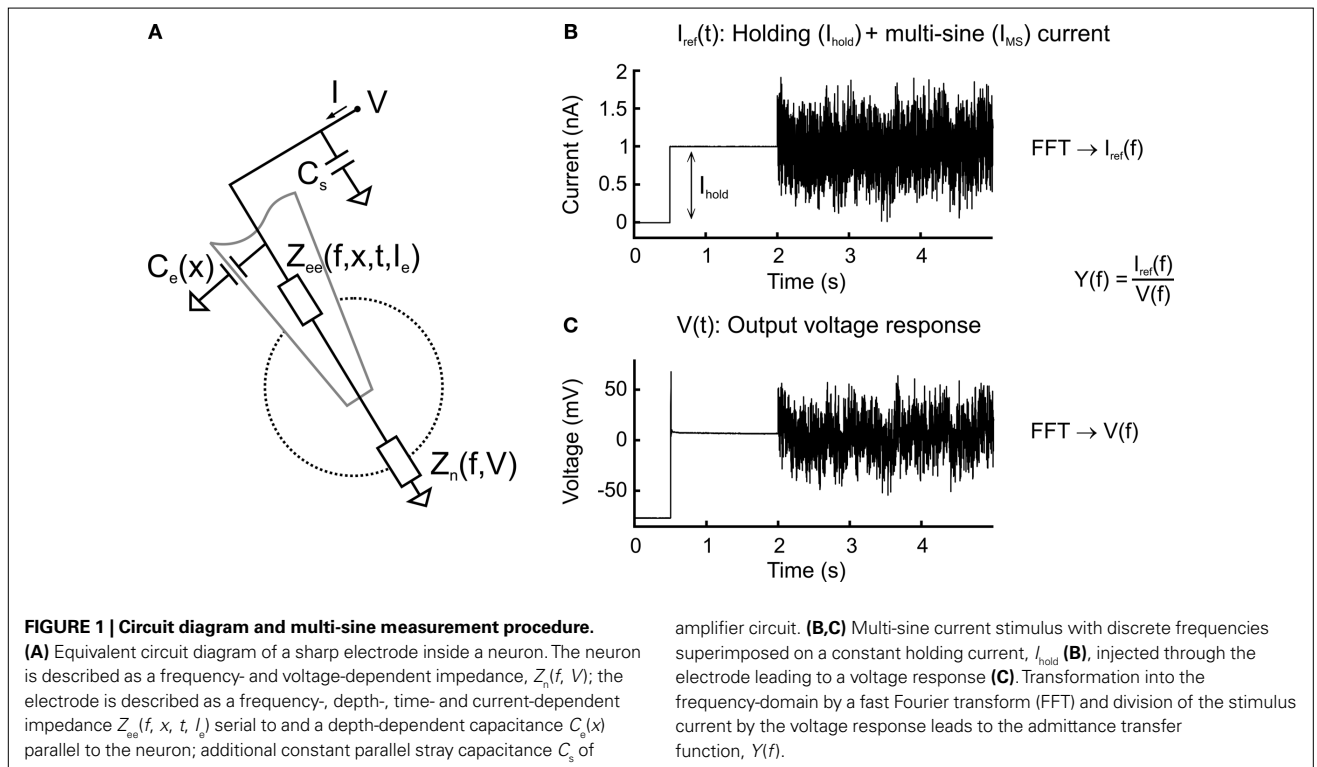
COMPLEX ADMITTANCE MEASUREMENTS WITH SHARP MICROELECTRODES

Sharp high-resistant glass microelectrodes for intracellular recordings were made with a horizontal puller (P-87 Brown/Flaming) using filament-containing borosilicate glass with pre-fire-polished ends (GB150F-8P, Science Products GmbH, Hofheim, Germany). Electrodes were filled with a 3-M solution of KCl or a mixture of 3 M KCl and 2 M KAc (1:10), which gave final resistances of 70–90 MΩ and 80–120 MΩ, respectively. Bath application of the potassium channel blocker 4-aminopyridine (4-AP; 20 μM) confirmed in one experiment the putative contribution of voltage-dependent potassium conductances (Wu et al., 2001; Beranek et al., 2007) to the non-linear response properties of phasic 2°VN.

Voltage recordings and current injections were performed with a single-electrode clamp amplifier (SEC-05L, NPI Electronic GmbH, Tamm, Germany) in the “bridge balance” operation mode with no resistance or capacitance compensation. For A/D and D/A conversion a National Instruments acquisition card (PCI-6052E) was used with a PC (Intel Pentium 4, 1.9 GHz, Windows XP); the signals were sampled at 5 kHz. Recordings were done with a custom Matlab (Mathworks Corp.) program.

Responses of 2°VN and AbMot to a multi-sine current-clamp were measured at different membrane potentials. The multi-sine stimulus I_{MS} was composed of 52–55 discrete frequencies of interest with a uniform stimulus amplitude and randomized phase spectra over a range of either 0.2–988.8 Hz or 0.2–1935.7 Hz (Idoux et al., 2008). The constant magnitude was designed to drive the voltage responses uniformly at all frequencies of interest and the random phase spectrum was chosen to minimize the peak-to-peak dynamic amplitude of the stimulus waveform. The maximal half-amplitude of the multi-sine stimulus (h_{Amp} = half of peak-to-peak amplitude) ranged from 0.4 to 1.2 nA with a duration of 6 or 12 s. In order to measure neurons at membrane potentials of interest (just below spike threshold), the multi-sine stimulus I_{MS} was superimposed on a constant holding current I_{hold} , which preceded the multi-sine stimulus by 1.5 s. This holding current + multi-sine signal was the current clamp command or input current, $I_{ref}(t)$, (Figure 1B) that led to an output voltage response $V(t)$ (Figure 1C). Each measurement consisted of two stimuli, where the second multi-sine stimulus, I_{MS} , was multiplied by –1. A fast Fourier transform (FFT) was done on the difference of the two runs providing $I_{ref}(f)$ and $V(f)$, respectively. The FFT, without windowing, has been computed on all N data points of $I_{ref}(f)$ and $V(f)$, but only the frequencies present in the stimulus were used for the frequency-domain analysis.

The sum of the voltage responses $V(t)$, V_{AveM} , revealed the mean membrane potential and non-linear membrane effects, such as subthreshold responses or action potentials, as well as recurrent synaptic potentials evoked by the current injection during the two runs. Since the polarity of the stimulus alternated, the sum removed all coherent linear responses and thus V_{AveM} is an excellent control for the quality of the measurement. The corresponding admittance



transfer functions were computed as $Y(f) = I_{ref}(f)/V(f)$. Admittance extends the concept of conductance, taking into account dynamic effects by describing not only the relative amplitudes of the voltage and current, but also the relative phases. Admittance is expressed as a complex number $Y(f) = G + jB$ with j being the imaginary unit and G the real part. It is the inverse of the impedance $Z(f) = 1/Y(f)$, which is also a complex number, $Z = R + jC$ with resistance R being the real part.

All transfer functions are shown as complex admittance or impedance Bode plots. In the complex admittance plots, the real part is shown on the x -axis, whereas the imaginary part is plotted on the y -axis. Each data point in this plot thus expresses a different frequency, starting with 0 Hz at the point $(x,0)$. The length of a line that can be drawn between each point and $(0,0)$ corresponds to the magnitude of the admittance at a given frequency, whereas the angle between this line and the horizontal x -axis is the phase shift between the response and the stimulation. Therefore the units of both axes of complex admittance plots are nano-Siemens (nS). All transfer functions after electrode subtraction are shown as the more common impedance Bode plots.

Since no electrode resistance or capacitance compensation was used, the resulting voltage response (**Figure 1C**), and therefore the admittance transfer function, $Y(f)$, refers to both the electrode and the neuron. In the following all admittance transfer functions are written as Y_i with i being e, e + n or e + m indicating that the electrode was measured alone, within a neuron or with a neuronal model, respectively.

During intracellular measurements, the properties of the electrode are best described as a frequency-, depth- (electrode tip with respect to the surface of the Ringer solution in the recording

chamber), time- and current-dependent serial impedance, $Z_{ee}(f, x, t, I_e)$, and a depth-dependent capacitance, $C_e(x)$, parallel to the neuron. In addition to this parallel electrode capacitance, a constant parallel stray capacitance, C_s (**Figure 1A**) is always present, i.e. the capacitance to ground at the input of the buffer operational amplifier (Molecular Devices, 2008). In order to obtain reliable data on frequency responses of single neurons recorded with sharp electrodes, a procedure called Piece-wise Non-linear Electrode Compensation (PNEC) was developed to remove the electrode properties from the total response in the frequency-domain. To test the PNEC method a passive neuronal circuit model composed of a thin film resistance with $R_m = 10 \text{ M}\Omega$ (Tolerance: $\pm 0.02\%$) (Vishay Sfernice, Pennsylvania, USA) parallel to a polystyrene capacitor with $C_m = 1 \text{ nF}$ (Tolerance: $\pm 1\%$) was used. For neuronal or model measurements the root-mean-square (RMS) error was computed separately for impedance magnitude and phase. The degree of electrode nonlinearity (λ) was calculated as the slope of the linear regression between injected current and the steady state electrode resistance (Brette et al., 2008). Matlab (Mathworks Corp.) was used for computations. For time-domain simulations Simulink was used in combination with the SimPowerSystems Blockset to model the electrode and the passive neuron as electrical circuits. For AEC compensation the kernel computation and electrode kernel extraction was done using the latest Python implementation from <http://audition.ens.fr/brette/HRCORTEX/AEC/AECcode.html>. For linear regression calculations the Matlab function “regress” was used. A model for the electrode has been created by fitting two distributed capacitances and resistances (RC’s) and a serial resistance and inductance (R–L) to the measured frequency response of an electrode using the Matlab function “lsqcurvefit”. Graphical

presentations were made with Corel Draw (Corel Corporation Ltd.). Statistica 6.1 was used for the Wilcoxon matched pairs test.

RESULTS

ELECTRODE PROPERTIES

Electrode properties were revealed by using a multi-sine analysis of the electrodes in the recording chamber and/or the tissue to determine the electrode transfer function, Y_e . In contrast to a simple electrode model (constant parallel capacitance and resistance), which approximates a theoretically expected straight line on an admittance plot (red line in **Figure 2A1**), the glass microelectrodes used for the present intracellular recordings show a complex frequency-dependent behavior of the real part (green and blue lines in **Figure 2A1**) but an essentially linear behavior of the imaginary part, similar to a simple RC electrode model (**Figure 2A2**). This behavior depended on the depth (x) of the electrode tip in the tissue and/or bath with respect to the level of the Ringer solution; in particular, the capacitance of the electrode increased with the depth (**Figure 2A2**). Even though the resistance of sharp electrodes, filled with KCl or KAc, could fluctuate randomly within the range of minutes (**Figure 2B1**), the shape of the admittance measurements and its imaginary component (**Figure 2B2**) did not change over time. This spontaneous impedance change was considerably reduced, yet not absent when the electrode tip was inside a neuron. Injections of holding currents I_{hold} through the electrode radically changed the real part of the admittance measurements, but had little effect on its imaginary part (**Figures 2C1,C2**). This behavior can be best seen in the corresponding impedance magnitude plot (**Figure 2C1** inset). Also, note that some sharp electrodes showed a resonance (* in **Figure 2C1** inset) at ~50 Hz that occurred mostly for positive I_{hold} injections. Considering these results and taking into account the additional stray capacitance of the amplifier, the electrode transfer function can be described as

$$Y_e = \frac{1}{Z_{ec}(f, x, t, I_e)} + j2\pi f [C_e(x) + C_s] \quad (1)$$

where Z_{ec} is the complex impedance of the electrode without an assumed passive capacitance. Thus, $\text{real}(Y_e) = \text{real}[1/Z_{ec}(f, x, t, I_e)]$ with an essentially frequency-, depth-, time- and current-dependency and $\text{imaginary}(Y_e) = j2\pi f [C_e(x) + C_s] + \text{imaginary}[1/Z_{ec}(f, x, t, I_e)]$, with the latter being dominated by a depth (x)-dependent electrode capacitance, $C_e(x)$, plus C_s , the amplifier stray capacitance. **Figures 2A2,B2,C2** shows that the imaginary part of Y_e depends linearly on the frequency and is thus almost completely described by $j2\pi f [C_e(x) + C_s]$. Therefore, the parallel capacitance, $C = C_e + C_s$ can be estimated by fitting the function $2\pi f C$ to $\text{imaginary}(Y_e)$ using a linear regression. For all electrodes in the present study, the regression was highly significant (all $R^2 > 0.990$).

PIECE-WISE NON-LINEAR ELECTRODE COMPENSATION (PNEC) PROCEDURE

Because of the particular complex electrode behavior, no electrode compensation (neither resistance nor capacitance compensation) was used, but a procedure called Piece-wise Non-linear Electrode Compensation (PNEC) was developed to subtract the

electrode from the frequency-domain response offline after the measurements. The subtraction procedure involved measuring the electrode alone just after removing it from the neuron, but leaving it in the immediate vicinity (5–8 μm) of the cell and applying the same holding currents, I_{hold} , as used during the intracellular recording. The latter procedure was necessary because of the current-dependent non-linearities of the electrode. As indicated above, changes in the electrode impedance observed either spontaneously or after impalement (Brette et al., 2008) are most likely due to partial blocking or unblocking of the micropipette tip as suggested by the finding that this behavior can be described by translating the real part of Y_e along the real axis, which is equivalent to adding a conductance G_T to the admittance Y_e .

The impedance Z_n of a passive neuron (resistance R_n and capacitance C_n) can be expressed by:

$$Z_n = (R_n^{-1} + j2\pi f C_n)^{-1} = \frac{R_n - j2\pi f C_n R_n^2}{1 + 4\pi^2 f^2 C_n^2 R_n^2} \quad \text{and} \quad \lim_{f \rightarrow \infty} Z_n = 0 \quad (2)$$

$$\text{with } \tau_n = R_n C_n$$

$$\text{real}(Z_n) = \frac{R_n}{1 + 4\pi^2 f^2 \tau_n^2} \quad (3)$$

Thus at high frequencies, the neuron is shunted by its capacitance such that the electrode + neuron admittance measurement Y_{e+n} should overlap with the electrode measurement Y_e . Therefore, in order to compensate for the change in electrode impedance after leaving the neuron, Y_e was translated along the real axis until it superimposed on Y_{e+n} at high frequencies above f_{fit} . For f_{fit} , the frequency was chosen where the resistance of the neuron reaches 1% of its baseline resistance. Knowledge of the membrane time constant (τ_n) of a typical recorded neuron, f_{fit} can thus be calculated by:

$$f_{\text{fit}} = \sqrt{\frac{1}{4\pi^2 \tau_n^2} - 1} \quad (4)$$

A $\tau_n = 2$ ms, as measured in e.g. tonic and phasic 2°VN (Straka et al., 2004) gives a f_{fit} of 792 Hz, which was used in our experiments. With a typical neuronal resistance of 10 M Ω and typical electrode resistances of ~100 M Ω the theoretical error calculated for the electrode resistance estimation is thus only ~0.1% in our experiments.

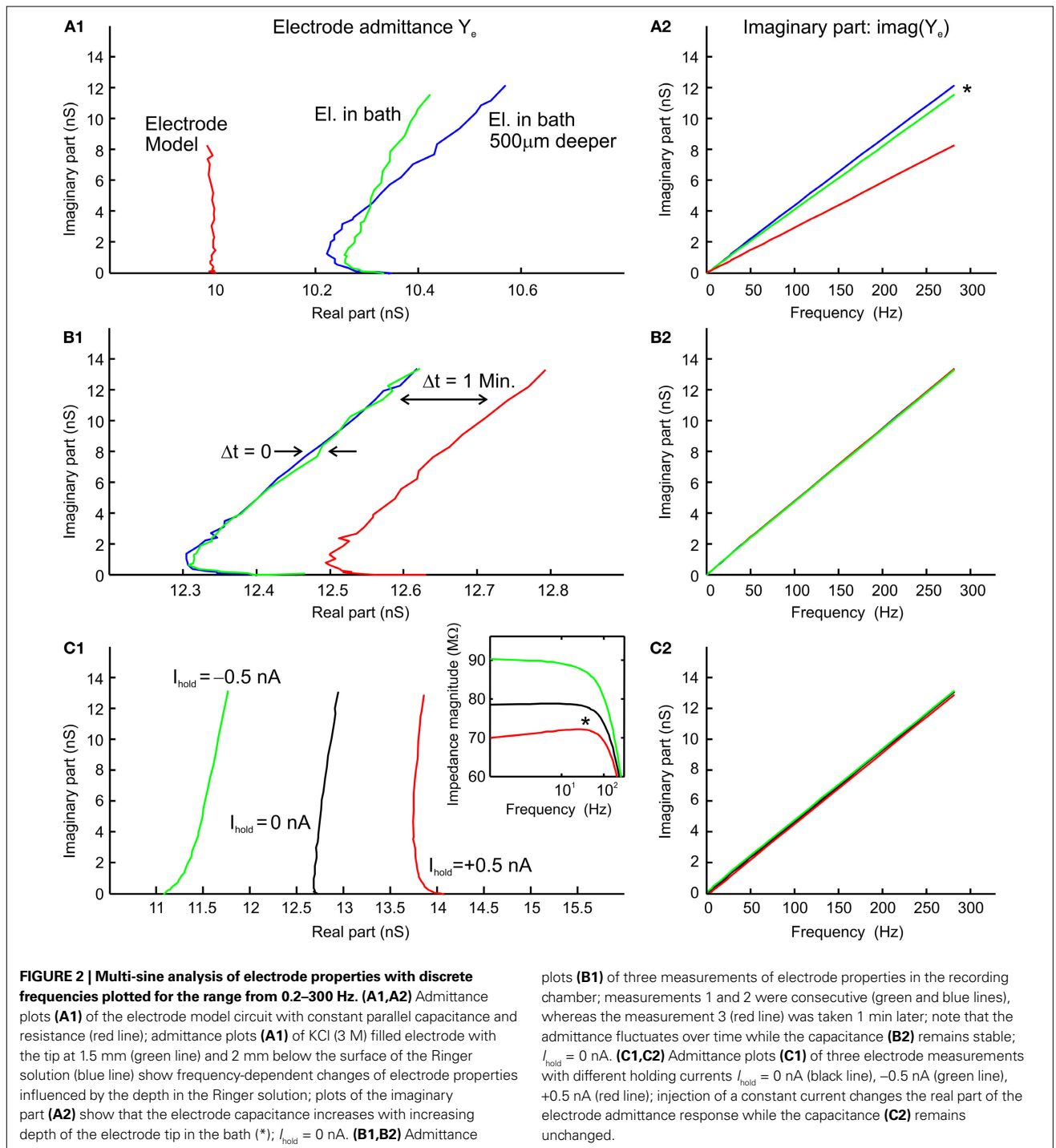
After translating and determining the conductance G_T , the electrode admittance measurements can be used to remove the electrode. Thus, this electrode compensation procedure, referred to as PNEC, is as follows:

- (1) To estimate the conductance G_T the error $[\text{real}(G_T + Y_e) - \text{real}(Y_{e+n})]^2$ has to be minimized in the frequency range between f_{fit} and the maximal frequency (f_{max}) measured. Since G_T is real, the estimation of G_T simplifies to:

$$G_T = \text{mean} [\text{real}(Y_{e+n}) - \text{real}(Y_e)] \quad (5)$$

- (2) Fit $2\pi f C$ to $\text{imaginary}(Y_e)$, using linear regression, in order to remove the parallel electrode capacitance $C_e(x)$, and amplifier stray capacitance C_s :

$$Y_{e+n-c} = Y_{e+n} - j2\pi f C \quad (6)$$



(3) Remove the serial impedance $Z_{\text{ec}}(f, x, t, I_e) = (G_T + Y_e - j2\pi fC)^{-1}$ of the electrode:

$$Y_n = \left[Y_{e+n-c}^{-1} - (G_T + Y_e - j2\pi fC)^{-1} \right]^{-1} \quad (7)$$

The PNEC procedure has been performed with 19 neurons: the 19 electrodes showed a mean resistance of $85.5 \pm 24.5 \text{ M}\Omega$

(mean \pm SD) and a mean capacitance of $8.16 \pm 2.01 \text{ pF}$; for G_T an average of $0.76 \pm 1.2 \text{ nS}$ (mean \pm SD) was estimated, which resulted in an RMS of $0.0375 \pm 0.018 \text{ nS}$ (mean \pm SD; from f_{fit} to f_{max}). The mean degree of nonlinearity (λ) could be evaluated in 12 electrodes and resulted in $-2.56 \pm 3.9 \text{ M}\Omega/\text{nA}$ (mean \pm SD) which is comparable to nonlinearities found previously (Brette et al., 2008).

MODEL TEST OF THE SUBTRACTION PROCEDURE

Measuring a passive neuronal circuit model

The PNEC procedure was tested by measuring a passive neuronal circuit model ($R_m = 10 \text{ M}\Omega$, $C_m = 1 \text{ nF}$), attached to the electrical path-to-ground, through a real electrode in the bath (**Figure 3A**). Although this reproduces the serial resistive connection of an electrode to a real neuron, the electrode capacitance C_e is also serial to the neuron. Since the capacitance C_e is only parallel to the electrode it shunts only the electrode impedance, comparable to the parallel RC of neurons. Accordingly, at high frequencies the two measurements of Y_e and Y_{e+m} do not overlap and the translation conductance G_T cannot be estimated. Thus G_T was chosen for this model test in such a way that the resistance of the model neuron ($10 \text{ M}\Omega$) was correct at the lowest frequency after electrode subtraction. **Figure 3B** shows the admittance plots with $I_{\text{hold}} = 1 \text{ nA}$ of electrode + model neuron (Y_{e+m}) and the measured, but translated electrode ($G_T + Y_e$). **Figures 3C1,C2** illustrates that the impedance magnitude obtained after the PNEC procedure (orange lines) is in good agreement with the analytical values of the neuronal circuit model (green lines) (RMS: $0.22 \text{ M}\Omega$), but shows an error for the phase at high frequencies (RMS: 21.5°) that will be corrected below by taking into account the complete serial connection of the electrode to the test model system. Thus, both the lack of overlapping Y_e and Y_{e+m} at high frequencies and the phase error are due to the serial connection of the electrode capacitance to the model. Since only the amplifier stray capacitance C_s is in parallel to the neuron model, its subtraction must be adapted to the test setup. This involves two individual subtractions of $C_s = 4.4 \text{ pF}$ that was estimated before by measuring a precision resistance, as follows:

$$Y_m = [(Y_{e+m} - j2\pi f C_s)^{-1} - (G_T + Y_e - j2\pi f C_s)^{-1}]^{-1} \quad (8)$$

With this serial-PNEC the phase errors can be eliminated and the obtained impedance magnitude and phase plots (**Figures 3C1,C2**; black lines) match well with the analytical values for the neuronal circuit model (green lines) (RMS: $0.20 \text{ M}\Omega$, 3.7°). This successful subtraction of electrode properties in the model test setup confirms that non-linear electrode properties can be appropriately taken into account during piece-wise linear measurements.

The critical need for correcting microelectrode measurements with measured electrode properties are illustrated by comparing the errors that result from assuming a simple RC electrode (Y_{es} in **Figure 3B**) although it has a resistance identical to the low-frequency (0.2 Hz) impedance of the real electrode and an identical capacitance. **Figure 3C** shows that the serial subtraction, using adapted C_s subtraction as above, of a simple RC electrode (red lines) results in a considerable error and even suggests an incorrect resonance behavior because the real electrode has not been correctly taken into account (RMS: $3.40 \text{ M}\Omega$, 41°). To further quantify the quality of fit, the correlations between the residuals (estimated magnitude and phase minus theoretical values) and the frequency have been analyzed for all three electrode subtractions. The residual error after BC or PNEC still showed a correlation with frequency for both magnitude and phase, but there was no significant correlation using serial-PNEC.

Similar errors using simple RC electrode compensation can also be seen in the data from recorded neurons. Using the PNEC procedure for a frog phasic 2°VN ($I_{\text{hold}} = 0 \text{ nA}$; **Figures 3D1,D2**)

the magnitude and phase plots (black lines) suggest rather passive membrane properties. However, an incorrect subtraction using a simple RC electrode, with a resistance identical to the low-frequency impedance and capacitance identical to the real electrode, yields a considerable resonance (red lines) that however is an artifact due to the incorrect electrode compensation.

Comparison of PNEC, BC and AEC using an electrode model

Using a time-domain simulation in Matlab Simulink the performance of PNEC was compared to Bridge- (BC) and Active Electrode Compensation (AEC, Brette et al., 2008). The frequency-domain behavior of a typical electrode (**Figure 3E1** gray plot) was modeled by using distributed capacitances and resistances (RC's) reflecting the rightward bend in the electrode admittance plots at high frequencies and a serial resistance and inductance (R-L) in parallel to the last distributed RC to account for the resonant behavior at low frequencies. Thus the prominent electrode behaviors could be fitted (Y_e in **Figure 3E1** black line) using two distributed RC's of 14.5 or $55.5 \text{ M}\Omega$ and 4.9 or 2.8 pF , respectively and a R-L with $2.2 \text{ G}\Omega$ and 100 MH (**Figure 3E1** inset). To mimic the electrode resistance shift for the electrode inside the neuron, the resistance of the last RC was reduced from $55.5 \text{ M}\Omega$ to $53.5 \text{ M}\Omega$ when a purely passive RC-type neuron was added which, together with the electrode, produced the admittance response Y_{e+m} as shown exemplarily for a low resistance neuron model (low-R: $R_n = 10 \text{ M}\Omega$, $C_n = 200 \text{ pF}$) in **Figure 3E1** (green line).

For the simulation of BC, capacitance and resistance compensation have been directly implemented by simulating standard compensatory circuits (Molecular Devices, 2008) in Simulink: resistance compensation has been set to the low-frequency resistance of the electrode and capacitance compensation has been used maximally just before ringing occurred. For AEC, only capacitance compensation has been simulated in Simulink and the resistance has been subtracted offline using the provided AEC procedure (Brette et al., 2008). Prior to this simulation, the correct implementation of AEC could be confirmed using an electrode and neuron model as used in the simulations of Brette et al. (2008; not shown).

The simulation has been realized for two types of neurons having a time constant of 2 ms : a low resistance neuron (low-R: $R_n = 10 \text{ M}\Omega$, $C_n = 200 \text{ pF}$, solid lines) and a high resistance neuron (high-R: $R_n = 100 \text{ M}\Omega$, $C_n = 20 \text{ pF}$, dotted lines), mimicking a large and small cell, respectively. Application of the PNEC procedure (with $f_{\text{fit}} = 792 \text{ Hz}$), i.e. shifting $G_T + Y_e$ (**Figure 3E1** dotted line) and subtracting the electrode admittance, results in only small errors (RMS: low-R: $0.2 \text{ M}\Omega$, 3.4° ; high-R: $1.6 \text{ M}\Omega$, 3.5°) for the impedance magnitude and phase plots (black solid or dotted lines) when compared to the expected analytical results of the passive neuron (green solid or dotted lines) (**Figures 3E2,E3**). In contrast, using BC (**Figures 3E2,E3** red solid or dotted lines) magnitude and phase errors (RMS: low-R: $10.5 \text{ M}\Omega$, 20.1° ; high-R: $7.6 \text{ M}\Omega$, 21.0°) occur due to incorrect electrode compensation. For AEC (blue solid or dotted lines) (RMS: low-R: $0.8 \text{ M}\Omega$, 6.7° ; high-R: $5.5 \text{ M}\Omega$, 7.2°), errors already occur at the low-frequency end due to the underestimation of the electrode resistance especially with the high resistance neuron, which results from the low ratio of electrode and membrane time constants. In addition, the inductive component of the electrode further complicates the correct electrode kernel

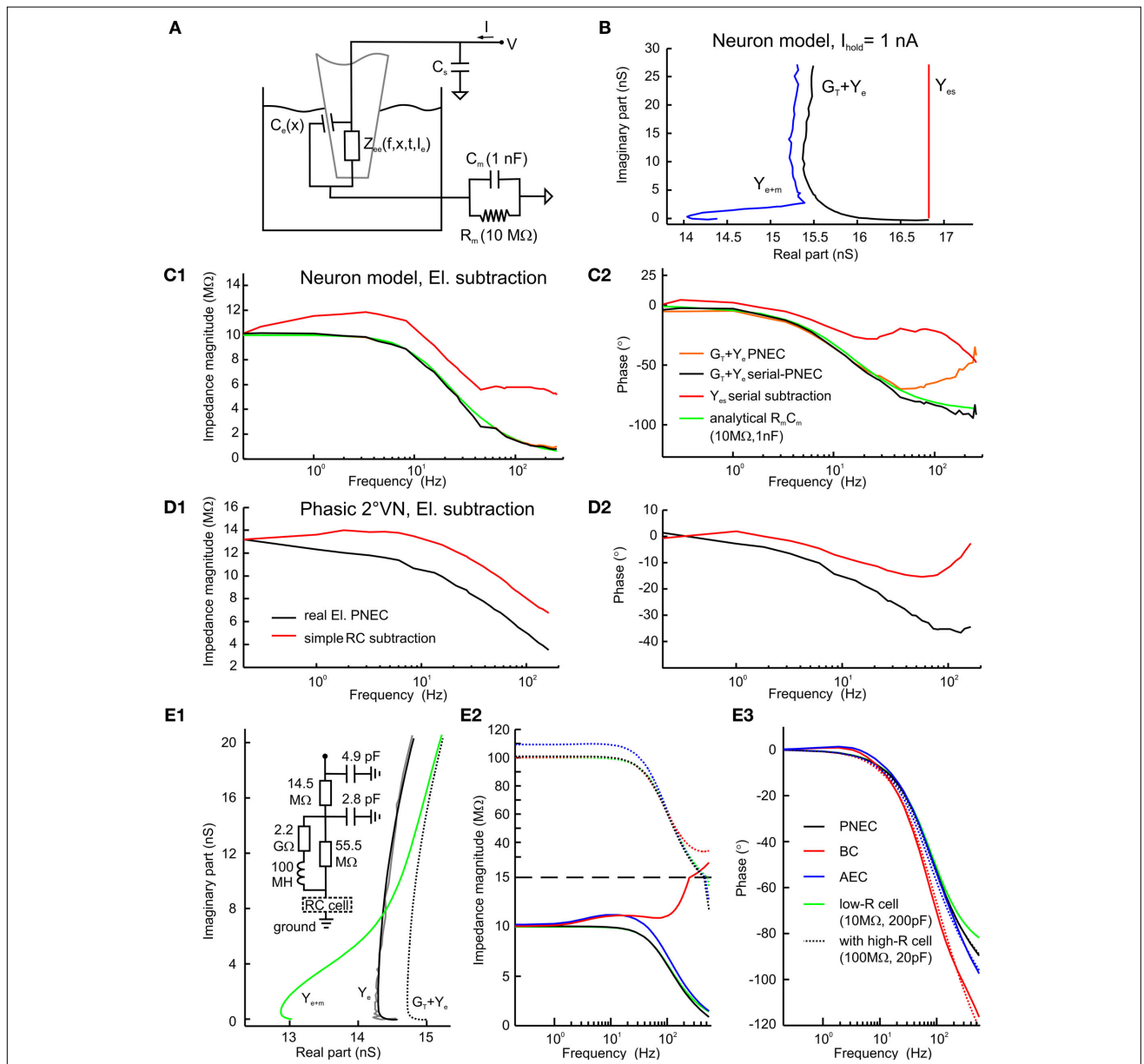


FIGURE 3 | Model test of the Piece-wise Non-linear Electrode Compensation (PNEC) method. (A) Equivalent circuit diagram of the test setup with the electrode in the Ringer-filled recording chamber representing a parallel impedance $Z_{ea}(f, x, t, I_e)$ and a capacitance, $C_e(x)$, serial to a passive neuronal circuit model ($R_m = 10 \text{ M}\Omega$, $C_m = 1 \text{ nF}$) attached to the electrical path-to-ground and a constant amplifier stray capacitance, C_s , parallel to the model. **(B)** Admittance plots of the corrected electrode alone $G_t + Y_e$ (black line) of the electrode with an attached neuronal circuit model Y_{e+m} (blue line) and the analytical response of a simple RC-type electrode model Y_{es} (red line); $I_{\text{hold}} = +1 \text{ nA}$, plotted frequency spectrum 0.2–485 Hz. **(C1,C2)** Bode plots of a passive neuronal circuit model using different electrode compensation methods on the combined measurement Y_{e+m} : (a) electrode $G_t + Y_e$ (orange lines) with PNEC, (b) electrode $G_t + Y_e$ using serial-PNEC (black lines), (c) simple theoretical RC electrode, Y_{es} , using serial subtraction (red lines) and (d) the analytical passive neuronal circuit model (green lines). Note that using the simple RC electrode compensation for the passive neuronal model shows a resonance that is solely an electrode compensation artifact; trace labels in **(C2)** also apply

to **(C1)**. **(D1,D2)** Results from the subtraction of a simple RC-type electrode (red lines) and using PNEC with the actual electrode (black lines) on the intracellular records of a phasic 2°VN ; note that subtraction of a simple RC-type electrode also shows an incorrect resonance for the actual neuron that is caused by the above electrode artifact; trace labels in **(D1)** apply also to **(D2)**. **(E1)** Time-domain simulation of PNEC, AEC and BC; admittance plots of an electrode with distributed capacities and parallel resistance and inductance (inset) Y_e (black line) with parameters adjusted to mimic the behavior as measured in real electrodes (gray line), with an attached passive RC neuronal circuit model ($10 \text{ M}\Omega$, 200 pF) and reduced overall resistance Y_{e+m} (green line) and shifted electrode $G_t + Y_{e+m}$ (dotted line) prior to PNEC subtraction; plotted frequency spectrum 0–556.2 Hz. **(E2,E3)** Results after electrode compensation with a low resistance RC cell (low-R: $10 \text{ M}\Omega$, 200 pF) (solid lines) or a high resistance RC cell (high-R: $100 \text{ M}\Omega$, 20 pF) (dotted lines): simple BC (red) or AEC compensation (blue) causes electrode resonance artifacts in the impedance **(E2)** and phase **(E3)**, while PNEC (black) complies well with the expected results (green); change of y-coordinate scale at $15 \text{ M}\Omega$ (dashed line) in **(E2)**; trace labels in **(E3)** also apply to **(E2)**.

estimation and results in a resonance that is an artifact due to the incorrect electrode compensation, which particularly can be seen in the low-R simulation. The simulations further show that the electrode compensation error in AEC is not solely dependent on the time constant ratio, as stated by Brette et al. (2008) but also increases with the resistance of the cell. This is also the case for PNEC, but here the error can be further reduced by increasing f_{fit} .

This comparison shows that the PNEC method is well suited to compensate for the complicated electrode behavior and yields better results compared to BC and even AEC. However, PNEC is also not perfect, since minor errors occur for the phase at very high frequencies, likely due to an insufficient compensation of distributed electrode capacitances. This suggests that PNEC is reliable at least up to ~300 Hz for the estimation of neuronal frequency-domain transfer functions.

MEASUREMENT RESULTS

Examples of electrode compensation for three different neuronal subtypes recorded with different holding currents (I_{hold}) in an isolated adult frog whole brain were used to illustrate the applicability of PNEC for typical neuronal recordings. **Figure 4A** illustrates the electrode adjustment procedure for an AbMot at $I_{\text{hold}} = +1$ nA, which required a shift in the electrode admittance response, Y_e , due to a difference in the electrode properties when it was removed from the neuron. As described above, the abscissa values were shifted prior to the subtraction in order for the curves to overlap at high frequencies above f_{fit} indicated as $G_T + Y_e$. Electrode corrected magnitude and phase plots for this AbMot at other holding currents illustrate the marked potential dependence of the neuronal impedance including a pronounced resonance (**Figures 4B1,B2**). Bode plot examples for previously described tonic (**Figures 4C1,C2**) and phasic (**Figures 4D1,D2,E1,E2**) 2°VN (Beraneck et al., 2007) indicate that the membrane resonance properties reported for phasic 2°VN (* in **Figures 4D1,E1**) are not an electrode artifact.

Multi-sine analysis allows direct visualization of the dynamic responses of functionally different neuronal phenotypes. For instance, the AbMot, which is plotted in **Figures 4B1,B2** revealed a high degree of resonance during depolarizing currents, most likely caused by an interaction of delayed rectifier potassium and sodium channels (Hutcheon and Yarom, 2000). Frog tonic 2°VN have no membrane resonance behavior but exhibited an increasing impedance with membrane depolarization (**Figures 4C1,C2**). This latter effect is likely caused by non-inactivating calcium or sodium inward currents as suggested previously (Beraneck et al., 2007). In contrast, frog phasic 2°VN showed decreasing impedance and increasing resonance (* in **Figures 4D1,E1**) with membrane depolarization due to the activation of low-threshold voltage-dependent I_D -type potassium channels as reported earlier (Beraneck et al., 2007). Furthermore, since I_D -type potassium channels are specifically blocked by low concentrations of 4-AP (Wu et al., 2001), bath application of 20 μM 4-AP during multi-sine measurements of a phasic 2°VN (dotted lines in **Figures 4D1,D2**) leads to an increase in impedance magnitude for $I_{\text{hold}} = 0$ and $I_{\text{hold}} = 0.5$ nA.

To demonstrate the errors induced by insufficient bridge compensation (BC), another phasic 2°VN (**Figures 4E1,E2**) has been additionally measured during standard BC from the amplifier (dotted lines). While both compensation types match fairly well at the

lowest frequencies for $I_{\text{hold}} = 0$ and -0.5 nA, the measurements at depolarized membrane potentials show an overcompensation due to electrode rectification. Furthermore incorrect compensation of the distributed electrode RCs in BC leads to bends in the magnitude and large jumps in the phase at higher frequencies (~200 Hz).

To compare the PNEC method with standard bridge compensation (BC), both techniques have been applied in a total of 11 neurons at $I_{\text{hold}} = 0$ nA. Since the measurements were made at resting membrane potential, these neurons presumably behave like passive RC circuits with an impedance of $Y_n = G_n + j2\pi fC_n$. Thus C_n can be estimated by fitting $j2\pi fC_n$ to $\text{imaginary}(Y)$ using a linear regression and $G_n = \text{mean}[\text{real}(Y)]$, where Y is the measured neuronal admittance after either PNEC or BC compensation. The root-mean-square error of this fit is calculated as $\text{RMS} = \sqrt{\text{mean}(|Y_n - Y|^2)}$. This test resulted in a better RMS for PNEC, median of RMS: 0.0458 μS , compared to BC, median of RMS: 0.1818 μS (difference highly significant with $p = 0.0076$, Wilcoxon matched pairs test).

TEST OF PIECE-WISE LINEARITY

Control experiments were performed to evaluate the validity of the assumption of piece-wise linearity for PNEC. Measurements of the electrode alone with different multi-sine half-amplitudes ($h_{\text{Amp}} = \text{half of peak-to-peak amplitude of multi-sine stimulus}$; $h_{\text{Amp}} = 1$ nA and $h_{\text{Amp}} = 0.5$ nA) showed that, apart from the time-dependent translational shift of the electrode, the frequency response itself (e.g. $I_{\text{hold}} = +0.5$ nA in **Figure 5A**) does not change with increasing amplitude. Nevertheless, as shown before, frequency responses are significantly affected by the holding I_{hold} current level (compare with Brette et al., 2008). A further indication of the linearity over the range of multi-sine amplitudes is the successful test subtraction procedure (**Figures 3A–C2**). Thus, this is a piece-wise linear analysis of two non-linear elements, the neuron and the electrode, both of which show marked non-linearities at different holding current levels. The non-linear effects of the neuron itself are due to its voltage-dependent ion channels. Measuring AbMot with an $I_{\text{hold}} = 0$ nA and multi-sine currents with three different half-amplitudes of $h_{\text{Amp}} = 0.4$ nA, 0.6 nA and 0.8 nA showed that, apart from some fluctuations in the phase using the largest multi-sine current ($h_{\text{Amp}} = 0.8$ nA), all measurements yield identical results (**Figures 5B1,B2**). The source of these phase fluctuations using $h_{\text{Amp}} = 0.8$ nA could be pinpointed by the observation of V_{AveM} which indicated that the multi-sine current triggered a few spikes (not shown). This result illustrates an important restriction required for most linearization methods, namely that the multi-sine amplitude should be chosen such that it is small enough not to trigger action potentials, but large enough to have a reasonable signal-to-noise ratio.

OUTLOOK: COMPENSATION IN TIME-DOMAIN MEASUREMENTS

Since we are considering piece-wise linear systems, the frequency-domain data can be translated into the time-domain, and therefore it is also possible to use the present PNEC framework to dissociate electrode from neuronal responses for arbitrary stimuli, as long as the current amplitude of the latter remain in the linear range. In the following, a method is presented that allows the determination of the electrode kernel for electrode compensation in the time-domain using the described PNEC framework. For this purpose,

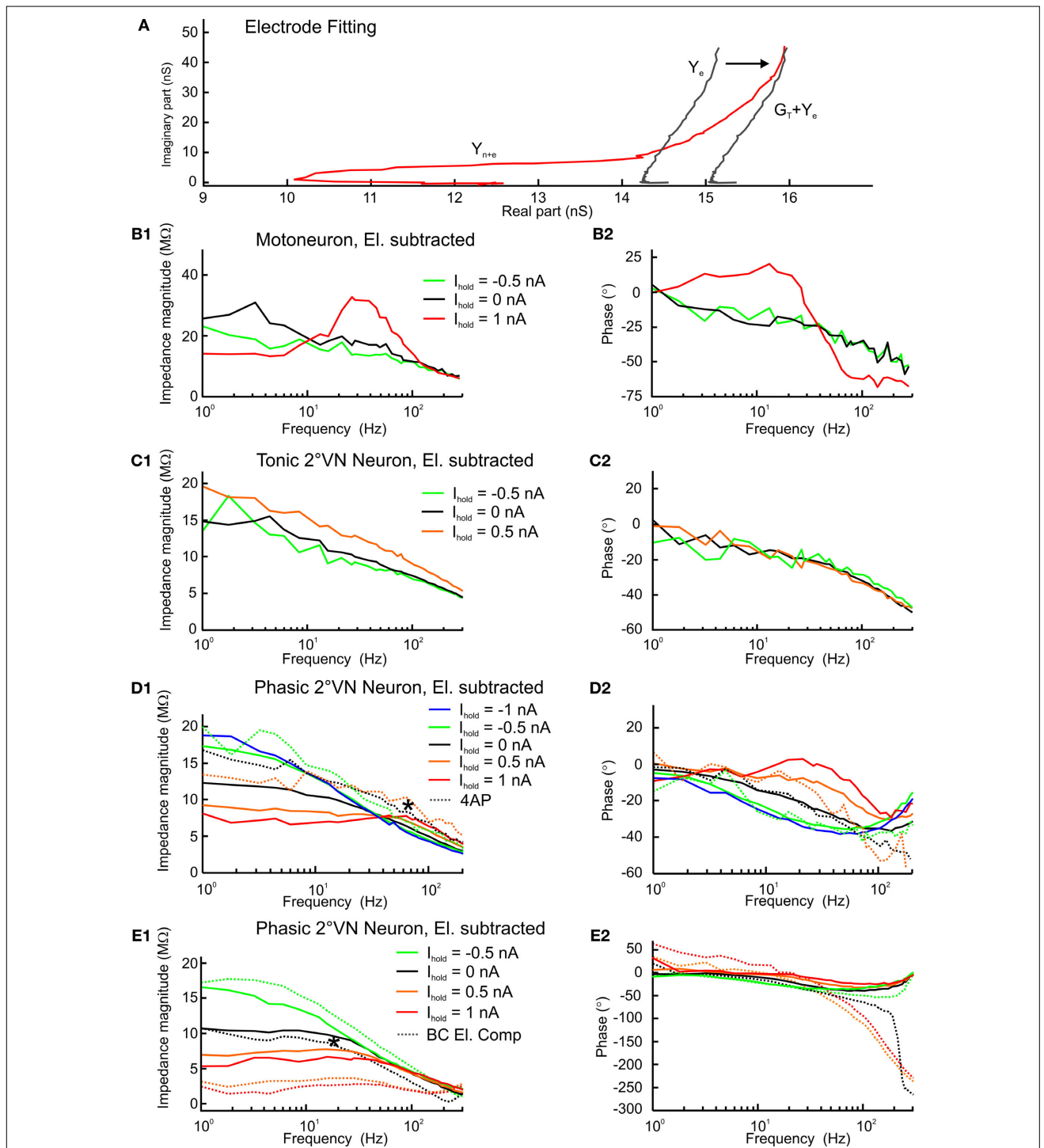
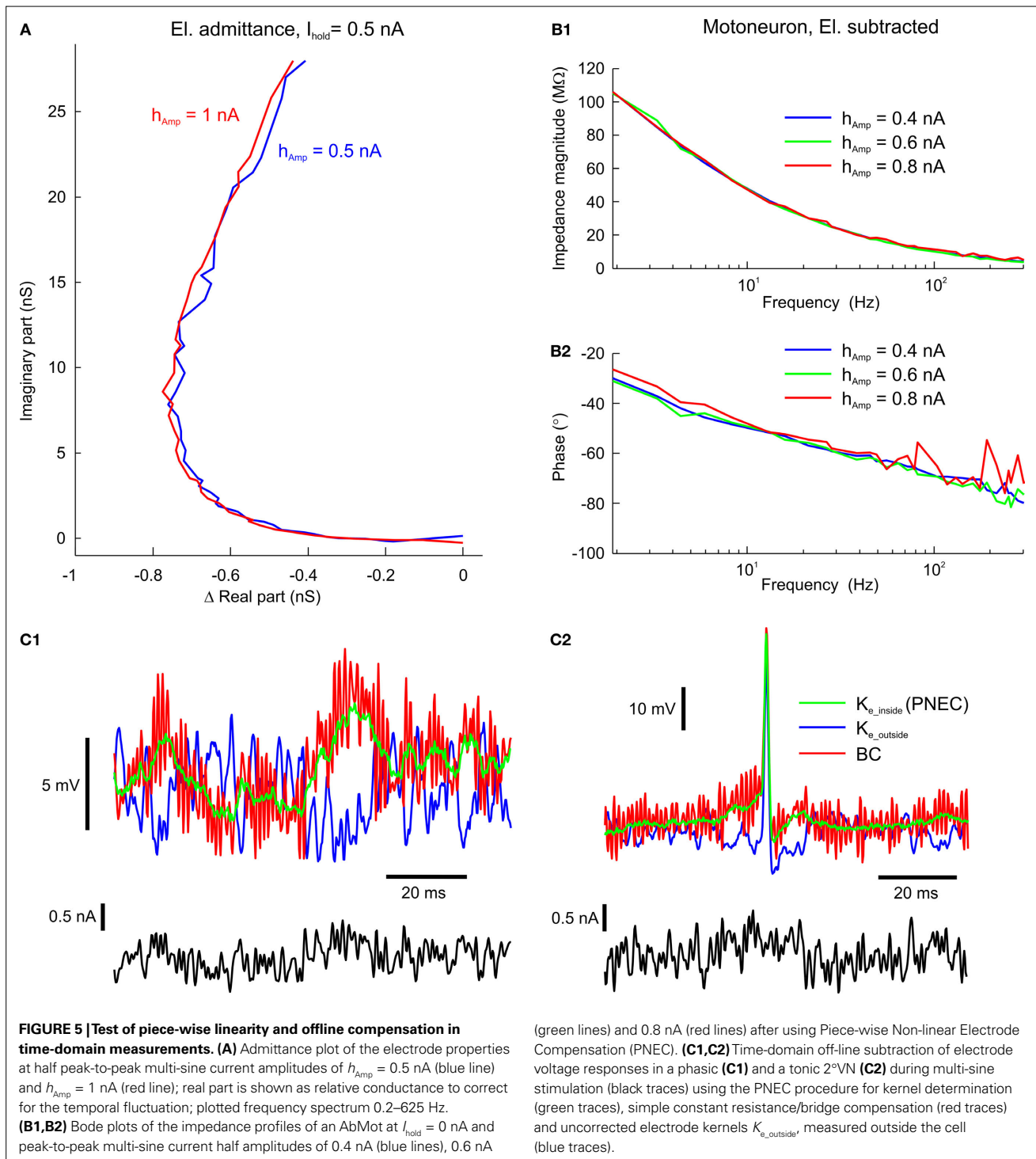


FIGURE 4 | Electrode fitting and response dynamics of second-order vestibular neurons (2°VN) and abducens motoneuron (AbMot) using Piece-wise Non-linear Electrode Compensation (PNEC). (A) Electrode fitting procedure of the responses in an AbMot at $I_{hold} = +1$ nA; the electrode admittance Y_e (solid line) changed after the electrode was removed from the neuron and was shifted ($G_T + Y_e$) in order to overlap at high frequencies with the properties of the electrode + neuron admittance Y_{n+e} ; plotted frequency spectrum 0.2–980 Hz. (B1,B2–D1,D2) Impedance profiles and corresponding

phase relations of the responses at several holding currents (I_{hold}) of an AbMot (B1,B2), a tonic (C1,C2) and two different phasic 2°VN (D1,D2,E1,E2) after PNEC; responses of the phasic 2°VN shown in (D1,D2) were measured before and after bath application of 4-aminopyridine (4AP; 20 μM) [dotted lines in (D1,D2)] with PNEC; responses of the phasic 2°VN shown in (E1,E2) were measured after PNEC as well as during standard bridge compensation (BC) of the amplifier [dotted lines in (E1,E2)]; legends in (B1–E1) also apply to (B2–E2).



multi-sine measurements of the electrode alone, outside the cell, were used to calculate the electrode kernel $K_{e_outside}$ via cross-correlation between input current and output voltage (similar to Brette et al., 2008). These electrode kernels however differ from the real electrode kernel inside the cell and were thus corrected using the conductance G_p estimated via the second measurement inside

the cell, as described before. For this correction, the kernel $K_{e_outside}$ was transformed into the frequency domain via FFT, shifted by G_p , which was estimated using the first step of PNEC, and transformed back into the time-domain using an inverse FFT:

$$K_{e_inside} = \text{IFFT}\{[\text{FFT}(K_{e_outside})^{-1} + G_p]^{-1}\} \quad (9)$$

This corrected electrode kernel K_{e_inside} can be further used to compute the electrode voltage by convolving it with the injected current I_e :

$$V_e = (K_{e_inside} * I_e) \quad (10)$$

However, since no electrode capacitance compensation was used in our experiments, the measured electrode + neuronal voltage V_{e+n} and the computed electrode voltage V_e were low-pass filtered by the electrode, but could be corrected using voltage deconvolution (Richardson and Silberberg, 2008) with:

$$V' = \tau \frac{dV}{dt} + V \quad (11)$$

Here by $\tau = RC$, with R being the impedance at the lowest frequency and C estimated from imaginary(Y_e) during the PNEC procedure.

After application of this voltage deconvolution to V_{e+n} and V_e , the neuronal voltage response could be computed as $V_n = V_{e+n} - V_e$. The results of this procedure were applied offline to the responses of a phasic (Figure 5C1, green traces) and a tonic 2°VN (Figure 5C2, green traces), measured during multi-sine stimulation (Figures 5C1,C2 black traces) with current amplitudes in the linear range, showed that the high-frequency electrode voltage had been removed leaving a low-frequency neuronal voltage, since the injected current was filtered by the neuronal time constant. Compensation of electrode voltage under noisy current stimulation is a demanding task for each electrode compensation mechanism: using a simple constant resistance R for the estimation of the electrode voltage and thus subtracting $V_e = RI_e$, equivalent to standard bridge compensation, leads to insufficient electrode compensation (Figures 5C1,C2 red traces) since small errors in the estimation of the electrode voltage result in high-frequency electrode artifacts (compare with Brette et al., 2008, supplemental data). In addition, using the uncorrected electrode kernels $K_{e_outside}$ for offline compensation (Figures 5C1,C2 blue traces) causes an incorrect estimation of V_n since the overall electrode resistance is overestimated in this case.

In essence, this indicates that the PNEC procedure can be used for a direct estimation of the electrode kernel and offline subtraction of the electrode voltage in the time-domain. For some applications, such as voltage-, or dynamic-clamp experiments, an offline compensation, however, is not sufficient. Nevertheless it is clear that the PNEC procedure to determine the electrode kernel can also be used in combination with online AEC (Brette et al., 2008), as long as the electrode is measured twice: before entering a neuron and inside a neuron. It should also be noted, that for online AEC using the PNEC electrode kernel estimation it is more convenient to use capacitance compensation from the amplifier, as also suggested for normal AEC (Brette et al., 2008), which supersedes the voltage deconvolution step.

DISCUSSION

The new Piece-wise Non-linear Electrode Compensation (PNEC) method provides a way to take into account the non-linear effects of arbitrarily complex electrode properties in the frequency-domain, without online control or compensatory manipulations during the recording. This not only avoids the uncertainties involved in

separating the effects of the electrode compared to those of the neuron, but also the frequent errors caused by improper online compensation, which is difficult if not almost impossible to correct afterwards.

In contrast to the Active Electrode Compensation (AEC) method described recently (Brette et al., 2008) the electrode properties in our PNEC method are not estimated from an electrode + neuron measurement, but are measured separately for each injected current step and corrected afterwards from the frequency-domain data, thus allowing the compensation of slow non-linearities caused by each current step. This compensation procedure is thus not only independent of electrode- and membrane-time constant ratios but also insensitive to resistance non-linearities of the electrode, which is not the case with AEC. Furthermore, using a simulation, it appears that the AEC electrode kernel estimation procedure is inaccurate especially when the electrodes show an inductive/resonating behavior, which however is not a problem for our PNEC procedure.

Frequency responses of neurons have been determined with low-resistant patch pipettes as well as with high-resistant sharp electrodes, but always using standard electrode compensation techniques. While this is not a problem for low-resistant patch pipettes, caution is advised when using high-resistant sharp electrodes and control experiments with the electrodes should be conducted prior to each experiment (see Moore et al., 1993). A previous work using high-resistant sharp electrodes (Gutfreund et al., 1995) states that their electrode impedance was frequency independent in the range of 0–50 Hz, which suggests the following: first, the maximum frequency was sufficiently low in order not to cause errors due to distributed electrode RCs and second, since slices were used, the electrode tips were not immersed as deeply into the bath or brain tissue compared to whole brain recordings which reduces the low frequency inductive/resonating behavior (compare Figure 2A1, blue and green lines).

It is important to emphasize that the piece-wise linear electrode properties shown here, such as the resonant electrode behavior, should not be understood as a general description of all glass micro-pipettes but should rather be considered as an example showing that PNEC is capable of compensating any arbitrarily complex electrodes in the frequency-domain response.

It should also be noted that the offline PNEC method presented here was specifically developed for a frequency-domain analysis. Nevertheless, we could show that the PNEC framework can be used for determination of the electrode kernel and offline subtraction of the electrode voltage in the time-domain. Furthermore this kernel estimation procedure can be used with online AEC (Brette et al., 2008) as long the electrode is measured before entering a cell. The advantage of the combination of the two methods helps avoiding errors that result from the standard AEC electrode kernel estimation.

PNEC is a piece-wise linear method that requires an amplitude of the injected multi-sine current that does not trigger action potentials. Thus, the holding currents I_{hold} have to be selected to drive the neuron either to a sub-threshold membrane potential or to a membrane potential where spiking does not occur due to sodium channel inactivation. As in other compensation methods, the present technique relies on combining distributed capacities of the electrodes. Based on the simulations, a frequency of ~300 Hz

is the upper limit for reliable neuronal impedance measurements with sharp, high-resistant electrodes using PNEC, which covers the important frequency range for most neuronal transfer functions. PNEC is capable of estimating neuronal transfer functions with high-resistant sharp electrodes and is thus a reasonable tool to correlate intrinsic membrane properties with synaptic signal processing in functionally intact whole brain preparations. The resulting neuronal representation in the frequency-domain can be used to analyze membrane properties and the different contributions of ion channels (Hutcheon and Yarom, 2000). It even is feasible to use these neuronal frequency responses to obtain Hodgkin–Huxley type models (Moore et al., 1995; Murphey et al., 1995; Booth et al.,

1997; Tennigkeit et al., 1998; Saint Mleux and Moore, 2000; Roth and Häusser, 2001; Erchova et al., 2004; Taylor and Enoka, 2004; Idoux et al., 2008). In combination with synaptic activation (e.g. Pfanzelt et al., 2008) it is now possible to estimate the synaptic signal processing properties and transfer functions of individual neurons within an entire network.

ACKNOWLEDGMENTS

The authors acknowledge the help of Tobias Kohl in part of the neuronal recordings. This research was supported by the CNRS, CNES and BMBF (01GQ0440). Christian Rössert received a PhD-grant from the Bayerische Forschungsstiftung.

REFERENCES

- Babalian, A., Vibert, N., Assie, G., Serafin, M., Mühlthaler, M., and Vidal, P. P. (1997). Central vestibular networks in the guinea-pig: functional characterization in the isolated whole brain in vitro. *Neuroscience* 81, 405–426.
- Beraneck, M., Pfanzelt, S., Vassias, I., Rohregger, M., Vibert, N., Vidal, P. P., Moore, L. E., and Straka, H. (2007). Differential intrinsic response dynamics determine synaptic signal processing in frog vestibular neurons. *J. Neurosci.* 27, 4283–4296.
- Booth, V., Rinzel, J., and Kiehn, O. (1997). Compartmental model of vertebrate motoneurons for Ca²⁺-dependent spiking and plateau potentials under pharmacological treatment. *J. Neurophysiol.* 78, 3371–3385.
- Brette, R., Piwkowska, Z., Monier, C., Rudolph-Lilith, M., Fournier, J., Levy, M., Fregnac, Y., Bal, T., and Destexhe, A. (2008). High-resolution intracellular recordings using a real-time computational model of the electrode. *Neuron* 59, 379–391.
- Erchova, I., Kreck, G., Heinemann, U., and Herz, A. V. (2004). Dynamics of rat entorhinal cortex layer II and III cells: characteristics of membrane potential resonance at rest predict oscillation properties near threshold. *J. Physiol.* 560, 89–110.
- Gutfreund, Y., Yarom, Y., and Segev, I. (1995). Subthreshold oscillations and resonant frequency in guinea-pig cortical neurons: physiology and modeling. *J. Physiol.* 483, 621–640.
- Hounsgaard, J., Kiehn, O., and Mintz, I. (1988). Response properties of motoneurons in a slice preparation of the turtle spinal cord. *J. Physiol.* 398, 575–589.
- Hutcheon, B., and Yarom, Y. (2000). Resonance, oscillation and the intrinsic frequency preferences of neurons. *Trends Neurosci.* 23, 216–222.
- Idoux, E., Eugene, D., Chambaz, A., Magnani, C., White, J. A., and Moore, L. E. (2008). Control of neuronal persistent activity by voltage-dependent dendritic properties. *J. Neurophysiol.* 100, 1278–1286.
- Llinás, R., and Yarom, Y. (1981). Electrophysiology of mammalian inferior olivary neurons in vitro. Different types of voltage-dependent ionic conductances. *J. Physiol.* 315, 549–567.
- Molecular Devices (2008). The Axon Guide, A Guide to Electrophysiology & Biophysics Laboratory Techniques (Online). Available at: http://www.moleculardevices.com/pdfs/Axon_Guide.pdf, Version 2500-0102 Rev. C.
- Moore, L. E., Buchanan, J. T., and Murphey, C. R. (1995). Localization and interaction of N-methyl-D-aspartate and non-N-methyl-D-aspartate receptors of lamprey spinal neurons. *Biophys. J.* 68, 96–103.
- Moore, L. E., Hill, R. H., and Grillner, S. (1993). Voltage-clamp frequency domain analysis of NMDA-activated neurons. *J. Exp. Biol.* 175, 59–87.
- Murphey, C. R., Moore, L. E., and Buchanan, J. T. (1995). Quantitative analysis of electrotonic structure and membrane properties of NMDA-activated lamprey spinal neurons. *Neural Comp.* 7, 486–506.
- Neher, E., and Sakmann, B. (1976). Single-channel currents recorded from membrane of denervated frog muscle fibres. *Nature* 260, 799–802.
- Pfanzelt, S., Rössert, C., Rohregger, M., Glasauer, S., Moore, L. E., and Straka, H. (2008). Differential dynamic processing of afferent signals in frog tonic and phasic second-order vestibular neurons. *J. Neurosci.* 28, 10349–10362.
- Richardson, M. J. E., and Silberberg, G. (2008). Measurement and analysis of postsynaptic potentials using a novel voltage-deconvolution method. *J. Neurophysiol.* 99, 1020–1031.
- Rössert, C., Glasauer, S., Moore, L. E., and Straka, H. (2008). White-noise analysis of central vestibular neurons with sharp electrodes in whole brain preparations. *Soc. Neurosci. Abstr.* 34, 100.6.
- Roth, A., and Häusser, M. (2001). Compartmental models of rat cerebellar Purkinje cells based on simultaneous somatic and dendritic patch-clamp recordings. *J. Physiol.* 535, 445–472.
- Saint Mleux, B., and Moore, L. E. (2000). Active dendritic membrane properties of *Xenopus* larval spinal neurons analyzed with a whole cell soma voltage clamp. *J. Neurophysiol.* 83, 1381–1393.
- Straka, H., Beraneck, M., Rohregger, M., Moore, L. E., Vidal, P. P., and Vibert, N. (2004). Second-order vestibular neurons form separate populations with different membrane and discharge properties. *J. Neurophysiol.* 92, 845–861.
- Straka, H., Biesdorf, S., and Dieringer, N. (1997). Canal-specific excitation and inhibition of frog second order vestibular neurons. *J. Neurophysiol.* 78, 1363–1372.
- Straka, H., and Dieringer, N. (1993). Electrophysiological and pharmacological characterization of vestibular inputs to identified frog abducens motoneurons and internuclear neurons in vitro. *Eur. J. Neurosci.* 5, 251–260.
- Taylor, A. M., and Enoka, R. M. (2004). Quantification of the factors that influence discharge correlation in model motor neurons. *J. Neurophysiol.* 91, 796–814.
- Tennigkeit, F., Schwarz, D. W., and Paul, E. (1998). GABA(B) receptor activation changes membrane and filter properties of auditory thalamic neurons. *Hear. Res.* 122, 18–24.
- Wu, N., Hsiao, C. F., and Chandler, S. H. (2001). Membrane resonance and subthreshold membrane oscillations in mesencephalic V neurons: participants in burst generation. *J. Neurosci.* 21, 3729–3739.

Conflict of Interest Statement: The authors declare that the research was conducted in the absence of any commercial or financial relationships that could be construed as a potential conflict of interest.

Received: 03 April 2009; paper pending published: 30 April 2009; accepted: 01 August 2009; published online: 20 August 2009.

Citation: Rössert C, Straka H, Glasauer S and Moore LE (2009) Frequency-domain analysis of intrinsic neuronal properties using high-resistant electrodes. *Front. Neurosci.* 3:64. doi: 10.3389/neuro.17.002.2009

This article was submitted to *Frontiers in Neuroscience Methods*, a specialty of *Frontiers in Neuroscience*. Copyright © 2009 Rössert, Straka, Glasauer and Moore. This is an open-access article subject to an exclusive license agreement between the authors and the *Frontiers Research Foundation*, which permits unrestricted use, distribution, and reproduction in any medium, provided the original authors and source are credited.

**Cellular and network contributions to vestibular signal processing:
impact of ion conductances, synaptic inhibition and noise**

Cellular and network contributions to vestibular signal processing: impact of ion conductances, synaptic inhibition and noise

Running title: Cellular and network contributions to vestibular signal processing

C. Rössert^{1,2}, H. Straka³, L.E. Moore⁴ and S. Glasauer^{1,2,5}

¹ Institute of Clinical Neurosciences, LMU München, Marchioninstr. 23, 81377 Munich, Germany

² Integrated Center for Research and Treatment of Vertigo, LMU München, Marchioninstr. 15, 81377 Munich, Germany

³ Department Biology II, LMU München, Grosshadernerstr. 2, 82152 Planegg, Germany

⁴ Centre d'Etude de la Sensorimotricité, Centre National de la Recherche Scientifique, UMR 8194, Université Descartes, 45, rue des Saints-Pères, 75006 Paris, France

⁵ Bernstein Center for Computational Neuroscience Munich, LMU München, Grosshadernerstr. 2, 82152 Planegg, Germany

Send correspondence to:

Christian Rössert

Klinikum der Universität München

Zentrum für Sensomotorik

Marchioninstr. 23

81377 München, Germany

roessert@lrz.uni-muenchen.de

The manuscript includes: 7 figures, 30 pages

Supplemental material: 1 table

Number of words: Abstract: 248; Introduction: 497; Discussion: 1426

Keywords: afferent fibers, phasic, tonic, VOR, semicircular canal, adaptation

Acknowledgments:

This research was supported by the DFG (GRK 1091) and BMBF (BCCN 01GQ0440, IFB 01EO0901). C.R. received a PhD-grant from the Bayerische Forschungsförderung.

Abstract

Head motion-related sensory signals are transformed by second-order vestibular neurons (2°VN) into appropriate extraocular motor commands for retinal image stabilization during body motion. In frog, these 2°VN form two distinct subpopulations that have either linear (tonic 2°VN) or highly non-linear intrinsic properties (phasic 2°VN), compatible with low-pass and band-pass filter characteristics, respectively. In the present study, available physiological data on cellular properties of 2°VN have been used to construct conductance-based spiking cellular models that were fine-tuned by fitting to spike-frequency data. The obtained results of this approach suggest that the differential response characteristics of the two vestibular subtypes are mainly caused by a single additional potassium channel that is low-threshold and voltage-dependent in phasic and spike-dependent in tonic 2°VN. The insertion of phasic 2°VN into a local feed-forward inhibitory network was used to develop a cellular model with conductance-based synapses that allows simulation of the emerging properties of this network. This approach reveals the relative contributions of intrinsic and synaptic factors on afferent signal processing in phasic 2°VN. Extension of the single cell model to a population model allowed further testing under more natural conditions including asynchronous afferent labyrinthine input and synaptic noise. This latter approach indicated that the feed-forward inhibition from the local inhibitory network acts as a high-pass filter, which reinforces the impact of the intrinsic membrane properties of phasic 2°VN on peak response timing. Moreover, the model suggests that synaptic noise and postsynaptic properties of the target neurons critically influence the dynamics of vestibulo-motor commands.

Introduction

Processing of sensory signals in central networks is determined by intrinsic properties and by the synaptic circuitry in which the neurons are embedded (Grillner, 2003). This is well documented in the acoustic system where inhibitory circuits along with intrinsic membrane properties shape the response dynamics of auditory sensory signals (Grothe, 2003; Mathews et al., 2010). In contrast to the organizational complexity of auditory signal processing, the relatively simpler vestibulo-motor signal transformation along sequentially organized three-neuronal reflex pathways (Straka and Dieringer, 2004) is ideally suited to study how cellular and network properties contribute to the signal processing. The major computational step in

transformation of head motion-related sensory signals into extraocular motor commands is performed by second-order vestibular neurons (2°VN), which subdivide in all vertebrates into more or less distinct functional subpopulations with respect to cellular properties (Straka et al., 2005). The different subtypes form the central elements of frequency-tuned parallel vestibulo-ocular information streams (Straka et al., 2009) that are the functional basis for modifiable/non-modifiable or linear/non-linear vestibulo-motor signaling pathways (Lisberger et al., 1983; Clendaniel et al., 2002; Ramachandran and Lisberger, 2008).

Computational models offer the possibility to better understand how properties of individual neuronal populations interact with emerging properties of the circuits in which these neurons are embedded to produce a particular output. The motor circuitry in the lamprey spinal cord is an excellent example that shows how combined cellular and network models can be used to generate a systems model for various modes of locomotor behavior (Grillner, 2003). Even though a number of computational models explain on a systems level various aspects of vestibular-controlled eye movements (e.g. Anastasio and Robinson, 1989; Minor and Goldberg, 1991; Raphan and Cohen, 2002; Green and Angelaki, 2003; Ramachandran and Lisberger, 2006; Glasauer, 2007), a link with cellular vestibular models (Av-Ron and Vidal, 1999; Quadroni and Knöpfel, 1994) or implementation of distinct cellular properties and morpho-physiological aspects is rare (Cartwright et al., 2003). Cellular models of mammalian type A and type B medial vestibular nucleus neurons, on the other hand, largely focus on the impact of ion conductances on vestibular sensory signal processing (Av-Ron and Vidal, 1999; Quadroni and Knöpfel, 1994) but mostly lack implementation of emerging network properties from synaptic inputs of surrounding circuitry. However, several studies (Goldberg et al., 1987; Camp et al., 2006; Bagnall et al., 2008; Biesdorf et al., 2008) suggest that specific insertion of 2°VN into local circuits is an essential element for differential sensory-motor transformation and formation of parallel signaling pathways.

The solid knowledge of cellular physiology and network connectivity of frog 2°VN (Beraneck et al., 2007; Biesdorf et al., 2008; Pfanzelt et al., 2008), allowed generating conductance-based Hodgkin-Huxley type spiking models that were supplemented by excitatory and inhibitory synaptic inputs to distinguish between contributions of cellular and network properties to signal processing. Extension of these single cell models to a population model, allowed making predictions on intrinsic and synaptic contributions to signal transformation during different stimulus paradigms including asynchronous afferent fiber input and synaptic noise.

Materials and Methods

Electrophysiology

In vitro recordings of central vestibular neurons were performed in isolated brains of 12 adult grass frogs (*Rana temporaria*) and complied with the "Principles of animal care", publication No. 86-23, revised 1985 by the National Institute of Health. The experimental methods for the dissection of the frog whole brain preparation were described earlier in detail (Beraneck et al., 2007; Pfanzelt et al., 2008). Neurons were intracellularly recorded with sharp high-resistant glass microelectrodes (80-100 M Ω) and identified as 2 $^{\circ}$ VN by monosynaptic EPSPs following electrical stimulation of individual ipsilateral semicircular canal nerve branches (Straka et al., 1997). All 2 $^{\circ}$ VN were subdivided into either phasic or tonic neurons based on the responses to the injection of long, positive current steps (Straka et al., 2004). Neuronal filter properties of 2 $^{\circ}$ VN were determined by evaluating subthreshold and spike responses following intracellular injection of sinusoidally modulated currents (length $T = 30$ s) with quadratically increasing frequency (maximum $f_{\max} = 100$ Hz) (ZAP stimuli): $I_{ZAP}(t) = I_0 \sin(2\pi f(t)t/3) + I_{hold}$, with $f(t) = f_{\max} (t/T)^2$ (Beraneck et al., 2007). Intrinsic membrane properties were further analyzed using impedance magnitude functions obtained with Piece-wise Non-linear Electrode Compensation (PNEC) (Rössert et al., 2009). The processing of synaptic signals in 2 $^{\circ}$ VN was studied by applying trains of single current pulses (0.2 ms) to individual ipsilateral canal nerves with intensities that ranged between 1.5x and 4x threshold (T) for the postsynaptic response. The stimulus trains consisted of pulses with interstimulus intervals that were sinusoidally modulated with a peak frequency of 70 Hz (Pfanzelt et al., 2008).

Computational Models

All time-domain simulations were run using the NEURON simulation environment (Carnevale and Hines, 2009). To simulate tonic and phasic neurons, Hodgkin-Huxley type models were constructed with regard to simplicity, fast simulation and effective data fitting. Complexity was only added when needed to reproduce the observed behavior (Av-Ron and Vidal, 1999). The minimal models consisted of a soma and a passive dendrite (Clopath et al.,

2007) having nine compartments ($N = 9$). The model is described by the following equations (“time-domain” models):

$$C_S \frac{dV}{dt} = -G_S (V_0 - E_{leak}) - I_{comp} - I_{Na} - I_K - I_D - I_{KA} + I_e \quad (1)$$

for the soma, and

$$\frac{C_D}{N} \frac{dV}{dt} = -\frac{G_D}{N} (V_i - E_{leak}) - I_{comp}, \text{ with } C_D = \rho C_S \quad (2)$$

for the dendritic compartments ($i=[1,N]$). C_S and C_D are the capacitance of the soma and the whole dendrite respectively, G_S and G_D are the resting membrane conductance of the soma and the whole dendrite respectively, E_{leak} is the reversal potential, ρ is the ratio of the total dendritic area to the area of the soma. I_{Na} and I_K are the sodium and delayed-rectifier potassium conductances responsible for action potential generation, I_D is a low-threshold potassium conductance responsible for the band-pass filtering properties in phasic neurons and I_{KA} is an adaptation current responsible for the spike rate adaptation in tonic neurons. I_e is the current applied via the electrode. The area A of the cylindrical compartments is computed using a specific capacitance of $C_m = 1 \mu\text{F}/\text{cm}^2$ and the length and diameter are set to $L = \text{diam} = \sqrt{A/\pi}$. I_{comp} is the current from neighboring compartments and described by:

$$I_{comp} = G_{core} (V_i - V_{i+1}) + G_{core} (V_i - V_{i-1}) \text{ with } G_{core} = N G_D / L_E^2 \quad (3)$$

The index i is 0 for the soma or 1 to N for the dendritic compartments. L_E is the electrotonic length (Rall, 1969).

The kinetics for the voltage-dependent Na^+ current were modeled with equations given by Frankenhaeuser and Huxley (1964) for the amphibian sodium current, adjusted to a temperature of 14° and using Kirchoff's law for the driving force.

$$I_{Na} = g_{Na} m^2 h (V - E_{Na}); Q_{10} = 3^{(14^\circ - 20^\circ)/10}$$

$$dm/dt = \alpha_m(V)(1-m) - \beta_m(V)m; dh/dt = \alpha_h(V)(1-h) - \beta_h(V)h$$

$$\alpha_m = \frac{Q_{10} 0.36 (V - 22 + 70)}{1 - \exp[(-V + 22 - 70)/3]}; \beta_m = \frac{Q_{10} 0.4 (-V + 13 - 70)}{1 - \exp[(V - 13 + 70)/20]}$$

$$\alpha_h = \frac{Q_{10} 0.1 (-V - 10 - 70)}{1 - \exp[(V + 10 + 70)/6]}; \beta_h = \frac{Q_{10} 4.5}{1 + \exp[-(V - 45 + 70)/10]} \quad (4)$$

To reproduce the typical class 1 excitability (definition by Hodgkin (1948), continuous spike frequency – current curve) as seen in tonic 2°VN (Straka et al., 2004) a delayed-rectifier K⁺ (I_K) current with high activation threshold is necessary (Izhikevich, 2006; Prescott et al., 2008). Another indication for the presence of a high-threshold I_K channel is the absence of a resonance in tonic 2°VN impedance measurements during membrane potential depolarization (Beraneck et al., 2007; Rössert et al., 2009). Assuming an identical delayed-rectifier K⁺ current for tonic and phasic 2°VN the channel was therefore modeled as a generic high-threshold potassium type (Prescott et al., 2008) using the Morris-Lecar formalism (Morris and Lecar, 1981) with b_n = -20 mV and g_n = 10 mV.

$$I_K = g_K n (V - E_K); \quad dn / dt = (n_\infty(V) - n) / \tau_n(V)$$

$$n_\infty(V) = 0.5 \left[1 + \tanh \left(\frac{V - b_n}{g_n} \right) \right]; \quad \tau_n(V) = t_n / \cosh \left(\frac{V - b_n}{2g_n} \right) \quad (5)$$

In phasic 2°VN a 4-aminopyridine (4-AP) sensitive low-threshold Kv1.1 potassium channel is implicated in the particular response dynamics (Beraneck et al., 2007). Since this channel is currently not fully characterized in frog, it was modeled using the formalism for the similar low-threshold Kv1.1 potassium channel in mammalian ventral cochlear nucleus neurons (Rothman and Manis, 2003). The factor t_{fac} was added to the original formula to account for time constant adjustments.

$$I_D = g_{KD} w^4 (V - E_K); \quad dw / dt = (w_\infty(V) - w) / \tau_w(V)$$

$$w_\infty = [1 + \exp(-(V + 48) / 6)]^{-1/4}$$

$$\tau_w = t_{fac} (100 [6 \exp((V + 60) / 6) + 16 \exp(-(V + 60) / 45)]^{-1} + 1.5) \quad (6)$$

Tonic 2°VN exhibit a spike rate adaptation during depolarizing current pulse injections (Straka et al., 2004). While the definite mechanism for this adaptation remains unknown, the second, late after-hyperpolarization (AHP) as generally seen in tonic 2°VN (Straka et al., 2004) is very similar to that of mammalian type B MVN neurons (Johnston et al., 1994; Quadroni and Knöpfel, 1994; Peusner et al., 1998; Av-Ron and Vidal, 1999) and thus strongly

suggests a potassium-mediated adaptation. It was therefore modeled as an abstract spike-dependent potassium conductance (Benda and Herz, 2003) that can be easily fitted to spike frequency data:

$$I_{KA} = g_{KA} a (V - E_K); \tau_a \frac{da}{dt} = \delta(t - t_i) - a \quad (7)$$

$\delta(t-t_i)$ is the Dirac delta-function and t_i is the time of the last spike. Thus, each time a spike occurs, the conductance of the channel is increased by g_{KA} and decays with the time constant τ_a .

Frequency-domain model formulation and fitting

For phasic neurons a phenomenological impedance function of a sub-threshold model was fitted to frequency-domain responses obtained during different amplitudes of constant current injections (I_{hold}) (Rössert et al., 2009). This model is similar to the “time-domain” model, but with only one active conductance I_D , which was assumed to be the dominant active conductance close to the resting potential. The total membrane current is the sum of the capacitive displacement current, the ionic current I_D and the constant electrode holding current I_{hold} :

$$I_0 = C_S \frac{dV}{dt} + G_S (V_0 - E_{leak}) + I_{comp} + I_D + I_{hold} \quad \text{with} \quad I_D = G_{KD} w^4 (V - E_K) \quad (8)$$

for the soma and

$$I_i = \frac{C_D}{N} \frac{dV}{dt} + \frac{G_D}{N} (V_i - E_{leak}) + I_{comp} \quad (9)$$

for a dendritic compartment.

The corresponding admittance function can be described as follows. For a general derivation of frequency-domain model formulations see Pfanzelt et al. (2008). A lower index V means that the formula is evaluated at a certain voltage, like $w_V = w_\infty(V)$.

$$Y_S = j2\pi f C_S + G_S + G_{KD} [w_V^4 + 4w_V^3 \delta w^\circ (V - E_K)]$$

$$\delta w^\circ = \left(\frac{dw_\infty}{dV} \right)_V / (j2\pi f \tau_V + 1)$$

$$\left(\frac{dw_{\infty}}{dV}\right)_V = \frac{(1 + \exp[-(V + 48)/6])^{(-1/4)} \exp[-(V + 48)/6]}{24[1 + \exp(-(V + 48)/6)]} \quad (10)$$

The admittance Y_D of a single passive dendritic compartment is:

$$Y_D = j\omega C_D / N + G_D / N \quad (11)$$

The complete input admittance, Y_0 , of the whole compartment model as seen at the soma can be derived by reducing the network to an equivalent driving point admittance (Murphey et al., 1995). The complete input admittance can be derived by beginning at the distal end of the cable and working towards the soma.

$$Y_N = Y_D; Y_i = Y_D + \frac{Y_{i+1} G_{core}}{Y_{i+1} + G_{core}} \text{ for } 1 \leq i \leq N-1; Y_0 = Y_S + \frac{Y_1 G_{core}}{Y_1 + G_{core}} \quad (12)$$

The specific steady state voltage V for each compartment during different holding currents I_{hold} was computed by means of a find root calculation. Finally the inverse of the admittance, the impedance, was taken and the magnitude of the impedance was fitted to the frequency response data of three representative phasic $2^{\circ}VN$. The fitted parameters were L_E , ρ , C_S (pF), G_S (nS), G_D (nS), g_{KD} (mS/cm²) and t_{fac} . The reversal potentials were set to $E_K = -90$ mV and $E_{leak} = -70$ mV. The fit was realized using the nonlinear least-squares fitting function 'lsqnonlin' in MATLAB (Mathworks Corp.). The resulting mean values (\pm SD) for the phasic frequency-domain models ($n = 3$) were: $L_E = 0.77 \pm 0.2$, $\rho = 4.15 \pm 2.6$, $C_S = 138.2 \pm 53.2$ pF, $G_S = 27.4 \pm 18$ nS, $G_D = 27.6 \pm 33$ nS, $g_{KD} = 5.55 \pm 4.3$ mS/cm² and $t_{fac} = 1.00 \pm 0.1$. The detailed parameters for all phasic frequency-domain models are given in the supplemental Table 1 available online as supplemental material.

Time-domain fitting to experimental data

The time-domain models of tonic and phasic $2^{\circ}VN$ were adjusted to experimental data using the simulated annealing algorithm implementation 'simulannealbnd' in MATLAB (Mathworks Corp.). The error function consisted of two parts. Similar to Pospischil et al. (2008), the first part was based on the firing behavior of the cells (f-I fit) and was the sum over the absolute values of the differences between several interspike frequencies: from onset of DC injection to the first spike (f_0), between the first and second interspike interval (f_1, f_2) and the mean of the firing frequencies after 150 ms of DC injection (f_{∞}) where spike rate adaptation was complete. If no spikes occurred to compute f_1-f_{∞} , the corresponding values were set to 0,

which corresponds to an interspike interval of infinity. The values were taken at 4-13 different DC levels, depending on the cell. The second part was the sum over the absolute values of the differences in the membrane potential at the end of a small amplitude current injection (-0.3 to 0.3 nA) (V_{decay} fit). To prevent fitting of electrode artifacts the first 1 ms after the stimulation was excluded from the fit. This led to an overall error function of:

$$e = \sum_{i=0,1,2,\infty} \sum_{DC} \sqrt{(f_i^{\text{data}} - f_i^{\text{sim}})^2} + \sqrt{(V_{\text{decay}}^{\text{data}} - V_{\text{decay}}^{\text{sim}})^2} \quad (13)$$

The adjusted parameters for tonic neurons were L_E , ρ , C_S (pF), G_S (nS), G_D (nS), g_{Na} (S/cm²), g_K (S/cm²), τ_n (ms), g_{KA} (mS/cm²) and τ_a (ms). The resulting mean values (\pm SD) for the tonic time-domain models ($n = 7$) were: $L_E = 1.0 \pm 0.3$, $\rho = 7.2 \pm 1.4$, $C_S = 92.3 \pm 20$ pF, $G_S = 27.8 \pm 9.0$ nS, $G_D = 6.81 \pm 4.1$ nS, $g_{\text{Na}} = 0.10 \pm 0.02$ S/cm², $g_K = 0.013 \pm 0.003$ S/cm², $\tau_n = 4.6 \pm 1.9$ ms, $g_{\text{KA}} = 0.139 \pm 0.06$ mS/cm² and $\tau_a = 49.3 \pm 9.7$ ms. Due to the limited information content in the spiking data of phasic 2°VN, the fitted parameters in the latter neurons were L_E , ρ , C_S (pF), G_S (nS), G_D (nS), g_{KD} (mS/cm²). For g_{Na} (S/cm²), g_K (S/cm²) and τ_n (ms) the mean values from the tonic fit have been used. For t_{fac} the mean from the frequency domain fit was chosen. The resulting mean values (\pm SD) for the phasic time-domain models ($n = 17$) were: $L_E = 1.0 \pm 0.3$, $\rho = 6.18 \pm 2.8$, $C_S = 38.0 \pm 16.3$ pF, $G_S = 28.5 \pm 13.3$ nS, $G_D = 15.1 \pm 11$ nS, $g_{\text{KD}} = 2.78 \pm 2.2$ mS/cm². The detailed parameters for all tonic and phasic neurons are given in the supplemental Table 1 available online as supplemental material. Unless stated otherwise, the reversal potentials for all models are $E_{\text{Na}} = 55$ mV, $E_{\text{K}} = -90$ mV and $E_{\text{leak}} = -70$ mV.

Model for synaptic activation

To simulate synaptic activation of 2°VN, dual-exponential conductance-based synapses were added to the soma of the compartmental models using the following equation: $I_s = g_s F [\exp(-t/\tau_2) - \exp(-t/\tau_1)] (V_i - E_s)$ with τ_1 as rise and τ_2 as fall time constant (Johnston and Wu, 1994). The index s is E for excitatory or I for inhibitory synapses. The peak conductance for a single synaptic event was defined by g_s ; V_s indicates the reversal potential and V_i the current compartmental membrane potential. The scaling factor F is defined such that the peak of the dual-exponential is 1. For excitatory synapses values were $\tau_1 = 5$ ms, $\tau_2 = 50$ ms and $E_E = 0$

mV (similar to Pfanzelt et al. (2008)). Disynaptic GABAergic and glycinergic feed-forward inhibition (Pfanzelt et al., 2008) was combined into one inhibitory synaptic process with $\tau_1 = 5$ ms, $\tau_2 = 150$ ms and $E_I = -75$ mV. Synapses were implemented by the function "exp2syn" in the NEURON simulation environment. To mimic the monosynaptic excitation following electrical stimulation of vestibular nerve afferent fibers in the periphery a delay of 3.4 ms (Biesdorf et al., 2008), from the stimulus to the onset of the excitation, was used. This delay is composed of stimulus utilization time for activation of vestibular afferents, conduction time from the site of stimulation in the periphery to central targets and synaptic delay between vestibular afferents and 2°VN (Straka et al., 1997). For the inhibition by the local circuit a delay of 1.8 ms for one synapse (Holler and Straka, 2001) was used. Unless stated otherwise $g_E = 10$ μ S and $g_I = 20/N$ nS, where N is the number of inhibitory interneurons. To simulate the synaptic activation by ipsilateral canal nerves, each single current pulse of the sinusoidally modulated stimulus train was assumed to trigger one synaptic event.

Spike rate analysis under sinusoidal stimulation

For single tonic cells or models the instantaneous firing rate (IF) was calculated as the inverse of the interspike interval and assigned to the time of the second spike of the interval to ensure a causal relation between IF and input current (du Lac and Lisberger, 1995). The spike response transfer function for each frequency was calculated as $\Delta IF / \Delta I$ where ΔIF is the amplitude of the instantaneous firing rate IF and ΔI is the amplitude of the stimulation current I_e (Beraneck et al., 2004). The phase shift was calculated as the position of ΔIF with respect to the peak of the sine wave, provided that at least two spikes are triggered by the sine wave.

Population model

For the population model, a total of 200 phasic and 200 tonic cells have been simulated. The parameters have been drawn from a lognormal distribution using the mean and standard deviation values estimated in the time-domain fits (see Table 1 in the supplemental material). Inhibition via local interneurons was realized by adding inhibitory synapses to each phasic 2°VN from 10 randomly selected tonic 2°VN. Instead of using a classical spike rate analysis to evaluate the responses of the tonic and phasic cell populations a more biological relevant analysis was employed: the output of the simulated neuronal population that converges onto a particular target neuron was assumed to be the sum of the synaptic activity that is evoked by

the spikes from the simulated population. All tonic and all phasic 2°VN were thus connected with excitatory synapses (with a normalized synaptic strength of 1) to two hypothetical target neurons, respectively. The postsynaptic conductance was simulated with alpha-functions ($g_s = t / \tau_{syn} \exp(-(t - \tau_{syn}) / \tau_{syn})$) (Dayan and Abbott, 2001) using two different time constants, $\tau_{syn} = 30$ ms or $\tau_{syn} = 5$ ms mimicking temporal evolution of the synaptic conductance. The resulting population response is called computed postsynaptic conductance G_S .

The population model was stimulated in two ways. To simulate sinusoidally modulated pulse-train stimulation each model cell was excited as described above with $g_E = 15$ nS for phasic and $g_E = 5$ nS for tonic neurons. To simulate noisy synaptic afferent input during sinusoidal rotation, a sinusoidal current $I(t) = I_0 + I_{max} \sin(2\pi ft)$ was injected into each cell (Hospedales et al., 2008). Since frog vestibular afferents show a low resting activity *in vivo* (Blanks and Precht, 1976) and many frog central vestibular neurons are silent or have a low resting discharge (Dieringer and Precht, 1977, 1979), continuous synaptic input seems to play a minor role in the frog vestibular system and thus $I_0 = 0$ in the simulations. Furthermore only ipsilateral stimulation was considered, thus all negative values of $I(t)$ were set to zero. To simulate synaptic noise and unsynchronized responses from single afferent fibers a noise current $\varepsilon(t) = N(0, \sigma)$ filtered with $\tau = 2$ ms (Hospedales et al., 2008) was added which resulted in a total excitatory current of $I_s(t) = I(t) + \varepsilon(t)$. For the implementation of the noise current $\varepsilon(t)$ in NEURON see Arsiero et al. (2007). I_{max} was set for each neuron individually to 1.5 times the rheobase threshold, estimated with current steps of 100 ms. Unless stated otherwise, standard deviation σ of the noise current was set to 60 pA (Hospedales et al., 2008). Even though this stimulation used a current-based synaptic model that neglects conductance fluctuations, this model has been proven exceptionally useful to provide insight into basic neuronal signal transmission during noisy input (Arsiero et al., 2007; Richardson and Silberberg, 2008; Hospedales et al., 2008). To calculate the sensitivity of the population for several frequencies f , the population was stimulated with frequencies varying from 0.1 to 100 Hz. After an onset time of at least 1 s, the amplitude ΔG_S was estimated from the mean of 20 sinusoidal cycles.

Results

Differential organization of intrinsic properties of frog second-order vestibular neurons

In frog, 2°VN form two well-separated populations (tonic - phasic neurons) that differ in intrinsic and synaptic response dynamics. Tonic 2°VN exhibit a sustained discharge (Fig. 1A₁) during long positive current steps with a relatively linear current-frequency relation, while phasic 2°VN fire only few spikes immediately after stimulus onset (Fig. 1A₂), consistent with different filter properties of the two neuronal types (Straka et al., 2004). These firing behaviors correspond to class 1 and class 3 excitability, respectively, as defined by Hodgkin (1948). Subthreshold responses (Fig. 1B₁, gray) and spike discharge (Fig. 1B₁, black) in tonic 2°VN exhibit low-pass filter-like properties (Beraneck et al., 2007). In contrast, phasic 2°VN have band-pass filter-like characteristics as evidenced by the presence of a membrane potential-dependent subthreshold response peak between 10-50 Hz that generates a particular frequency window for spike discharge (Fig. 1B₂). Moreover, depolarization causes an increase of the impedance in tonic (Fig. 1C₁) and a decrease in phasic 2°VN (Fig. 1C₂) (Beraneck et al., 2007; Rössert et al., 2009). The different, yet complementary filter properties thus render tonic 2°VN suitable for integration and phasic 2°VN for differentiation of synaptic inputs.

The different intrinsic properties of tonic and phasic 2°VN correlate with different dynamics of synaptic responses activated by vestibular nerve afferents (Pfanzelt et al., 2008). In tonic 2°VN, the overall waveform of the compound EPSP, activated by sinusoidally modulated pulse trains, is approximately aligned with the stimulus frequency modulation (Fig. 1D₁) and spikes are continuously triggered above spike threshold (Fig. 1E₁). In phasic 2°VN, the compound EPSP has a sharp rise and an early, slow decay, thus causing an advanced response peak relative to the envelope of the pulse train (Fig. 1D₂). In addition, spikes are triggered only by the first few pulses of the stimulus train (Fig. 1E₂). Physio-pharmacological analyses (Biesdorf et al., 2008; Pfanzelt et al., 2008) suggest that the dynamic response profile of phasic 2°VN is caused by intrinsic membrane properties as well as the emerging properties of the network in which the neurons are embedded. In particular, activation of local inhibitory feed-forward circuits that are composed of tonic-type vestibular interneurons contribute to the marked asymmetry of the response in phasic 2°VN.

Model of tonic second-order vestibular neurons

In order to establish the quality of the modeling procedure, the fitting results for tonic 2°VN models were compared with the respective intracellular recordings. Figure 2A_{1,2} shows an exemplary fit of a model cell to the two-part error function consisting of the adapting frequency-current (f-I) response (Fig. 2A₁, black lines) and membrane potential decay after depolarization (Fig. 2A₂, gray solid line). Comparison between the electrophysiological recordings of the fitted cell (Fig. 2B_{1,2}) and the resulting model (Fig. 2C_{1,2}) during current step injection indicates that the typical firing characteristics of the tonic cell was well reproduced by the model. The generated models allow studying the effect of the adaptation current I_{KA} . Removal of the latter current results in an f_{∞} response (Fig. 2A₁, gray line) that is less linear. This general linearization effect of adaptation has been shown analytically (Ermentrout, 1998). However, the firing behavior of tonic 2°VN models, classified as class 1 excitability (Hodgkin, 1948), remained unchanged by the removal of I_{KA} as indicated by the steady state f_{∞} response (Fig. 2A₁, black line) that remained continuous (Izhikevich, 2006).

The necessity for generating a compartmental model and fitting with the two-part error function becomes obvious when a simple RC model (dendritic compartments were removed) was fitted to the frequency-current response only. The membrane potential decay of the resulting model (Fig. 2A₂, gray dashed line) showed that the membrane time constant was otherwise underestimated. The generated compartmental tonic 2°VN models that were fitted with the two-part error function not only reproduced the typical firing behavior during current step injections but also during stimulation with sinusoidally modulated pulse trains that consisted of single pulses of quadratically increasing frequency (ZAP stimuli). Following ZAP stimulation, tonic 2°VN (Fig. 3A₁) and the corresponding model (Fig. 3A₂) activated spikes beginning at the lowest frequency and stopped firing at frequencies at ~50 Hz. This spiking behavior appeared to have simple low-pass filter characteristics, however, closer analysis of the interspike rate amplitude at each frequency ($\Delta I F / \Delta I$) (Fig. 3B₁) indicated that the neurons (black line) as well as the models (gray line) exhibited a band-pass filter behavior with a resonance peak at ~4 Hz. This band-pass behavior is attributable to the adaptation current I_{KA} . Removal of this current from the models (Fig. 3B₂, dashed line) resulted in an increased $\Delta I F / \Delta I$ response with a typical low-pass behavior. However, the adaptation not only had an influence on the amplitude but also on the phase (Fig. 3B₃). Both, data and model responses (Fig. 3B₃, gray and black lines, respectively) showed a strong phase lead already at low frequencies. Removal of the adaptation current I_{KA} from the model considerably reduced

the phase lead (Fig. 3E, black dashed line). Apart from the reproduction of the typical firing pattern of tonic 2°VN, the resulting models also showed the typical subthreshold response behavior: the impedance magnitude increased with membrane depolarization (Fig. 4A₁) and during ZAP stimulation the depolarizing response components were larger in magnitude compared to the hyperpolarizing half waves (Fig. 4A₂) (Beraneck et al., 2007). This effect in the model is caused by the window current of the standard fast sodium conductance, which originated from the overlap of activation and inactivation profiles (Fan et al., 1994; Parri and Crunelli, 1998), rather than from the more complex non-inactivating sodium or calcium conductances as previously suggested (Beraneck et al., 2007; Pfanzelt et al., 2008; Rössert et al., 2009). However, it cannot be excluded that these latter channels may also contribute to the specific subthreshold membrane properties as in other neurons (Johnston et al., 1994).

Model of phasic second-order vestibular neurons

At variance with the response properties of tonic 2°VN, phasic 2°VN exhibit a decrease in impedance magnitude with depolarization (Beraneck et al., 2007). This effect was well reproduced by including a low-threshold potassium channel (I_D) in the fitted frequency domain subthreshold models (Fig. 4B₁). The kinetics of the I_{LT} channel described by Rothman and Manis (2003) yields a good estimation for the assumed I_D channel in phasic 2°VN. The resulting phasic subthreshold models reproduced the typical asymmetry of the sinusoidally modulated membrane potential (Fig. 4B₂) consisting of larger hyperpolarizing compared to depolarizing half waves (Beraneck et al., 2007).

In the following, the fitting results of time-domain phasic models were compared with intracellularly recorded responses of phasic 2°VN. Figure 5A illustrates an exemplary fit of a spiking time-domain model to a phasic 2°VN with the two-part error function of frequency-current response (Fig. 5A₁) and membrane potential decay (Fig. 5A₂). The frequency-current response is limited to f_0 , since the evoked discharge is restricted to a single spike at the beginning of the stimulation and thus f_1, f_2 and f_∞ are zero. The responses of the resulting model during current step injections (Fig. 5B₂) showed that the typical class 3 excitability (definition by Hodgkin (1948), also see Izhikevich (2006)) of phasic neurons is reproduced (Fig. 5B₁). Furthermore the model responses during low-amplitude ZAP current injections (Fig. 5C₂, black trace) as well as during higher-amplitude ZAP current injections that evoked

spike discharge (Fig. 5D₂, black trace) were in good agreement with the actual intracellular recordings (Fig. 5C₁ and 5D₁).

As shown in Beraneck et al. (2007), the response peak frequency of the ZAP stimulus-evoked responses in phasic 2°VN is shifted to higher values with depolarization by, e.g. constant current injection (Fig. 5C₂, gray trace). This depolarization-related shift in subthreshold response peak frequency consequently results in a shift of the discharge sensitivity to higher frequencies (Fig. 5D₂, gray trace). To further examine this dependency, the ZAP response peak frequency was evaluated in the phasic 2°VN model at different holding currents (I_{hold}) and ZAP stimulus amplitudes (I_0) (Fig. 5E), which impressively illustrated the depolarization-induced shift in ZAP response peak frequency. Furthermore, the response peak frequency depends on the amplitude of the ZAP stimulus due to non-linear effects of the I_D channel. Interestingly, with larger depolarizing holding currents the ZAP response peak frequencies from stimuli with different amplitudes coincided more and more, suggesting the presence of a particular parameter value where maximal potential deflections saturate.

Synaptic activation of second-order vestibular neuron models

The dynamics of synaptic signal processing by the 2°VN models was determined mimicking simulation with sinusoidally modulated synaptic stimulus trains applied to vestibular afferent fibers (Pfanzelt et al., 2008), exemplarily shown for one tonic and one phasic 2°VN model (Fig. 6). The synaptically activated 7 tonic models (Fig. 6A₁) were characterized as in the electrophysiological measurements, by a subthreshold EPSP compound response with an overall waveform that was aligned with stimulus frequency modulation (Fig. 6A₂) and by an activation of spikes with increasing synaptic conductance that started around the peak stimulus frequency and continued symmetrically until each stimulus pulse triggered a spike (Fig. 6A_{3,4}). In phasic 2°VN models, mimicking synaptic excitation from vestibular nerve afferents (Fig. 6B₁), the prominent early decay of the subthreshold EPSP compound response which characterized the response of these neurons in electrophysiological recordings (Pfanzelt et al., 2008) was absent (Fig. 6B₂). It was replaced by a symmetrical response similar to that observed in tonic 2°VN models. With increased synaptic conductance, spikes were only evoked during the first single pulses of the pulse train in 5 out of 17 model neurons (Fig. 6B₃). In the remaining models and all models that were stimulated with a high synaptic conductance, spikes were triggered by the first as well as the last single pulses (Fig. 6B₄).

Importantly, no phasic 2°VN model was encountered that elicited spikes around the center of the stimulus pulse train (Fig. 6B_{3,4}). The incompatibility of the symmetric subthreshold response (Fig. 6B₂) and the activation of spikes by the last single pulses of the stimulus train with the actual recordings required a modification of the phasic cell models. Compatible with anatomical and electrophysiological data (Straka et al., 1997; Biesdorf et al., 2008; Malinvaud et al., 2010), a synaptic inhibition through local GABAergic and glycinergic circuits was added. As suggested earlier by Minor and Goldberg (1991), this inhibition is mediated by tonic type 2°VN that are activated by vestibular afferents (Fig. 6C₁). The insertion of all 7 tonic 2°VN as inhibitory interneurons (Fig. 6C₁) accounted for the skewed subthreshold response (Fig. 6C₂) and prevented spiking at the end of the synaptic stimulation (Fig. 6C_{3,4}), compatible with recorded data (Pfanzelt et al., 2008).

Population responses of second-order vestibular neuron models

Evaluation of the qualitative contributions of ion channels, inhibition, asynchronous afferent fiber input and synaptic noise to the signal transmission in the vestibular system of the frog was studied by generation of a population model. The functional output of tonic and phasic cell populations (population response) was analyzed by determination of the theoretical postsynaptic conductance (G_S) onto a hypothetically innervated target neuron (e.g. extraocular motoneuron). For simplification, the responses were computed for one postsynaptic neuron, respectively, that was innervated by convergence of either 200 phasic or 200 tonic 2°VN. This analysis took into account synaptic integration and summation at the postsynapse (see Methods).

Excitation of the population model with a sinusoidally modulated train of single electrical pulses in each tonic 2°VN model cell resulted in a symmetrical population response (Fig. 7A₁, control) with a gain that increased considerably with reduction of the adaptation potassium current I_{KA} (Fig. 7A₁, 50% I_{KA}). In contrast, the phasic 2°VN model population caused a typical asymmetric response with a large transient response at the beginning and a small response at the end of the stimulus train (Fig. 7A₂, control). The postsynaptic activation at the end of the stimulus train is mediated by a small number of phasic model neurons with a particularly low I_D conductance where the implemented feed-forward inhibition was too weak to prevent spiking during the last pulses of the stimulus train. Further reduction of the I_D conductance in each of the model cells by 50% (Fig. 7A₂, black dashed line) increased the

population response, both at the beginning and the end of the stimulus train. In contrast, reduction of the feed-forward inhibition by 50% had a larger impact on the response component at the end of the stimulus train (Fig. 7A₂, gray line).

To simulate a more natural vestibular input, e.g. by asynchronously activated single afferent fibers and synaptic noise, a noisy sinusoidally modulated current was injected into each target cell (see Methods). Figure 7B_{1,2} illustrates the postsynaptic conductance amplitude ΔG_s with respect to the stimulus frequency for the tonic (Fig. 7B₁) and for the phasic model population (Fig. 7B₂). In control conditions (Fig. 7B_{1,2}, black lines), the tonic neuron population exhibited a typical low-pass filter behavior, while the phasic neuron population showed the typical band-pass behavior. Notably however, the resonance observed in the firing rates of individual tonic 2°VN (see Fig. 3B₁) was absent in the postsynaptic responses. In contrast, removal of the adaptation current I_{KA} in tonic 2°VN (Fig. 7B₁, gray line) caused a considerably increased gain along with a shift of the cut-off frequency towards lower values (Fig. 7B₁, inset).

Reduction of the low-threshold potassium current (I_D) to 50% in each phasic model neuron (Fig. 7B₂, black dotted lines) resulted in enhanced amplitudes during low stimulus frequencies and a large shift of the resonance peak towards lower frequencies. Reduction of the inhibition to 50% (Fig. 7B₂, black dashed lines) or 0% (Fig. 7B₂, gray solid lines) also caused a gain increase that was accompanied only by a small resonance shift to lower frequencies. Interestingly, without inhibition, phasic model cells exhibited an activity at low stimulus frequencies, which was not the case in control conditions. This effect is largely due to the noise current. Removal of this latter current, while maintaining 0% inhibition (Fig. 7B₂, gray dashed lines) caused a general decrease of the activity, specifically at low stimulus frequencies, leaving only few phasic 2°VN with a particularly low I_D active. In contrast, amplifying the noise current to 200%, while maintaining 0% inhibition strongly enhanced the postsynaptic conductance amplitude evoked at low stimulus frequencies and almost entirely removed the resonance peak (Fig. 7B₂, gray dotted lines).

As demonstrated above, the dynamics and frequency tuning of the postsynaptic input onto presumed target neurons of tonic and phasic 2°VN, e.g. extraocular motoneurons, are to a large extent determined by intrinsic and synaptic properties of the presynaptic 2°VN. However, time constants of the synapses between 2°VN and the target neurons can either reinforce or antagonize the presynaptic properties. In particular, reduction of the time constants of the activated model alpha-synapses from $\tau_{syn} = 30$ ms to $\tau_{syn} = 5$ ms (Fig. 7C)

revealed how this parameter changes vestibulo-motor response dynamics. Shortening of the time constant unmasked a pronounced resonance in the tonic 2°VN-mediated postsynaptic population response (Fig. 7C₁, inset) similar to the resonance in the firing rate of individual tonic 2°VN (Fig. 3B₁).

A similar effect was seen in the phasic 2°VN population response. The noise current eventually created voltage transients that were fast enough to trigger action potentials in phasic 2°VN and as a consequence a postsynaptic conductance in the presumed target neuron. However, the magnitude of the postsynaptic time constant determined the degree of integration of the relayed signals. A long time constant caused integration of the activated conductance during the depolarizing half wave, visible as a high gain at low frequencies below 1 Hz (Fig. 7B₂, gray lines). Higher stimulus frequencies finally caused synaptic integration to exceed the cycle duration of the sinusoidally modulated stimulus waveform. Consequently, this increased the overall signal amplitude at the expense of postsynaptic signal dynamics, thereby decreasing the gain, seen as a dip at ~3 Hz in the phasic 2°VN population response without feed-forward inhibitory inputs and a long τ_{syn} (Fig. 7B₂, gray lines). Above a particular stimulus frequency, action potentials are triggered independent of the amount of noise current in phasic 2°VN, which caused a substantial gain increase above 3 Hz with maximal values at ~10 Hz (gray * in Fig. 7B₂). In contrast, a short time constant of the presumed postsynaptic target neuron limits the integration of the postsynaptic conductance. This results in particular low gains of the postsynaptic conductance for the frequency range up to ~3 Hz but causes an enhancement of the response resonance peaks and a shift of the latter to considerably higher frequencies independent of other conditions (compare plots in Fig. 7B₂, C₂).

Comparison of the consequences of short and long time constants of 2°VN synapses onto vestibular target neurons thus yields important information on how the processing of sensory signals in central vestibular neurons can be enhanced or antagonized at the next synaptic level within e.g. the vestibulo-ocular circuitry. A short postsynaptic time constant limits synaptic integration, thereby ensuring a more or less unaltered transformation of pre- into postsynaptic signals including particular expressions of response resonance phenomena. In contrast, a long synaptic time constant causes signal integration over longer time periods, thereby cancelling or diminishing potential presynaptic response resonances observed in both tonic and phasic 2°VN. The extension of the single cell model to a population model proved to be extremely useful for an estimation of how the feed-forward inhibition and specific potassium

conductances control particular aspects of the sensory signal transformation in 2°VN and the transmission to target neurons under semi-natural conditions. The obtained results suggest a critical influence of synaptic noise as well as properties of the postsynapse on the timing and sharpness of effective vestibular signal processing.

Discussion

Frog phasic and tonic 2°VN form two separate subpopulations with distinctly different, yet complementary membrane properties that cause different synaptic signal processing in the two cell types, respectively. The clear categorization and differential embedding into synaptic environments of phasic and tonic 2°VN make the two types excellent models for studying the respective contributions of intrinsic cellular and emerging network characteristics to the generation of vestibulo-motor commands in a computational approach. The compartmental Hodgkin-Huxley type models reproduced the distinct behavior of both subgroups and allowed making predictions of the respective functional roles of ion conductances, noise currents, synaptic inhibition and postsynaptic time constants for vestibular signal processing.

Functional reliability of vestibular cellular models

Intrinsic membrane properties assign to frog tonic 2°VN a low-pass filter based frequency-dependency of subthreshold responses (Beraneck et al., 2007). In contrast to this, the frequency dependent spike rate reveals a prominent band-pass characteristics with a resonance peak around ~4 Hz that is reproduced by a potassium conductance-based adaptation process with a time constant of ~50 ms. Since this current has no effect on the subthreshold and impedance response, it is possible that the resulting spike rate adaptation is caused by high-threshold calcium and calcium-dependent potassium currents (Ermentrout, 1998; Benda and Herz, 2003). The somewhat surprising combination of low-pass subthreshold and resonant spike discharge might be due to calcium-dependent potassium-activated adaptation mechanisms as in chicken MVN neurons (du Lac, 1996), which cause the observed linear current-firing rate relationship (du Lac and Lisberger, 1995; Bagnall et al., 2008). In mammalian type B MVN neuron models (Av-Ron and Vidal, 1999), an apamin-sensitive calcium-dependent (SK type) potassium channel (Serafin et al., 1991a, 1991b; Johnston et al., 1994; Smith et al., 2002) causes spike rate adaptation and a resonance similar to frog tonic 2°VN. The similarity between the two types, however, is at variance with

different functional roles in vestibular signal processing, respectively (Straka et al., 2005). In mammals, the more phasic non-linear response dynamics of type B MVN neurons is complemented by a more tonic response dynamics of type A MVN neurons (Ris et al., 2001), while in frog, tonic 2°VN complement the highly non-linear phasic 2°VN (Straka et al., 2005).

Particular details of the frequency-domain neuronal models suggest that the low-threshold Kv1.1 (I_D) potassium channel of frog phasic 2°VN is the essential component that assigns to these neurons the particular phasic response properties. This conductance is similar to the low-threshold potassium current (I_{LT}) of bushy ventral cochlear nucleus neurons (Rothman and Manis (2003), which show a strikingly similar firing pattern as frog phasic 2°VN (Peusner et al., 1998). However, a hyperpolarization-activated cation current (I_h), is present in the former but absent in the latter neurons, indicating that the I_D channel is the major determinant for the highly adaptive response properties. The generated band-pass filter-like characteristics of subthreshold responses in phasic 2°VN and the polarization-dependent response peak around ~10-50 Hz align well with the discharge preference that limits repetitive spike discharge (Beraneck et al., 2007).

Network contribution to signal processing in vestibular neuronal models

Simulation of simple synaptic excitation in tonic 2°VN models was sufficient to reproduce the linear and symmetric responses (Fig. 6A) observed during electrophysiological measurements (Pfanzelt et al., 2008). In contrast, the characteristic pronounced subthreshold compound response peak asymmetry and temporally limited early spike discharge in phasic 2°VN models (Figs. 1A, 6B,C) required flexible contributions of delayed inhibitory inputs through tonic type 2°VN, compatible with previous studies (Straka et al., 1997; Pfanzelt et al., 2008). The contribution of local inhibitory networks to band-pass filtering of vestibular nerve-activated excitation, however, depends on the extent of afferent activity. During recruitment of small numbers of afferent fibers, the I_D channel was sufficient to prevent continuous spike discharge in phasic model neurons (Fig. 6B₃). Larger numbers of activated afferent fibers, however required additional inhibitory inputs from tonic type 2°VN to prevent spike discharge during most of the stimulus train (compare Fig. 6B₄,C₄). Thus, both intrinsic cellular and emerging network properties are functionally co-adapted and act synergistically,

even though with different temporal contributions, to generate the filter properties for limiting and sharpening the discharge dynamics in phasic 2°VN (Beraneck et al., 2007). Such a coadaptation of intrinsic membrane and network properties has been shown before in the Mautner cell in fish (Nakayama and Oda, 2004) where recurrent inhibition and membrane properties both contribute to phasic spiking behavior. Just recently it could be shown that in addition to the well examined ipsi- and contralateral inhibition on medial superior olive (MSO) neurons (Grothe, 2003) also low-threshold potassium channels (Kv1) in the latter neurons are crucial for binaural coincidence detection (Mathews et al., 2010).

Population simulation of second-order vestibular neuron models

Calculation of postsynaptic conductances (G_S) in e.g. extraocular motoneurons, activated by phasic and tonic model populations allowed testing the contributions of different critical parameters to sensory-motor transformation of vestibular signals. Since diffusive noise is an important factor for the response fidelity in the vestibular system (Hospedales et al., 2008) the model populations were stimulated mimicking noisy synaptic afferent input to reveal its effect on the response behavior of 2°VN.

This procedure essentially confirmed the functional roles of intrinsic cellular and emerging network properties of phasic 2°VN but also revealed several relations that were not directly evident from the empirical data. The dynamics of the constructed postsynaptic responses critically depends on the synaptic time constant that either reinforced (small τ_{syn}) or counteracted (large τ_{syn}) the 2°VN filter properties. The observed discharge resonance at ~ 4 Hz in tonic 2°VN is only transmitted to postsynaptic targets if τ_{syn} is small, but is low-pass filtered if τ_{syn} is large because of synaptic conductance integration. Thus, a linear low-pass filter-shaped synaptic transmission between tonic 2°VN and postsynaptic targets requires synapses with a long time constant. On the presynaptic side, the adaptation conductance I_{KA} in tonic 2°VN can also balance this critical relationship by increasing the cut-off frequency when τ_{syn} is large, which helps maintaining a constant (linear) gain for frequencies <10 Hz.

Sensory-motor transformation in phasic 2°VN depends on intrinsic membrane properties as well as ipsilateral feed-forward inhibition (Goldberg et al., 1987; Straka and Dieringer, 2004). A previous semi-quantitative model suggested that this inhibition potentially silences inputs from irregularly firing afferents (Minor and Goldberg, 1991). The current modeling approach revealed several aspects that shed more light onto possible roles of this circuitry for filtering

afferent inputs. In the absence of synaptic inhibition, phasic population responses are characterized by relatively high gains (Fig. 7B₂) at low frequencies where a discharge is usually absent. This gain increase is due to noisy signals (membrane potential fluctuations) that eventually create voltage transients that are fast enough to trigger spikes during the depolarizing stimulus half-cycle. However, such high gains occur only when the synaptic time constant τ_{syn} is large. In contrast, small time constants cause an amplification of the resonance and a shift to lower frequencies (Fig. 7C₂). Thus, the feed-forward inhibition allows silencing responses in the frequency range of 0.1-4 Hz, compatible with the study by Minor and Goldberg (1991). With increasing frequency, however, the disynaptic inhibition decreases due to cessation of firing in the mediating local tonic 2°VN and as a consequence phasic 2°VN are released from the discharge suppression. Functionally, the inhibitory side-loop thus acts as high-pass filter, which controls the resonance frequency of phasic 2°VN. This is particularly obvious when the postsynaptic time constant is short. In this case, intrinsic membrane properties along with synaptic inhibition sharpen the band-pass properties of the phasic population response in the postsynaptic target neuron. Reduction of either of the two latter parameters makes e.g. vestibulo-ocular signal processing more sensitive for responses at lower frequencies.

Even though, many of the actual synaptic properties in the population model are still unknown, the results clearly indicate that the output of the system critically depends on the integrational capabilities of the postsynaptic synapse. In addition, the integrational membrane properties (Segev and London, 2000; Magee, 2000) of the postsynaptic neurons will also contribute to shaping vestibulo-motor outputs. As the synaptic current integration increases with distance from the soma (Rall et al., 1967) the amount of 2°VN resonance antagonization at the next synaptic level thus directly depends on the site of the synaptic contact. Distant locations of synapses on e.g. extraocular motoneurons would thus facilitate integration of vestibular inputs and reinforce signals from tonic 2°VN (Fig. 7B₁), while synapses closer to the soma reduce integration, thereby amplifying inputs from phasic 2°VN (Fig. 7C₂). Thus, the integrational capabilities of the postsynaptic synapse and neuron are important factors that contribute to the generation of dynamically appropriate vestibulo-motor commands.

References

- Anastasio TJ, Robinson DA (1989) The distributed representation of vestibulo-oculomotor signals by brain-stem neurons. *Biol Cybern* 61:79-88.
- Arsiero M, Lüscher H, Lundstrom BN, Giugliano M (2007) The impact of input fluctuations on the frequency-current relationships of layer 5 pyramidal neurons in the rat medial prefrontal cortex. *J Neurosci* 27:3274-3284.
- Av-Ron E, Vidal PP (1999) Intrinsic membrane properties and dynamics of medial vestibular neurons: a simulation. *Biol Cybern* 80:383-392.
- Bagnall MW, McElvain LE, Faulstich M, du Lac S (2008) Frequency-independent synaptic transmission supports a linear vestibular behavior. *Neuron* 60:343-352.
- Benda J, Herz AVM (2003) A universal model for spike-frequency adaptation. *Neural Comput* 15:2523-2564.
- Beraneck M, Idoux E, Uno A, Vidal P, Moore LE, Vibert N (2004) Unilateral labyrinthectomy modifies the membrane properties of contralesional vestibular neurons. *J Neurophysiol* 92:1668-1684.
- Beraneck M, Pfanzelt S, Vassias I, Rohregger M, Vibert N, Vidal P, Moore LE, Straka H (2007) Differential intrinsic response dynamics determine synaptic signal processing in frog vestibular neurons. *J Neurosci* 27:4283-4296.
- Biesdorf S, Malinvaud D, Reichenberger I, Pfanzelt S, Straka H (2008) Differential inhibitory control of semicircular canal nerve afferent-evoked inputs in second-order vestibular neurons by glycinergic and GABAergic circuits. *J Neurophysiol* 99:1758-1769.
- Blanks RHI, Precht W (1976) Functional characterization of primary vestibular afferents in the frog. *Exp Brain Res* 25:369-390.
- Camp AJ, Callister RJ, Brichta AM (2006) Inhibitory synaptic transmission differs in mouse type A and B medial vestibular nucleus neurons in vitro. *J Neurophysiol* 95:3208-3218.
- Cartwright AD, Gilchrist DPD, Burgess AM, Curthoys IS (2003) A realistic neural-network simulation of both slow and quick phase components of the guinea pig VOR. *Exp Brain Res* 149:299-311.
- Carnevale NT, Hines ML (2009) *The NEURON Book* 1. ed. Cambridge University Press.
- Clendaniel RA, Lasker DM, Minor LB (2002) Differential adaptation of the linear and nonlinear components of the horizontal vestibuloocular reflex in squirrel monkeys. *J Neurophysiol* 88:3534-3540.
- Clopath C, Jolivet R, Rauch A, Lüscher H, Gerstner W (2007) Predicting neuronal activity with simple models of the threshold type: Adaptive exponential integrate-and-fire model with two compartments. *Neurocomputing* 70:1668-1673.
- Dayan P, Abbott LF (2001) *Theoretical Neuroscience: Computational and Mathematical*

Modeling of Neural Systems 1. ed. The MIT Press.

Dieringer N, Precht W (1977) Modification of synaptic input following unilateral labyrinthectomy. *Nature* 269:431-433.

Dieringer N, Precht W (1979) Mechanisms of compensation for vestibular deficits in the frog. I. Modification of the excitatory commissural system. *Exp Brain Res* 36:311-328.

Ermentrout B (1998) Linearization of F-I curves by adaptation. *Neural Comput* 10:1721-1729.

Fan S, Stewart M, Wong RK (1994) Differences in voltage-dependent sodium currents exhibited by superficial and deep layer neurons of guinea pig entorhinal cortex. *J Neurophysiol* 71:1986-1991.

Frankenhaeuser B, Huxley AF (1964) The action potential in the myelinated nerve fibre of *Xenopus laevis* as computed on the basis of voltage clamp data. *J Physiol* 171:302-315.

Glasauer S (2007) Current models of the ocular motor system. *Dev Ophthalmol* 40:158-174.

Goldberg JM, Highstein SM, Moschovakis AK, Fernandez C (1987) Inputs from regularly and irregularly discharging vestibular nerve afferents to secondary neurons in the vestibular nuclei of the squirrel monkey. I. An electrophysiological analysis. *J Neurophysiol* 58:700-718.

Green AM, Angelaki DE (2003) Resolution of sensory ambiguities for gaze stabilization requires a second neural integrator. *J Neurosci* 23:9265-9275.

Grillner S (2003) The motor infrastructure: from ion channels to neuronal networks. *Nat Rev Neurosci* 4:573-586.

Hodgkin AL (1948) The local electric changes associated with repetitive action in a non-medullated axon. *J Physiol* 107:165-181.

Holler S, Straka H (2001) Plane-specific brainstem commissural inhibition in frog second-order semicircular canal neurons. *Exp Brain Res* 137:190-196.

Hospedales TM, van Rossum MCW, Graham BP, Dutia MB (2008) Implications of noise and neural heterogeneity for vestibulo-ocular reflex fidelity. *Neural Comput* 20:756-778.

Izhikevich EM (2006) *Dynamical Systems in Neuroscience: The Geometry of Excitability and Bursting* 1. ed. The MIT Press.

Johnston AR, MacLeod NK, Dutia MB (1994) Ionic conductances contributing to spike repolarization and after-potentials in rat medial vestibular nucleus neurones. *J Physiol* 481:61-77.

Johnston D, Wu SM (1994) *Foundations of Cellular Neurophysiology*. The MIT Press.

du Lac S, Lisberger S (1995) Cellular processing of temporal information in medial vestibular

nucleus neurons. *J Neurosci* 15:8000-8010.

du Lac S (1996) Candidate cellular mechanisms of vestibulo-ocular reflex plasticity. *Ann NY Acad Sci* 781:489-498.

Lisberger SG, Miles FA, Optican LM (1983) Frequency-selective adaptation: evidence for channels in the vestibulo-ocular reflex? *J Neurosci* 3:1234-1244.

Magee JC (2000) Dendritic integration of excitatory synaptic input. *Nat Rev Neurosci* 1:181-190.

Malinvaud D, Vassias I, Reichenberger I, Rössert C, Straka H (2010) Functional organization of vestibular commissural connections in frog. *J Neurosci* 30:3310-3325.

Mathews PJ, Jercog PE, Rinzel J, Scott LL, Golding NL (2010) Control of submillisecond synaptic timing in binaural coincidence detectors by Kv1 channels. *Nat Neurosci* 13:601-609.

Minor LB, Goldberg JM (1991) Vestibular-nerve inputs to the vestibulo-ocular reflex: a functional-ablation study in the squirrel monkey. *J Neurosci* 11:1636-1648.

Morris C, Lecar H (1981) Voltage oscillations in the barnacle giant muscle fiber. *Biophys J* 35:193-213.

Murphey CR, Moore LE, Buchanan JT (1995) Quantitative analysis of electrotonic structure and membrane properties of NMDA-activated lamprey spinal neurons. *Neural Comput* 7:486-506.

Nakayama H, Oda Y (2004) Common sensory inputs and differential excitability of segmentally homologous reticulospinal neurons in the hindbrain. *J Neurosci*. 24:3199-3209.

Parri HR, Crunelli V (1998) Sodium current in rat and cat thalamocortical neurons: Role of a non-inactivating component in tonic and burst firing. *J Neurosci* 18:854-867.

Peusner K, Gamkrelidze G, Giaume C (1998) Potassium currents and excitability in second-order auditory and vestibular neurons. *J Neurosci Res* 53:511-520.

Pfanzelt S, Rössert C, Rohregger M, Glasauer S, Moore LE, Straka H (2008) Differential dynamic processing of afferent signals in frog tonic and phasic second-order vestibular neurons. *J Neurosci* 28:10349-10362.

Pospischil M, Toledo-Rodriguez M, Monier C, Piwkowska Z, Bal T, Frégnac Y, Markram H, Destexhe A (2008) Minimal Hodgkin-Huxley type models for different classes of cortical and thalamic neurons. *Biol Cybern* 99:427-441.

Prescott SA, De Koninck Y, Sejnowski TJ (2008) Biophysical basis for three distinct dynamical mechanisms of action potential initiation. *PLoS Comput Biol* 4:e1000198.

- Quadroni R, Knöpfel T (1994) Compartmental models of type A and type B guinea pig medial vestibular neurons. *J Neurophysiol* 72:1911-1924.
- Rall W, Burke RE, Smith TG, Nelson PG, Frank K (1967) Dendritic location of synapses and possible mechanisms for the monosynaptic EPSP in motoneurons. *J Neurophysiol* 30:1169-1193.
- Rall W (1969) Time constants and electrotonic length of membrane cylinders and neurons. *Biophys J* 9:1483-1508.
- Ramachandran R, Lisberger SG (2006) Transformation of vestibular signals into motor commands in the vestibuloocular reflex pathways of monkeys. *J Neurophysiol* 96:1061-1074.
- Ramachandran R, Lisberger SG (2008) Neural substrate of modified and unmodified pathways for learning in monkey vestibuloocular reflex. *J Neurophysiol* 100:1868-1878.
- Raphan T, Cohen B (2002) The vestibulo-ocular reflex in three dimensions. *Exp Brain Res* 145:1-27.
- Richardson MJE, Silberberg G (2008) Measurement and analysis of postsynaptic potentials using a novel voltage-deconvolution method. *J Neurophysiol* 99:1020-1031.
- Ris L, Hachemaoui M, Vibert N, Godaux E, Vidal PP, Moore LE (2001) Resonance of spike discharge modulation in neurons of the guinea pig medial vestibular nucleus. *J Neurophysiol* 86:703-716.
- Rössert C, Straka H, Glasauer S, Moore LE (2009) Frequency-domain analysis of intrinsic neuronal properties using high-resistant electrodes. *Front Neurosci* 3:64.
doi:10.3389/neuro.17.002.2009
- Rothman JS, Manis PB (2003) The roles potassium currents play in regulating the electrical activity of ventral cochlear nucleus neurons. *J Neurophysiol* 89:3097-3113.
- Serafin M, de Waele C, Khateb A, Vidal PP, Mühlethaler M (1991a) Medial vestibular nucleus in the guinea-pig. II. Ionic basis of the intrinsic membrane properties in brainstem slices. *Exp Brain Res* 84:426-433.
- Serafin M, de Waele C, Khateb A, Vidal PP, Mühlethaler M (1991b) Medial vestibular nucleus in the guinea-pig. I. Intrinsic membrane properties in brainstem slices. *Exp Brain Res* 84:417-425.
- Segev I, London M (2000) Untangling dendrites with quantitative models. *Science* 290:744-750.
- Smith MR, Nelson AB, du Lac S (2002) Regulation of firing response gain by calcium-dependent mechanisms in vestibular nucleus neurons. *J Neurophysiol* 87:2031-2042.
- Straka H, Biesdorf S, Dieringer N (1997) Canal-specific excitation and inhibition of frog second-order vestibular neurons. *J Neurophysiol* 78:1363-1372.

Straka H, Beraneck M, Rohregger M, Moore LE, Vidal P, Vibert N (2004) Second-order vestibular neurons form separate populations with different membrane and discharge properties. *J Neurophysiol* 92:845-861.

Straka H, Dieringer N (2004) Basic organization principles of the VOR: lessons from frogs. *Prog Neurobiol* 73:259-309.

Straka H, Vibert N, Vidal PP, Moore LE, Dutia MB (2005) Intrinsic membrane properties of vertebrate vestibular neurons: function, development and plasticity. *Prog Neurobiol* 76:349-392.

Figure Legends

Figure 1. Response profiles of tonic and phasic 2°VN. **A**, Injection of a positive current steps of 1.2 nA evoked a continuous discharge in tonic (A_1) and a single spike in phasic 2°VN (A_2). **B**, Subthreshold responses (gray traces) and spike discharge (black traces, spikes truncated) of a tonic (B_1 , $I_0=0.5$ nA, $I_{\text{hold}} = 0$ (gray trace) and $I_0=1$ nA, $I_{\text{hold}} = 0$ (black trace)) and a phasic 2°VN (B_2 , $I_0=0.8$ nA, $I_{\text{hold}} = 0$ (gray trace) and $I_0=1$ nA, $I_{\text{hold}} = 0$ (black trace)) evoked by injection of sinusoidally modulated current (ZAP stimuli) with different amplitudes. **C**, Impedance magnitude at different holding currents (I_{hold}) for the tonic 2°VN (C_1 , $I_{\text{hold}}=0$ (black), $I_{\text{hold}}=0.5$ nA (gray)) and the phasic 2°VN (C_2 , $I_{\text{hold}}=0$ (black), $I_{\text{hold}}=-0.5$ nA (black dashed), $I_{\text{hold}}=0.5$ nA (gray dashed), $I_{\text{hold}}=1$ nA (gray dotted)) shown in **B**. **D,E**, Typical subthreshold compound EPSPs (**D**) and spike discharge (**E**) evoked by stimulation of individual semicircular canal nerve branches with sinusoidally modulated trains of single electrical pulses (peak frequency 70 Hz) of a tonic (D_1,E_1) and a phasic 2°VN (D_2,E_2). Pulse trains and corresponding sinusoidal modulation is shown at the bottom and apply to responses in **D,E**. Calibration bars in A_2,D_2,E_2 apply to A_1,D_1,E_1 , respectively.

Figure 2. Comparison between tonic 2°VN data and model. A_1 , Fit of a model (black lines) to frequency-current (f-I) responses of a tonic 2°VN (f_0 : circles, f_1 : diamonds, f_2 : triangles and f_∞ : squares); model f_∞ response (gray line) after removal of the adaptation current I_{KA} ($g_{KA}=0$). A_2 , Fit of a model (gray line) to the membrane potential decay (black line) of the same tonic 2°VN after injection of a current step of 0.15 nA; response (gray dashed line) of a simple RC model (dendritic compartments removed prior to fitting to f-I response). **B,C**, Spike discharge of the fitted tonic 2°VN ($B_{1,2}$) and the generated model neuron ($C_{1,2}$) evoked by a depolarizing current step of 0.6 nA (B_1,C_1) or 1.1 nA (B_2,C_2). Parameters for the tonic model neuron (T1):

$L_E = 1.05$, $\rho = 6.2$, $C_S = 84.3$ pF, $G_S = 15.5$ nS, $G_D = 3.65$ nS, $g_{Na} = 0.074$ S/cm², $g_K = 0.016$ S/cm², $\tau_n = 7.2$ ms, $g_{KA} = 0.073$ mS/cm² and $\tau_a = 58.6$ ms. Calibration bars in B_1, C_1 apply to B_2, C_2 , respectively.

Figure 3. Discharge dynamics of a tonic 2°VN and model neuron. **A**, Spike discharge of the tonic 2°VN (A_1) and the corresponding tonic model neuron (T1) (A_2), shown in Fig. 2 evoked by injection of sinusoidally modulated current (ZAP stimuli) with $I_0=0.5$ nA. **B**, Discharge behavior during ZAP stimulation ($I_0=0.5$ nA) analyzed at each frequency using spike rate ($\Delta IF/\Delta I$); **B₁**, Comparison between response of the tonic 2°VN (gray line) and the tonic model neuron (black line); **B₂**, response of the control model neuron (solid line) and after removal of the adaptation current I_{KA} ($g_{KA}=0$) (dashed line); **B₃**, Phase shift of the responses of the measured tonic 2°VN (gray line), the tonic model neuron (black line) and the model neurons after removal of the adaptation current I_{KA} ($g_{KA}=0$) (dashed line). Calibration bars in A_1 apply to A_2 .

Figure 4. Impedance dynamics and subthreshold responses of phasic and tonic model neurons. **A₁**, Impedance profiles of a tonic 2°VN model during injection of different holding currents ($I_{hold} = 0$ (black line) and $I_{hold} = 0.45$ (gray line)); **A₂**, Response of the same tonic model neuron evoked by injection of sinusoidally modulated current (ZAP stimuli) of $I_0=0.2$ nA at a depolarized membrane potential ($I_{hold} = 0.33$); parameters for the tonic model neuron (T3) are: $L_E = 0.98$, $\rho = 7.89$, $C_S = 118$ pF, $G_S = 38.1$ nS, $G_D = 13.0$ nS, $g_{Na} = 0.098$ S/cm², $g_K = 0.013$ S/cm², $\tau_n = 4.1$ ms, $g_{KA} = 0.10$ mS/cm² and $\tau_a = 44.3$ ms. Note, that the tonic model neuron was generated from data of a tonic 2°VN other than shown in Fig. 2,3. **B₁**, Fit of a model (black lines) to impedance magnitudes obtained from subthreshold responses of a phasic 2°VN at different holding currents ($I_{hold}=0$ (circles), $I_{hold}=-0.5$ nA (triangles), $I_{hold}=-1$ nA (stars), $I_{hold}=0.5$ nA (diamonds), $I_{hold}=1$ nA (squares)); **B₂**, Response of the same phasic model neuron evoked by injection of sinusoidally modulated current (ZAP stimuli) of $I_0=0.7$ nA at a depolarized membrane potential ($I_{hold} = 0.5$); parameters for the phasic model neuron (PI1) are: $L_E = 0.68$, $\rho = 3.7$, $C_S = 195$ pF, $G_S = 45.4$ nS, $G_D = 10.7$ nS, $g_{KD} = 1.51$ mS/cm² and $t_{fac} = 1.06$.

Figure 5. Comparison between phasic 2°VN data and model. **A₁**, Fit of a model (black lines) to the frequency-current (f-I) response of a phasic model neuron (f₀: circles, f₁: diamonds, f₂: triangles and f_∞: squares); **A₂**, Fit of the model (gray line) to the membrane potential decay (black line) after injection of a current step of 0.26 nA. **B**, Comparison between the evoked discharge of the fitted phasic 2°VN (**B₁**) and the resulting phasic model neuron (**B₂**) during depolarization with a current pulse of 1 nA. **C**, Subthreshold responses, evoked by sinusoidally modulated current injection (ZAP stimuli), of the same phasic 2°VN (**C₁**, I₀=0.9 nA, I_{hold}=0 nA) and the corresponding model (**C₂**, I₀=0.9 nA, I_{hold}=0 nA (black trace) and I₀=0.5 nA, I_{hold}=0.6 nA (gray trace)). **D**, Spike discharge, evoked by sinusoidally modulated current injection (ZAP stimuli), of the phasic 2°VN (**D₁**, I₀=1 nA, I_{hold}=0 nA) and corresponding model shown in **A-C** (**D₂**, I₀=1 nA, I_{hold}=0 nA (black trace) and I₀=0.52 nA, I_{hold}=0.6 nA (gray trace)). **E**, Response peak frequency during ZAP stimuli at different holding currents (I_{hold}) and stimulus amplitudes (I₀= 0.6 nA (circles), I₀=0.3 nA (triangles), I₀=0.1 nA (squares)). Parameters for the phasic model neuron (P8) are: L_E = 0.75, ρ = 6.2, C_S = 46.6 pF, G_S = 24 nS, G_D = 18.0 nS, g_{Na} = 0.1 S/cm², g_K = 0.013 S/cm², τ_n = 4.6 ms, g_{KD} = 2.57 mS/cm² and t_{fac} = 1. Calibration bars in **B₁, C₁, D₁** apply to **B₂, C₂, D₂**, respectively.

Figure 6. Synaptic subthreshold compound responses and spike discharge of tonic and phasic model neurons evoked by sinusoidally modulated pulse train stimulation (peak frequency: 70 Hz) for three different cellular and network configurations: **A**, tonic model neuron with monosynaptic afferent vestibular nerve excitation only, **B**, phasic model neuron with monosynaptic afferent vestibular nerve excitation only, **C**, same phasic model neuron with monosynaptic excitation and disynaptic inhibition from all 7 tonic model neurons; **A₁, B₁, C₁**, indicate network configuration, respectively. Excitatory synaptic conductance increases from **A₂-A₄** (A₂, g_E=1 nS; A₃, g_E=4 nS; A₄, g_E=9 nS), **B₂-B₄** (B₂, g_E=4 nS; B₃, g_E=26 nS; B₄, g_E=35 uS) and **C₂-C₄** (C₁, phasic: g_E=4 nS, tonic: g_E=4 nS; C₂, phasic: g_E=26 nS, tonic: g_E=7 nS; C₃, phasic: g_E=35 nS, tonic: g_E=9 nS). Parameters for the tonic model neuron (T4) are: L_E = 1.22, ρ = 8.5, C_S = 75.8 pF, G_S = 32.5 nS, G_D = 8.05 nS, g_{Na} = 0.125 S/cm², g_K = 0.009 S/cm², τ_n = 2.9 ms, g_{KA} = 0.106 mS/cm² and τ_a = 46.0 ms. Parameters for the phasic model neuron (P7) are: L_E = 1.41, ρ = 9.04, C_S = 41.7 pF, G_S = 35.0 nS, G_D = 30.8 nS, g_{Na} = 0.1 S/cm², g_K = 0.013 S/cm², τ_n = 4.6 ms, g_{KD} = 4.4 mS/cm² and t_{fac} = 1. Calibration bars in **A₂, B₃, B₄** apply to **B₂**, to **A₃, C₃**, and to **A₄, C₄**, respectively.

Figure 7. Role of ion channels, synaptic inhibition, noise currents and postsynaptic time constants in shaping the dynamics of population model responses. **A**, Specific implication of altered parameters on the calculated postsynaptic conductance G_S of tonic (A_1) and phasic (A_2) model neuron populations during sinusoidally modulated pulse train stimulation; overlay of control responses (black lines in A_1, A_2), without adaptation current I_{KA} ($g_{KA}=0$) in tonic population responses (gray line in A_1), with reduced (50%) low-threshold potassium currents (I_D ; black dotted line in A_2) and with reduced (50%) synaptic inhibition through local interneurons (gray line in A_2) in phasic model populations; inset in A_2 shows the response to the last pulse train stimuli at an extended time and amplitude scale; postsynaptic time constant $\tau_{syn} = 30$ ms. **B,C**, Calculated postsynaptic conductance amplitudes ΔG_S of tonic (B_1, C_1) and phasic vestibular population model responses (B_2, C_2) with large ($\tau_{syn} = 30$ ms; **B**) or small ($\tau_{syn} = 5$ ms; **C**) postsynaptic time constants; functional consequences of altered ion channel conductances (I_{KA} , I_D), magnitude of synaptic inhibition by local vestibular interneurons and noise currents (σ) on tonic and phasic population response dynamics is indicated by different symbols in **B,C**; insets in B_1, C_1 represent responses that were normalized to control values at 0.1 Hz.

Fig. 1

Rössert et al.

Cellular and network contributions to vestibular signal processing: impact of ion conductances, synaptic inhibition and noise

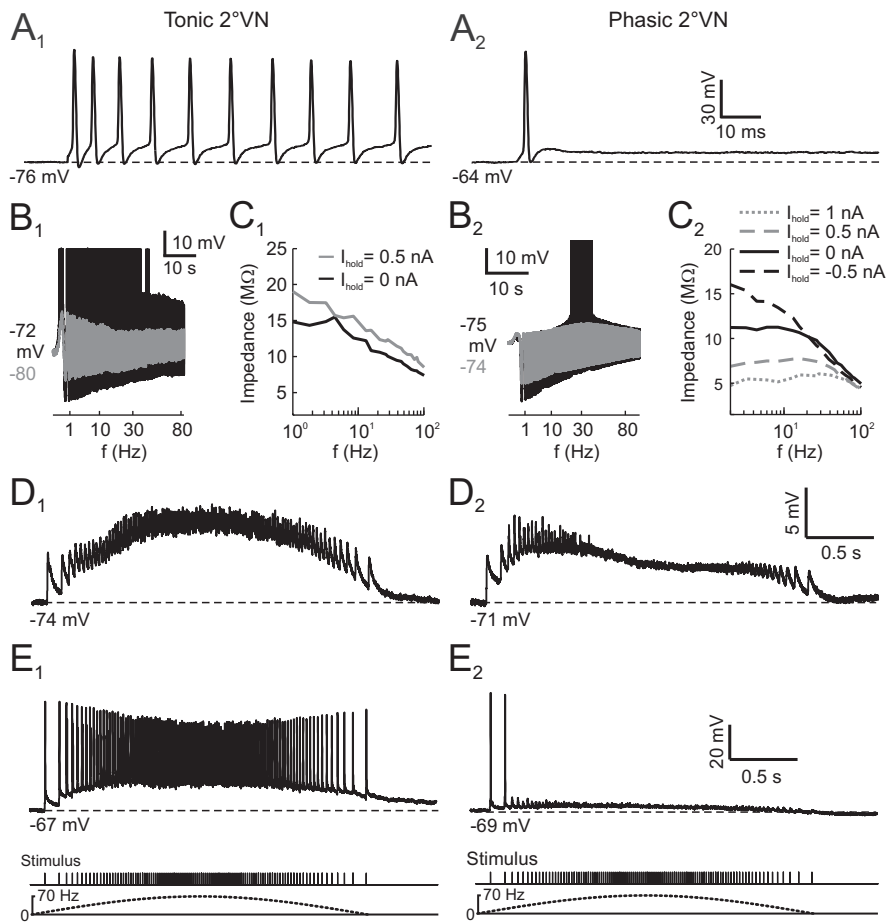


Fig. 2

Rössert et al.

Cellular and network contributions to vestibular signal processing: impact of ion conductances, synaptic inhibition and noise

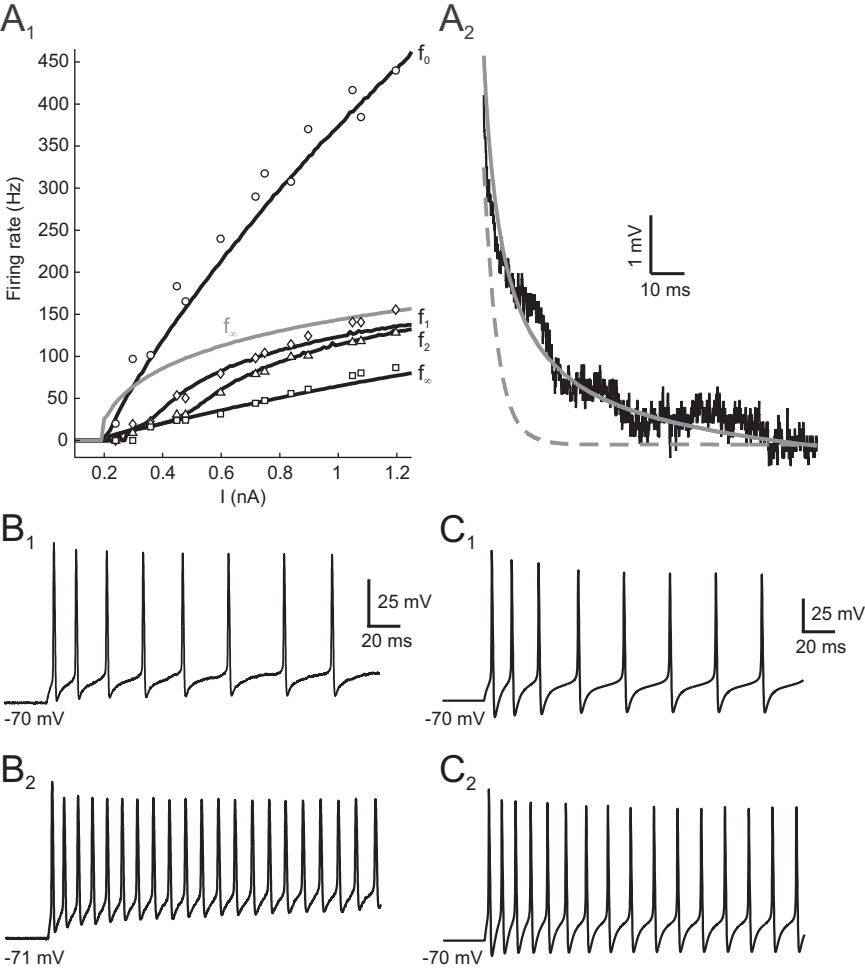


Fig. 3

Rössert et al.

Cellular and network contributions to vestibular signal processing:
impact of ion conductances, synaptic inhibition and noise

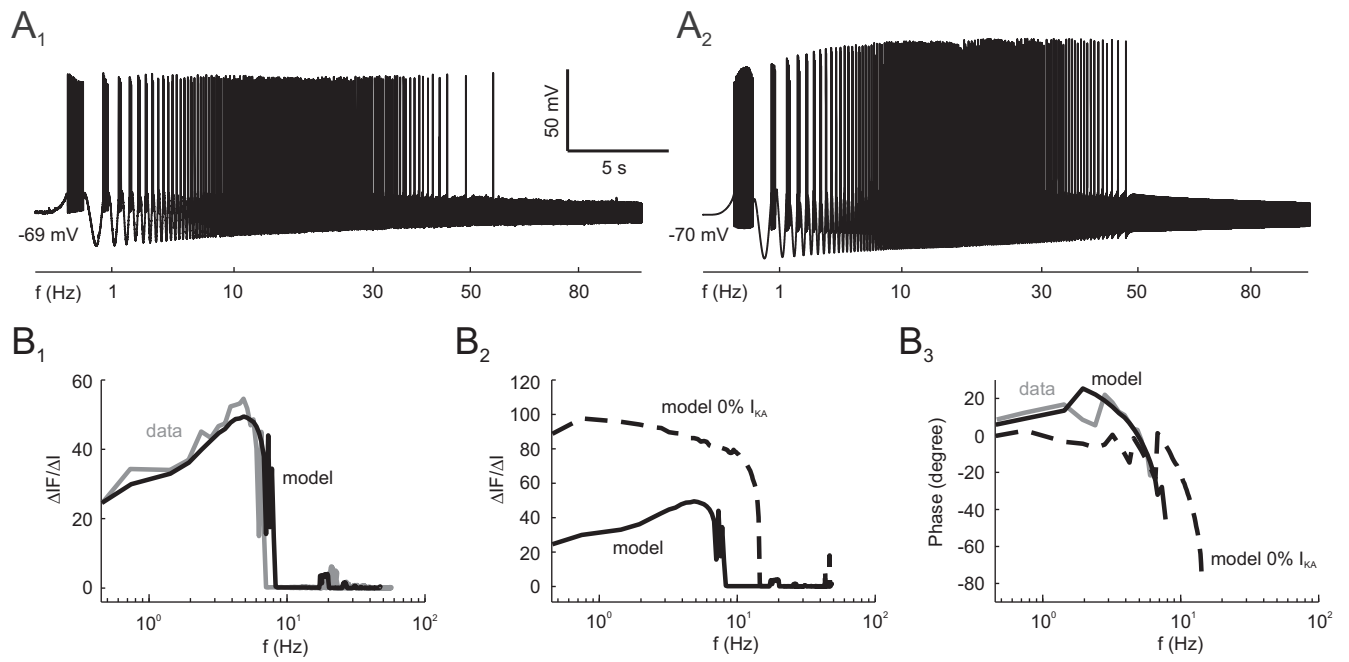


Fig. 4

Rössert et al.

Cellular and network contributions to vestibular signal processing: impact of ion conductances, synaptic inhibition and noise

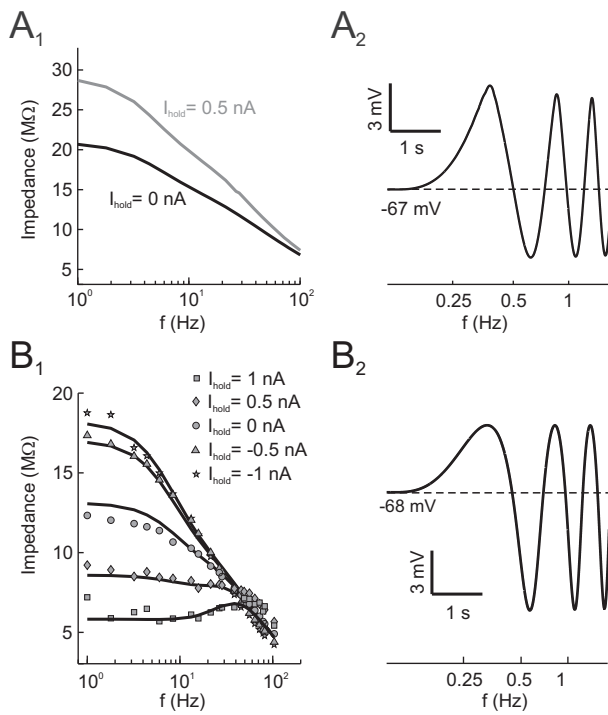


Fig. 5

Rössert et al.

Cellular and network contributions to vestibular signal processing: impact of ion conductances, synaptic inhibition and noise

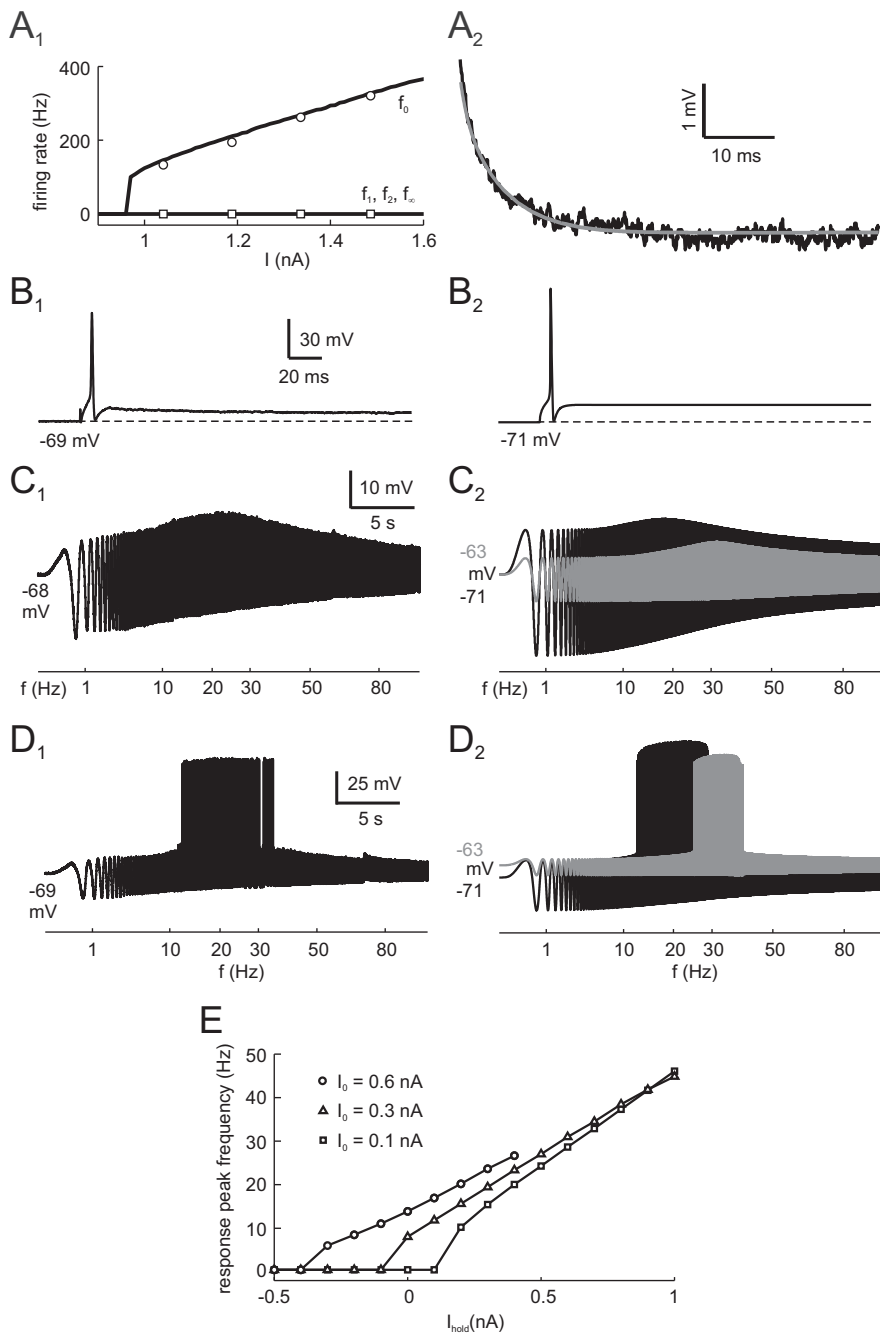


Fig. 6

Rössert et al.

Cellular and network contributions to vestibular signal processing: impact of ion conductances, synaptic inhibition and noise

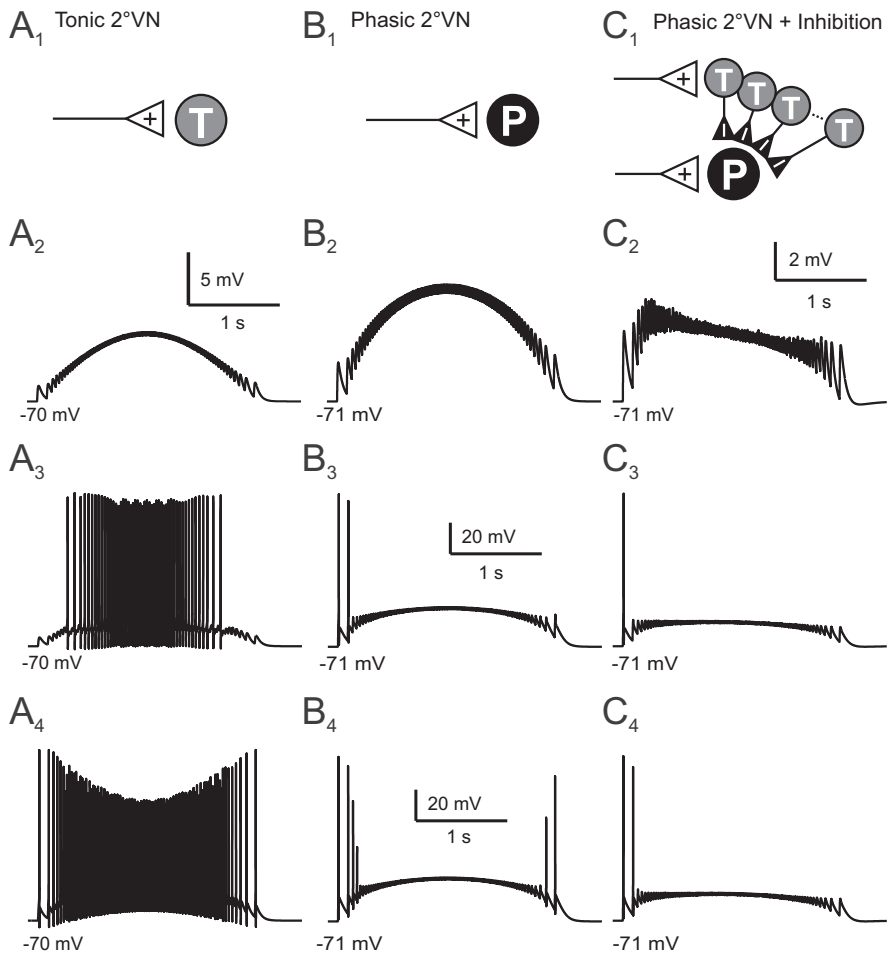
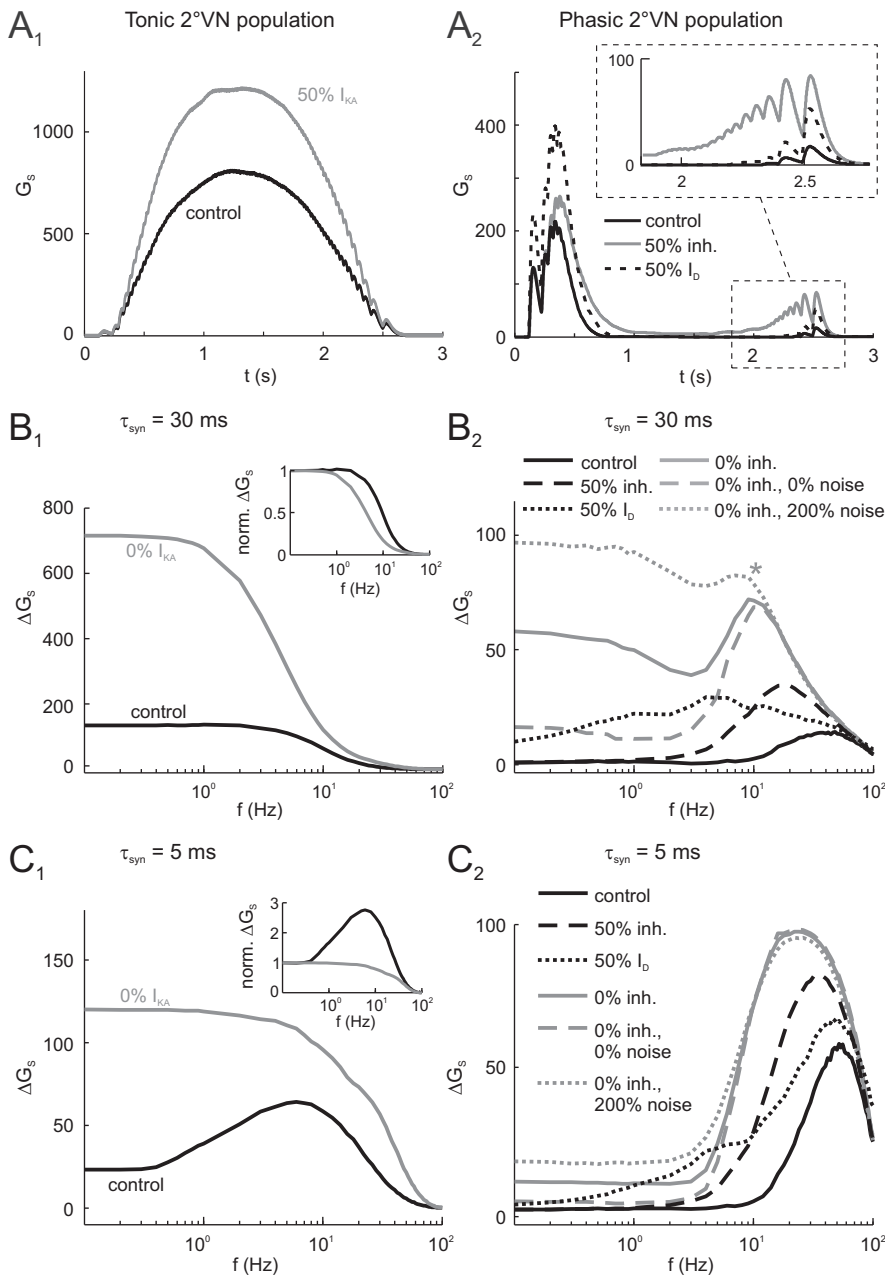


Fig. 7

Rössert et al.

Cellular and network contributions to vestibular signal processing: impact of ion conductances, synaptic inhibition and noise



Supplemental Table 1. Model parameters

	L_E	ρ	C_S (pF)	G_S (nS)	G_D (nS)	g_{Na} (S/cm ²)	g_K (S/cm ²)	τ_n (ms)	g_{KD} (mS/cm ²)	t_{fac}	g_{KA} (mS/cm ²)	τ_a (ms)
Phasic Imp.												
PI1	0.68	3.71	195.81	45.44	10.70	-	-	-	1.51	1.06	-	-
PI2	0.95	6.99	90.93	9.42	65.80	-	-	-	5.13	0.84	-	-
PI3	0.67	1.76	127.77	27.26	6.30	-	-	-	10.00	1.10	-	-
MEAN	0.77	4.15	138.17	27.37	27.60	-	-	-	5.55	1.00	-	-
SD	0.16	2.64	53.21	18.01	33.16	-	-	-	4.26	0.14	-	-
Tonic												
T1	1.05	6.22	84.28	15.53	3.65	0.074	0.016	7.2	-	-	0.073	58.58
T2	0.67	6.86	93.13	36.56	5.99	0.108	0.013	3.1	-	-	0.123	51.08
T3	0.98	7.89	118.12	38.10	12.97	0.098	0.013	4.1	-	-	0.105	44.32
T4	1.22	8.46	75.76	32.50	8.05	0.125	0.009	2.9	-	-	0.106	46.04
T5	1.50	9.32	111.47	30.84	1.60	0.090	0.018	6.4	-	-	0.240	37.71
T6	0.91	6.41	62.80	17.74	4.34	0.106	0.010	6.0	-	-	0.171	65.18
T7	0.75	5.14	100.24	23.53	11.10	0.112	0.015	2.6	-	-	0.156	42.17
MEAN	1.01	7.19	92.26	27.83	6.81	0.102	0.013	4.6	-	-	0.139	49.30
SD	0.28	1.44	19.60	8.98	4.12	0.017	0.003	1.9	-	-	0.055	9.68
Phasic												
P1	1.66	4.47	39.39	35.88	8.75	0.102	0.013	4.6	3.43	1	-	-
P2	0.86	4.68	27.14	52.02	27.84	0.102	0.013	4.6	1.49	1	-	-
P3	0.79	2.54	32.32	18.97	12.58	0.102	0.013	4.6	2.71	1	-	-
P4	1.42	8.84	38.76	6.85	3.35	0.102	0.013	4.6	4.74	1	-	-
P5	1.05	2.22	23.28	38.80	20.09	0.102	0.013	4.6	0.71	1	-	-
P6	0.73	5.21	22.20	34.23	2.24	0.102	0.013	4.6	1.66	1	-	-
P7	1.41	9.04	41.64	35.03	30.84	0.102	0.013	4.6	4.40	1	-	-
P8	0.75	6.20	46.60	24.00	17.98	0.102	0.013	4.6	2.57	1	-	-
P9	0.70	6.13	12.26	27.85	13.26	0.102	0.013	4.6	7.08	1	-	-
P10	0.73	9.45	36.60	42.70	4.45	0.102	0.013	4.6	1.23	1	-	-
P11	1.09	9.73	56.85	4.41	12.86	0.102	0.013	4.6	8.19	1	-	-
P12	1.17	2.26	48.82	20.29	43.94	0.102	0.013	4.6	1.97	1	-	-
P12	1.15	2.48	21.75	18.46	9.89	0.102	0.013	4.6	1.96	1	-	-
P14	0.77	5.18	61.79	13.88	20.67	0.102	0.013	4.6	1.73	1	-	-
P15	0.88	8.65	74.77	29.45	7.76	0.102	0.013	4.6	1.86	1	-	-
P16	0.81	8.75	37.68	37.71	7.91	0.102	0.013	4.6	0.85	1	-	-
P17	1.10	9.21	22.99	43.65	12.20	0.102	0.013	4.6	0.75	1	-	-
MEAN	1.00	6.18	37.93	28.48	15.09	0.102	0.013	4.6	2.78	1	-	-
SD	0.29	2.80	16.30	13.34	10.95	-	-	-	2.17	-	-	-

Parameters for the Hodgkin-Huxley type models of phasic and tonic 2°VN (see details in Methods). For both neuron types, time-domain models have been fitted to frequency-current (f-I) and membrane potential decay responses (cells T1-T7 and P1-P17). Additionally, frequency-domain models have been fitted to impedance magnitude measurements of three phasic neurons (cells PI1-PI3). The mean values (MEAN) and standard deviations (SD) are indicated for each fit method and cell type.

